

NOTE TO USERS

This reproduction is the best copy available.

UMI[®]

Large Eddy Simulations for Compressible Turbulent Jet Flows

Nima Tajallipour

A Thesis

in

the Department

of

Mechanical and Industrial Engineering

Presented in Partial Fulfillment of the Requirements
for the Degree of Doctor of Philosophy (Mechanical Engineering) at
Concordia University
Montreal, Quebec, Canada

May 2009

© Nima Tajallipour



Library and Archives
Canada

Published Heritage
Branch

395 Wellington Street
Ottawa ON K1A 0N4
Canada

Bibliothèque et
Archives Canada

Direction du
Patrimoine de l'édition

395, rue Wellington
Ottawa ON K1A 0N4
Canada

Your file *Votre référence*
ISBN: 978-0-494-63428-8
Our file *Notre référence*
ISBN: 978-0-494-63428-8

NOTICE:

The author has granted a non-exclusive license allowing Library and Archives Canada to reproduce, publish, archive, preserve, conserve, communicate to the public by telecommunication or on the Internet, loan, distribute and sell theses worldwide, for commercial or non-commercial purposes, in microform, paper, electronic and/or any other formats.

The author retains copyright ownership and moral rights in this thesis. Neither the thesis nor substantial extracts from it may be printed or otherwise reproduced without the author's permission.

In compliance with the Canadian Privacy Act some supporting forms may have been removed from this thesis.

While these forms may be included in the document page count, their removal does not represent any loss of content from the thesis.

AVIS:

L'auteur a accordé une licence non exclusive permettant à la Bibliothèque et Archives Canada de reproduire, publier, archiver, sauvegarder, conserver, transmettre au public par télécommunication ou par l'Internet, prêter, distribuer et vendre des thèses partout dans le monde, à des fins commerciales ou autres, sur support microforme, papier, électronique et/ou autres formats.

L'auteur conserve la propriété du droit d'auteur et des droits moraux qui protègent cette thèse. Ni la thèse ni des extraits substantiels de celle-ci ne doivent être imprimés ou autrement reproduits sans son autorisation.

Conformément à la loi canadienne sur la protection de la vie privée, quelques formulaires secondaires ont été enlevés de cette thèse.

Bien que ces formulaires aient inclus dans la pagination, il n'y aura aucun contenu manquant.


Canada

ABSTRACT

LARGE EDDY SIMULATIONS FOR COMPRESSIBLE TURBULENT JET FLOWS

Nima Tajallipour, Ph.D.
Concordia University, 2009

Large Eddy Simulation is generally perceived as a very effective and highly promising method that can considerably improve our modeling of turbulent flows. Application of LES has considerably increased in the past decade among thermofluid scholars as well as within different industries. The main obstacles in further implementation of this method for engineering applications are its relatively high computational cost and also unavailability of well tuned and tested numerical tools and therefore there is a great interest in modification of available low order numerical tools which are computationally reasonable in order to use them for LES.

This dissertation is investigating the possibility of applying an available finite element/volume numerical code; used previously for RANS simulations of compressible flows, in order to carry out LES. In this work, a self-adaptive upwinding method, which is compatible with Roe's scheme and reduces the numerical dissipation of low order flux calculation on unstructured elements, is developed. At first, the proposed method is evaluated using channel flow stability test and decaying isotropic turbulence. The method is then used to numerically investigate a high Reynolds compressible turbulent free jet and compare the results with recently published set of experimental data. At the end, a hydrogen jet releasing from a high pressure reservoir is also numerically studied. During these simulations, the performance of the developed numerical tool for subsonic, sonic and supersonic flows at high Reynolds numbers will be extensively analyzed.

ACKNOWLEDGMENTS

I would like to express my sincere gratitude to my supervisor Dr. Marius Paraschivoiu for all his support, patience and valuable advice during my studies. He continually and convincingly conveyed a spirit of adventure to me in regard to research and never gave up on me through the difficult times. Without his guidance and persistent help this dissertation would not have been possible.

I thank Concordia University and the Réseau québécois de calcul de haute performance (RQCHP) for providing the necessary facilities as well as the computational resources for my research. Many thanks to Hui Zhong Lu and Steve Allen at the Université de Sherbrooke, whom their help was essential in MPI parallel computations and programming needed for this dissertation.

I would like to dedicate this dissertation to my father and my mother and express my greatest and deepest appreciation to them for their relentless support and prayers.

Table of Contents

List of Figures	vii
List of Tables	xi
Nomenclature	xii
1 Introduction	1
1.1 Motivation	1
1.2 Literature Review	2
1.3 Objectives and Thesis Outline	8
1.4 Structure of the Turbulent Free Jets	10
1.4.1 Kelvin-Helmholtz Instability	12
1.5 Hydrogen Release Jet from a High Pressure Reservoir (100 atm)	13
2 Large Eddy Simulation	17
2.1 Definition and application	17
2.2 Governing Equations	24
2.3 Subgrid Scale Models	26
2.3.1 Smagorinsky Subgrid Scale Model	27
2.4 Statistical Analysis of Turbulence	28
3 Applied Numerical Method for LES	29
3.1 Numerical Method for LES	29
3.2 Spatial Discretization	32
3.2.1 Convective Flux Calculation	33
3.2.2 Self-Adaptive Upwinding Scheme	35

3.3	Temporal Discretization	38
3.4	Boundary Conditions	40
3.4.1	Subsonic Inlet Boundary Condition	44
3.4.2	Noslip Adiabatic Boundary Condition	44
3.4.3	Free Slip Boundary Condition	45
3.4.4	Nonreflective Boundary Condition	45
3.4.5	Pressure Outlet Boundary Condition	46
3.4.6	Periodic Boundary Condition	46
4	Numerical Verifications	48
4.1	Channel Flow Stability Simulation	48
4.2	Decaying Isotropic Turbulence	53
4.2.1	Interaction of the Limiter Function and the Upwinding Term	64
5	LES of a Round Compressible Turbulent Free Jet	68
5.1	Experimental Setup and Measurements	68
5.2	Numerical Setup	72
5.3	Numerical Results	76
6	LES of a Hydrogen Jet Releasing from a High Pressure Reservoir (100 atm)	83
6.1	Numerical Setup	83
6.2	Numerical Results	85
6.2.1	Interaction of the Limiter Function and the Upwinding Term	101
7	Conclusions and Future works	105
	References	109
	Appendix A: Theoretical Analysis of Free Jets	121

List of Figures

<u>Figure</u>		<u>Page</u>
1.1	Different flow regions formed after the nozzle's exit	11
1.2	Deformation of the discontinuity surface (time is passing from a to f)	12
1.3	Jet structure at $t = 91\mu\text{sec}$ and $P_{in} / P_{\infty} = 25$ (Ref. 54)	15
1.4	Jet structure at $t = 181\mu\text{sec}$ and $P_{in} / P_{\infty} = 25$ (Ref. 54)	15
2.1	Cascade of energy (Ref. 76)	20
2.2	A depiction of observed energy spectrum for isentropic turbulence	21
3.1	Share of the cell C_i from an adjacent tetrahedron	33
3.2	Control volumes and convective flux calculation	34
3.3	Convective flux calculation	35
3.4	The definition of a wiggle in the present computations (Ref. 91)	36
3.5	Flux calculation for the nonreflective boundary condition	46
3.6	Nodes I and J attached according to the periodic boundary condition	47
4.1	Channel flow's grid and boundary conditions	49
4.2	Channel flow simulation (Cases 1, 2, 3, 4)	51
4.3	Channel flow simulation (Cases 2, 5, 6).	52
4.4	Non-dim. y-velocity (Case 4)	52
4.5	Comte-Bellot and Corrsin's experimental setup	53
4.6	Energy spectrum at $U_0 t_{CBC} / M = 42$	59
4.7	Non-dimensional vorticity at non-dimensional times $t=0.0$ and $t=0.1266$	60
4.8	Total kinetic energy (Cases 1, 2, 3, 4)	62

4.9	E(k) at $U_0 t_{CBC} / M = 98$ (Cases 1, 2, 3, 4)	62
4.10	E(k) at $U_0 t_{CBC} / M = 171$ (Cases 1, 2, 3, 4)	62
4.11	Total kinetic energy (Cases 3, 4, 5, 6)	63
4.12	E(k) at $U_0 t_{CBC} / M = 98$ (Cases 3, 4, 5, 6)	63
4.13	E(k) at $U_0 t_{CBC} / M = 171$ (Cases 3, 4, 5, 6)	63
4.14	Average limiter coefficient (Case 1)	66
4.15	Average upwinding coefficient (Case 3)	66
4.16	Average limiter coefficient (Case 3)	66
5.1	First configuration of jet facility (Refs. 101,102)	69
5.2	Second configuration of jet facility (Refs. 99,100)	69
5.3	Principle of Rayleigh scattering technique (Ref. 101)	70
5.4	Schematic of optical setup in a quiet, adjoining room to analyze the collected light, L_1 to L_5 are lenses; BS_1 is beam-splitter and FPI_1 is the Fabry-Perot interferometer (first configuration, Ref. 101)	71
5.5	Principles of velocity measurement by Rayleigh scattering technique (Ref. 101)	71
5.6	The applied coordinate system and the location of microphones (Ref. 99)	72
5.7	Grid for the free jet simulation: (a) entire computational domain, (b) jet's inlet	73
5.8	Boundary conditions for compressible turbulent free jet	74
5.9	Instantaneous distribution of density ($\rho(t) / \rho_j$).	76
5.10	Instantaneous distribution of Mach number (Ma_j)	76
5.11	Instantaneous distribution of vorticity ($0 \leq Vorticity \times D / U_j \leq 46$)	77
5.12	Instantaneous distribution of pressure ($P(t) / P_a$)	77
5.13	Mean velocity distribution at $X/D=0.1$	79
5.14	Mean velocity distribution at $X/D=1.0$	79
5.15	Mean density distribution along the jet's axis	80
5.16	rms density fluctuation along the jet's axis	80
5.17	Mean density distribution at $X/D=0.1$	80

5.18	Mean density distribution at $X/D=1.0$.	81
5.19	Mean density distribution at different axial locations	82
5.20	rms density fluctuations at different axial locations	82
6.1	Boundary conditions for the hydrogen release jet	84
6.2	3D grid and subdomains for the hydrogen release jet	84
6.3	Density contours for $0.0 \leq \rho \leq 1$ ($t = 5.01\mu s$)	87
6.4	Mach contours ($t = 5.01\mu s$)	87
6.5	Temperature contours ($t = 5.01\mu s$)	87
6.6	Density contours for $0.0 \leq \rho \leq 1$ ($t = 10.03\mu s$)	88
6.7	Mach contours ($t = 10.03\mu s$)	88
6.8	Temperature contours ($t = 10.03\mu s$)	88
6.9	Density contours for $0.0 \leq \rho \leq 1$ ($t = 15.09\mu s$)	89
6.10	Mach contours ($t = 15.09\mu s$)	89
6.11	Temperature contours ($t = 15.09\mu s$)	89
6.12	Density contours for $0.0 \leq \rho \leq 1$ ($t = 20.09\mu s$)	90
6.13	Mach contours ($t = 20.09\mu s$)	90
6.14	Temperature contours ($t = 20.09\mu s$)	90
6.15	Density contours for $0.0 \leq \rho \leq 1$ ($t = 25.15\mu s$)	91
6.16	Mach contours ($t = 25.15\mu s$)	91
6.17	Temperature contours ($t = 25.15\mu s$)	91
6.18	Density contours for $0.0 \leq \rho \leq 1$ ($t = 30.21\mu s$)	92
6.19	Mach contours ($t = 30.21\mu s$)	92
6.20	Temperature contours ($t = 30.21\mu s$)	92
6.21	Density contours for $0.0 \leq \rho \leq 1$ ($t = 55.34\mu s$)	93
6.22	Mach contours ($t = 55.34\mu s$)	93
6.23	Temperature contours ($t = 55.34\mu s$)	93

6.24	Density contours for $0.0 \leq \rho \leq 1$ ($t = 75.98\mu s$)	94
6.25	Mach contours ($t = 75.98\mu s$)	94
6.26	Temperature contours ($t = 75.98\mu s$)	94
6.27	Density contours for $0.0 \leq \rho \leq 1$ ($t = 94.98\mu s$)	95
6.28	Mach contours ($t = 94.98\mu s$)	95
6.29	Temperature contours ($t = 94.98\mu s$)	95
6.30	Density contours for $0.0 \leq \rho \leq 1$ ($t = 113.96\mu s$)	96
6.31	Mach contours ($t = 113.96\mu s$)	96
6.32	Temperature contours ($t = 113.96\mu s$)	96
6.33	Density contours for $0.0 \leq \rho \leq 1$ ($t = 151.96\mu s$)	97
6.34	Mach contours ($t = 151.96\mu s$)	97
6.35	Temperature contours ($t = 151.96\mu s$)	97
6.36	Density contours for $0.0 \leq \rho \leq 1$ and $Z/D = 10$ ($t = 151.96\mu s$)	98
6.37	Mach contours at $Z/D = 10$ ($t = 151.96\mu s$)	98
6.38	Temperature contours at $Z/D = 10$ ($t = 151.96\mu s$)	98
6.39	Mach distribution along the centerline (Case 1)	99
6.40	Density distribution along the center line(Case 1)	99
6.41	Mach distribution along the centerline (Case 2)	100
6.42	Density distribution along the center line(Case 2)	100
6.43	Limiter coefficient for density($t = 55.34\mu s$)	102
6.44	Limiter coefficient for velocity in the x-direction ($t = 55.34\mu s$)	102
6.45	Limiter coefficient for velocity in the y-direction ($t = 55.34\mu s$)	102
6.46	Limiter coefficient for velocity in the z-direction ($t = 55.34\mu s$)	103
6.47	Limiter coefficient for pressure ($t = 55.34\mu s$)	103
6.48	Upwinding parameter ($t = 55.34\mu s$)	103
A.1	Definition of a typical system, control volume and its control surface within a free jet	121

List of Tables

<u>Table</u>		<u>Page</u>
4.1	Explanation of different cases for channel flow simulation	51
4.2	Coefficients used to define energy spectrum at $U_0 t_{CBC} / M = 42$	54
4.3	Explanation of different cases for decaying turbulence simulation	61
5.1	Comparison of used parameters in different numerical simulation	75
5.2	Operating conditions for the experimental measurements	75
6.1	Operating conditions for the hydrogen release simulation	85
6.2	Explanation of different cases for hydrogen release jet	86

Nomenclature

Symbols

$\bar{f}(x,t)$	filtered function
$\tilde{f}(x,t)$	Favre-filtered function
$f''(x,t)$	fluctuating component of the filtered function
$G(x,\Delta)$	filter function
Δ	filtering size
x_i	cartesian coordinates (i=1,2,3)
$\bar{\rho}$	mean density
\bar{u}_i	cartesian components of the filtered velocity
\bar{p}	mean pressure
\bar{e}	filtered total energy per unit mass
\bar{T}	Favre-filtered static temperature
ρ_∞	reference density
U_∞	reference velocity
L	reference length scale
a_∞	average ambient speed of sound
T_∞	reference static temperature
$\rho_\infty U_\infty^2$	reference dynamic pressure
β	parameters to adjust the gradients in MUSCL scheme
γ	parameters to adjust the upwinding in MUSCL scheme

θ	intensity of the local wiggle
σ_{ij}	molecular viscous stress tensor
$\mu(\tilde{T})$	molecular viscosity
τ_{ij}	subgrid scale stress tensor
\tilde{S}_{ij}	rate-of-strain tensor
C_S	Smagorinsky constant
Q_j	subgrid scale heat flux
\hat{q}	average value of q evaluated at the boundary of a cell
q_-, q_+	inter nodal values between the nodes of an edge
\bar{X}_i	position vector of nodes i
$E(t)$	total kinetic energy
$E_{11}(k)$	one-dimensional energy spectrum
$E(k)$	energy spectrum
M_t	turbulence Mach number
Re_D	Reynolds number based on the jet's diameter
Pr	Prandtl number
Pr_t	turbulent Prandtl number
C_{noise}	coefficient of noise
h_x	element's size in the direction of jet's main axis
h_r	element's size in radial direction in respect to the jet's main axis
h_θ	element's size in tangential direction in respect to the jet's main axis
\bar{F}^{conv}	convective flux
\bar{F}^{diff}	diffusive flux
ϕ	Characteristic test function

ϕ	piecewise linear finite element basis function
\bar{X}	position vector
λ	Kolmogorov scale
$\bar{\epsilon}$	average energy dissipation rate
L	Taylor length (integral length scale)

Superscripts

∞	freestream
a	ambient conditions
j	exit condition at jet's nozzle
rms	root-mean-square

Subscripts

-	spatially filtered quantity
~	spatially Favre-filtered quantity
^	Fourier transfer
→	vector quantity
*	complex conjugate

Abbreviations

CFD	Computational Fluid Dynamics
CFL	Courant-Friedrichs-Lewy
DNS	Direct Numerical Simulation
DSM	Dynamic Smagorinsky Model
DRP	Dispersion Relation Preserving

FF Fast Fourier transfer
LES Large Eddy Simulation
MPI Message Passing Interface
MUSCL Monoton Upstream Centered Schemes for Conservation Laws
RANS Reynolds-Averaged Navier-Stokes
SGS Subgrid Scale
SM Smagorinsky Model

Chapter 1

Introduction

1.1 Motivation

COMPRESSIBLE jets have many engineering as well as scientific applications. Investigation of these jets can improve the design of reacting turbulent jets (Ref. 1,2) or cross flow jets applicable in combustors (Ref. 3), increase the efficiency of coaxial jet mixers (Refs. 4,5), provide a better understanding of jet noise generation mechanisms which will eventually lead towards designing aircrafts with lower noise emission (Refs. 6,7), decrease the screech noise generated by over or under-expanded jets (Ref. 8) or improve the design of high pressure gas vessels. The obtained knowledge about the physics of compressible jets can be even applied in the medical science to predict human's speech (phonation), because the primary source of human's voice is the pulsation of glottal jet (with the Reynolds number in the order of 10,000) generated by the vibration of vocal folds (mentioned in Ref. 9). Since Lighthill (1952),^{10,11} many attempts have been made based on his work to numerically predict the generated noise of compressible turbulent flows.

Theoretically studying the jet flows specially when the Reynolds number is high and the flow is turbulent is very difficult. On the other hand, experimental techniques are rather expensive, quite complicated and always contain a degree of uncertainty. As a result, numerical methods have been implemented in the past to achieve a better understanding of these flows. Large eddy simulation, in particular is considered as an optimum method because of its potential ability to simulate the larger scales of motion present in the flow and its lower computational cost in comparison to Direct Numerical Simulation (DNS).

In order to carry out reliable large eddy simulations, development of accurate numerical tools is fundamental. As it will be explained in the literature review section, there has not been enough research done on the performance of low order, upwinding schemes when they are used for LES. The effect of using unstructured grids is also not fully understood. In a typical LES intended for the industrial applications, given that considered flows are usually geometrically complex, it is not appropriate to use extremely refined models or highly accurate methods. Therefore there is a very high interest in modifying the available low order numerical tools in order to make them suitable for LES. That is the main objective of this study.

In this research, the performance of an available finite element/volume numerical code, previously used for RANS simulations of compressible flows, is extensively studied using channel flow stability test, single standing vortex simulation and isotropic decaying turbulence test. These numerical tests are used in order to review and investigate some of the main aspects of the turbulent flows' numerical simulation such as cascade of energy from high to low scale eddies, effects of subgrid modeling, numerical dissipation, accuracy, robustness and stability. A self-adaptive upwinding method, inspired by Refs. (12,13) and compatible with the available numerical scheme, is then implemented in order to improve the results. A compressible turbulent jet is simulated and the ability of the numerical method in predicting the average and fluctuating flow variables are determined using a recently published series of experimental data. Finally a hydrogen jet, releasing from a high pressure reservoir into the atmosphere is numerically studied and results are discussed and presented.

1.2 Literature Review

Until the 1990s, study and investigation of compressible jets have been mainly based on experimental measurements and theoretical approaches such as momentum integral method.^{14,15,16} It was only in the late 1990s that numerical methods were used to simulate and study compressible jets. Since then, obtaining an accurate prediction of jets' spreading rate and the length of their potential core has been a challenge. The length of the potential core is defined as the axial location downstream of the flow where the centerline mean velocity (U_C) equals 0.95 of the jet's axial velocity at the nozzle's exit (U_j).

Gamet and Estivalezes (1998),¹⁷ used a finite volume, high-order 2-4 MacCormack numerical scheme (2nd order accurate in time 4th accurate in space) to carry out the DNS and LES of a hot jet at Reynolds numbers equal to 1000 (2D simulation) and 3×10^4 (3D simulation) respectively. The potential core's length in their simulation was over-predicted.

Zhao et al. (2001),¹⁸ simulated two compressible turbulent jets at $Ma = 0.9$, $Re = 3.6 \times 10^3$ and $Ma = 0.4$, $Re = 5 \times 10^3$ using a combination of Fourier pseudospectral method and a 6th order compact finite difference method for the spatial discretization while turbulence fluctuations were forced at the inlet boundary condition. In their study, decaying rate of the axial velocity and the length of the potential core were accurately predicted using both dynamic Smagorinsky and mixed subgrid models. Similarly, Freund (2001),¹⁹ investigated the sound generation mechanism of a turbulent jet in a Mach of 0.9 and Reynolds number of 3600, using DNS. In his work, a 6th order compact finite difference method was used for the flux calculation in which the derivatives were computed with the Fourier spectral method. The potential core was accurately predicted but in their simulations, the intensity of the fluctuation at the inflow was set in an ad hoc fashion.

DeBonis and Scott (2002),²⁰ used a 4th order central difference spatial operator and a 6th order filtering technique to add the necessary artificial dissipation in order to simulate a compressible supersonic turbulent jet at $Ma = 1.4$ and $Re = 1.2 \times 10^6$. Their simulation over-predicted the decay rate of the flow and therefore the potential core was shorter than the experimental value. They suspected that adjustment of subgrid model's constant can positively affect the length of the potential core. They have also mentioned few references in their paper in which the length of potential core has been over-predicted. Andersson et al. (2003),²¹ simulated a compressible unheated turbulent jet at $Ma = 0.75$ using a 3rd order low-dissipation upwind scheme for convective fluxes, centered difference approach for the diffusive fluxes and a 2nd order Runge-Kutta for temporal discretization. Their model had 3×10^6 cells and the Smagorinsky model was used to compensate the effects of subgrid scales. In their simulation they failed to predict the length of the jet potential core. The applied numerical method over-predicted the spreading and therefore the length of the potential core was under-predicted. Based on the given discussion, we conclude that depending on the case, the length of the potential core might be accurately predicted, over-predicted or under-predicted.

The mixing rate and therefore the potential core's length are mainly affected by subgrid scale viscosity, numerical scheme, entrainment and inflow boundary condition (Ref. 22). The importance of applying a realistic- turbulent-inlet boundary condition in LES has been mentioned in the literature, especially for wall bounded flows (Ref. 23) but surprisingly in some simulations no significant effect has been observed. Andersson et al. (2005),^{24,25} recently studied the effects of these parameters on the LES of turbulent jets. Forcing external fluctuation at inlet didn't show any detectable effect on the statistics of the flow near the nozzle. The test case with lower subgrid contribution started to mix immediately as the jet exited the nozzle and this mixing was less rapid and violent in comparison to the test case with higher subgrid model. Increasing the subgrid scale filter width resulted in augmented high frequency content of the forward radiated sound as well as significant changes to the sound radiated to the rear arc. It was shown that the length of the potential core directly affected the overall intensity as well as the frequency content of the predicted noise. Despite including the geometry of the nozzle in their simulation, the potential core's length was under-predicted. They mentioned that increasing the subgrid-scale dissipation resulted in decreasing the length of the potential core despite an increase in the mixing rate. This conclusion however is not consistent with other similar studies.

The effect of the subgrid model on the flow regime of compressible turbulent jets seems to be significant but at the same time it is rather difficult to assess. Morris et al. (2002),²⁶ simulated a circular heated ($Ma = 1.48$) and an unheated ($Ma = 2.1$) jet at $Re = 10^5$ by solving nonlinear disturbance equations using a finite difference method, including a 4th order optimized DRP scheme accompanied with the 6th order artificial dissipation. They recognized the significant effect that subgrid model could have on the flow variables as well as on the generated noise. Suto et al. (2004),²⁷ simulated incompressible round jets at different Reynolds numbers ($Re = 1,200 \sim 100,000$) using a 4th order central difference numerical method. In their simulation, they used constant and dynamic Smagorinsky subgrid models. They observed that in the regions close to the inlet ($x/D \leq 2$), the dynamic model predicted high values of subgrid constant but that value decreased along the radial direction. At the fully-developed region ($x/D \geq 8$) the average value for the subgrid coefficient that was predicted by the dynamic model was higher than the value recommended for isotropic turbulent decaying and was also higher than the predicted values close to the

inlet. The maximum value at every axial location was still predicted at the center of the jet. The overall subgrid constant predicted by the dynamic model at $x/D \geq 2$ was $C_S \approx 0.04$ based on the definition given in chapter 2.3.1. They also reported that decay of mean velocity was somewhat stronger for their coarser mesh.

DeBonis (2004),²⁸ used a central difference spatial discretization and an explicit low-dispersion Runge-Kutta temporal discretization in order to simulate a compressible turbulent jet at $Ma = 0.9$ and $Re = 1.1 \times 10^6$, using 2.4×10^6 nodes. Their results indicated a strong dependence of the solution's accuracy on the value of Smagorinsky subgrid model's coefficient. When its value was set to 0.012 (typical for decaying isotropic turbulence), significantly large scales appeared in the mixing layer and it resulted in rapid spreading of jet and generation of a much shorter potential core. However, when subgrid coefficient was set to 0.1, the spreading was weaker and the length of the potential core was much closer to the experimentally predicted value.

Boersma (2005),²⁹ simulated an incompressible jet with $Re = 11000$ using a 2nd order finite volume method and 2nd order Adams-Bashforth temporal discretization. He chose a significantly higher value for the Smagorinsky coefficient $C_S = 0.15$ and the decaying rate of the central velocity matched very well with the experimental data. It is interesting to mention that strong overshoots in the instantaneous axial velocity distribution along the centerline were observed.

Culter et al. (2006),³⁰ recently simulated a coaxial (He, air) turbulent jet at $Ma = 1.8$ using a structured, finite volume code, $\tilde{k} - \tilde{\omega}$ turbulence model, one-third MUSCL scheme accompanied with the approximate Riemann solver of Roe problem and a 2nd order central method for the viscous fluxes. They have observed that the various simulated quantities deviated from the experimental values, especially near the boundary of coflow stream and the shear layer of jet and this deviation could be corrected by increasing the radial diffusion of turbulent kinetic energy. In their simulation the nozzle geometry has been included.

Bogey and Bailly (2006),³¹ simulated a compressible jet at $Ma = 0.9$ and for $2.5 \times 10^3 \leq Re \leq 4 \times 10^5$ using a numerical method already optimized in the Fourier space to minimize the dispersion and dissipation errors and calculates the spatial derivatives using a 4th order centered finite differencing and 2nd order Runge-Kutta algorithm. Grid-to-grid oscillations were removed by an explicit 4th order (13 point and 21

point) filter. They have concluded that having stronger subgrid model would result in a slightly longer potential core, even though it significantly increased the axial velocity decaying rate further downstream, and the dynamic subgrid model dissipates a significant part of the energy through a wide range of the spectrum. The dynamic subgrid model predicted an average value of 0.02 for the Smagorinsky constant (similar to isotropic decaying turbulence) while instantaneous overshoots reached to 0.04. The computational domain contained 12.5 million points and the peak value of the velocity fluctuation increased when the SGS model was activated.

Based on the above discussion, we can conclude that dissipation resulting from the subgrid model is expected to decrease the mixing and increases the length of the potential core. The correct value of subgrid coefficient however is very dependent on the applied numerical method. Therefore, as one of the objectives of this study, the valid range for C_S is investigated for jets.

Regarding the effects of entrainment, Babu and Mahesh (2004,2005),^{32,33} have simulated laminar and turbulent incompressible jets (DNS) and have investigated the effects of the entrainment on the flow by adjusting the length of the buffer region behind the flow inlet. They used a predictor-corrector algorithm which has been shown earlier to be nondissipative and yet robust at high Reynolds numbers and for complex geometries. They have shown that the inflow entrainment reduced the length of the potential core and increases the peak levels of the pressure fluctuations while the peaks of axial turbulent velocity remained the same. The length of the potential core in this simulation was under-predicted.

Randomly forced fluctuation at the inflow and the thickness of inflow's shear layer are expected to have significant effects on the flow and the acoustic field. Application of artificial forcing however can be justified only when the geometry of the nozzle is not included in the numerical model. Bogey et al. (2003),^{34,35} simulated a compressible turbulent jet at $Re_D = 65,000$ and $Ma = 0.9$, using the seven-point stencil, Dispersion-Relation-Preserving (DRP) finite-difference scheme accompanied with random velocity fluctuations at the inflow. Both the flow development and emitted sound were shown to depend appreciably on the initial parameters. A thinner initial jet shear layer thickness increased the noise levels in the sideline direction but it reduced them in the downstream direction. The most important changes were obtained when the four azimuthal modes of forcing were removed. It noticeably reduced the noise levels.

Heating and Mach number also can affect the generated noise. Following the standard Reynolds decomposition (as it was explained in Ref. 36), the noise generated by a turbulent flow can be divided into three different sources: shear noise (interaction of turbulent fluctuations and the mean flow), self noise (interaction of turbulent fluctuations with themselves) and entropy component (result of deviation of the pressure and density from the isentropic relation in the turbulent flow). Therefore accurate calculation of turbulent flow has direct impact on the accuracy of the simulated noise. Lew et al. (2007),³⁶ have shown that when a high speed subsonic compressible jet is heated while the ambient jet Mach number remains constant, significant cancellations occur in the far-field between the shear and entropy noise and therefore the overall level of noise decreases. Heating also reduces the intensity of the nonlinear self noise terms. For low speed heated jets, the main contributing source is the entropy noise while the shear and self noise hardly contribute to noise level at the far field.

The randomly forced fluctuations at inlet could potentially introduce some negative effects into the numerical results. For example Uzan et al. (2004),⁷ simulated a compressible turbulent jet using a 6th order accurate non-dissipative compact schemes. Since the actual nozzle geometry has not been included in their simulation, they have added randomized velocity perturbations in the form of a vortex ring into the jet shear layer at the $D/2$ distance from the inflow boundary. They have explained that the random inflow could be the reason for over-prediction of the generated noise. The overall predicted noise of their isothermal jet is more than the similar experimental results for cold jets which is not acceptable despite implementing a rather fine grid (20×10^6 nodes).

It is suspected that simulating the nozzle geometry in the simulation would positively affect the instability characteristics of the flow close to the jets exhaust and therefore it might improve the accuracy of the results. To the best of our knowledge, no study has been done yet to measure the importance of this parameter, even though in some cases, despite the inclusion of the nozzle's geometry, the expected effects have not been detected. For example in the jet simulation of Andersoon and el. (2005),⁶ length of the potential core was less than the experimental value and no fluctuation was detected at the inlet despite the fact that inlet's geometry was included in the simulation.

All the parameters mentioned above, significantly affect the LES results of compressible turbulent jets and therefore a special attention is needed in order to determine the best combination, based on the available numerical tool and computational resources.

1.3 Objectives and Thesis Outline

The applied numerical model plays a significant role in the accuracy especially for high Mach number jets. The issue in the supersonic flows is to concentrate the numerical dissipation only at the regions where shocks are present (Ref. 38) and confine their effects only to the highest scales. It has been shown however that numerical errors and subgrid models affect the entire turbulent energy spectrum of the flow and not only the high frequency fluctuations (Ref. 39). There are many different sources of error which may negatively affect the results. For example, in the case of unstructured grids which automatically require non-uniform filtering, the filtering and the differentiation operation do not commute. Ghosal and Moin (1995),⁴⁰ have shown that the application of standard large eddy equations introduces an error term which has the same order of magnitude as the 2nd order finite difference method which was used in order to discretize the LES equations. Other sources of error such as discretization or aliasing errors must also be taken into consideration. It is rather difficult to increase the accuracy of numerical method especially for unstructured discretization. There has been however many attempts to improve the accuracy of numerical methods for LES of jets. For example Constantinescu and Lele (2002)⁴¹ have proposed a highly accurate method in the cylindrical coordinate system. It should be also mentioned that, large eddy simulations of jets are usually very slow and require a long computational time. Fureby et al. (2002),⁴² have explained that because the NS equations are formally not filtered in time for LES, they should be fully resolved with $\Delta t < \tau_K$ (Δt is the time step and τ_K the Kolmogorov time). In practice, however, only the large scales are aimed to be retained and therefore higher values of Δt might be chosen. It should however be considered as another source of error.

There are not many studies about the effects of upwinding in the LES of compressible jets. Shur et al. (2005),^{43,44} have investigated the possibility of predicting the noise emitted from a typical jet engine by applying an upwinding method. They used a finite-volume method, based on flux-difference splitting

algorithm of Roe and Monoton Upstream-centered Schemes for Conservation Laws (MUSCL) to simulate the flow over a structured grid. In order to control the excessive dissipation generated by the upwinding, they have decreased the contribution of the upwinding term by multiplying it into an upwinding parameter (σ_{upw}). This parameter has provided a gradual switch from nearly centered scheme ($\sigma_{upw} = 0.25$) in the internal region of the domain towards the full upwinding scheme ($\sigma_{upw} = 1.0$) at the boundaries. They have concluded that the amount of upwinding and the strength of subgrid model directly affect the features of flow such as shear-layer roll-up, three-dimensionalization of the flow and transition to turbulence. They have shown that full upwinding scheme can considerably delay the transition of the flow and therefore increase the length of the potential core. In their simulation, higher grid resolution has resulted in an earlier transition and a shorter potential core. They have also shown that increasing the coflow results in more stabilization of the flow field and therefore further delay of the transition accompanied with a longer potential core. Assigning the value of σ_{upw} based on an overall judgment about the flow domain (Ref. 45) prohibits their method to be generally applicable.

Application of LES for simulation of turbulent jets is expected to highly expand in the future. At the present time, there is a great interest among the researches and also in the industry, to use low order numerical method such as upwinding methods for LES. In this research, the effect of upwinding on the large eddy simulation of turbulent flow is investigated and after applying necessary modification, the developed numerical method will be used to simulate a compressible turbulent free jet. The performance of the numerical method is evaluated by comparing the results with the available experimental data. As the final step of this research, hydrogen release from a high pressure reservoir (100 atm) will be simulated and the advantage of the proposed scheme will be further demonstrated.

In the remaining portions of this chapter the structure of compressible turbulent free jets is explained and the Kelvin-Helmholtz instabilities which transform the relatively laminar flow exiting from the nozzle into a fully developed turbulent jet are discussed. At the end flow, characteristics of an underexpanded jet, releasing from a high pressure reservoir is studied. A more detailed literature review about the turbulent jets has been previously provided in References 46 and 47.

1.4 Structure of Turbulent Free Jets

Free shear flows are a category of flows in which there is no solid surface present in the flow regime. In this class of flows usually jets, wakes and simple shear layers are studied. Round jets are categorized among the free shear flows,^{48,49} in which the flow is exiting from a circular nozzle of diameter D and is released into an open space. The flow regime is characterized by a significantly higher velocity in the axial direction while the great gradients are present in the transverse directions. These gradients gradually remove the irregularities present between the jet flow and the stagnant medium. This phenomenon makes the flow become more turbulent as it travels further downstream. A potential core is formed right after the nozzle's exit and it contains an irrotational-laminar flow. The interface between the turbulent jet and the surrounding flow is referred to as the mixing layer which has a random shape and is unsteady. This mixing layer thickens while moving away from the nozzle's exit and it reduces the diameter of the potential core while increasing the jet's diameter.

After the disappearance of the potential core, a fully-developed region is formed where the flow gradually reaches a similarity regime and the mean flow quantities such as density, velocity and temperature, at different locations along the axial direction can be collapsed using the proper scaling (Fig. 1.1). The amount of turbulence also increases as the jet travels downstream and its peak value happens close to the transition region which exists between the potential core and the fully developed region.

Experimental and numerical analyses have shown that this flow is very difficult to predict because of its strong dependence on many different parameters. Lau, Morris and Fischer (1979),⁵⁰ have proposed the following empirical equation in order to estimate this length of potential region for the air to air experiment and for the same density:

$$\frac{L_P}{D} = 4.2 + 1.1(Ma_j^2 + 1 - \frac{T_j}{T_a}) \quad (1.1)$$

Harsha (1971) also has proposed another formula for air to air axisymmetric jets:

$$\frac{L_P}{D} = 2.13(Re_D)^{0.097} \quad (1.2)$$

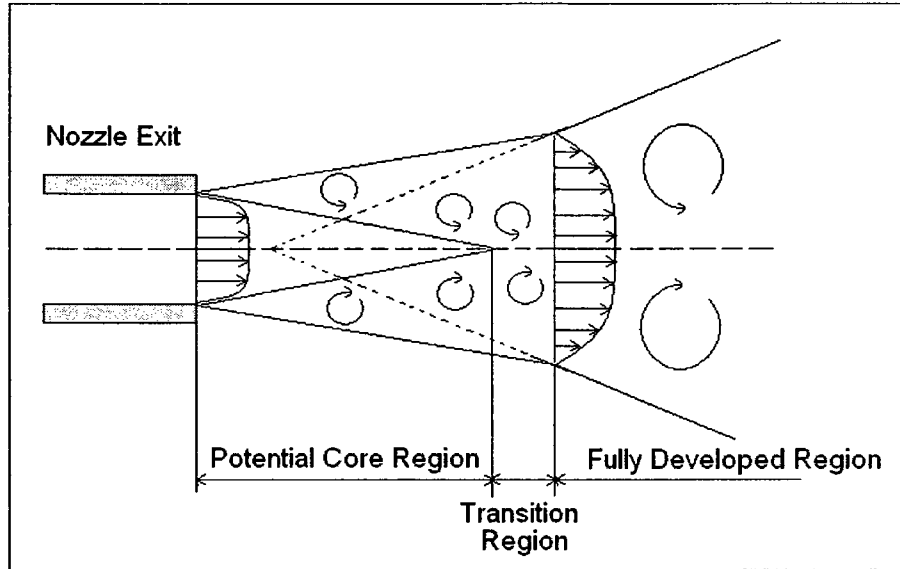


Fig. 1.1 Different flow regions formed after the nozzle's exit.

Lighthill (1963),⁵¹ has shown that the frequency of jet noise which arises from the turbulent mixing of the flow exiting from the nozzle with surrounding air is inversely proportional to the size of the eddies, thus the high frequency sound derives from the mixing region close to the nozzle and the low frequency sound emanates from the fully-developed jet which is well downstream of the nozzle.

From the theoretical point of view, the laminar, incompressible round jets which are flowing into an open medium at rest is the simplest case to be analyzed. These flows are usually studied using the similarity solutions. A detailed analysis is given in Appendix A.

The presented analysis is only for laminar and incompressible flows. Analytical analysis for turbulent flows is only possible for the fully developed region. That analysis however is highly dependent on the similarity assumption and experimental data is required in order to determine unknown coefficients. Therefore the extension of analytical approach for the turbulent jets is not included in the Appendix. As it is shown in Appendix A, the following closed form solution is obtained from the analytical method:

$$U = \frac{3J}{8\pi\rho vx} \left(1 + \frac{3J\eta^2}{64\pi\rho v^2} \right)^{-2} \quad (1.3)$$

$$U_{\max} = \frac{3J}{8\pi\rho vx} \quad (1.4)$$

$$\frac{U}{U_{\max}} = \left(1 + \frac{3J\eta^2}{64\pi\rho v^2}\right)^{-2} \quad (1.5)$$

In which $\eta = \frac{r}{x}$.

1.4.1 Kelvin-Helmholtz Instability

Let's consider a 2D horizontal discontinuity surface (Vortex sheet) where the velocity is equal to u_1 above the surface while its value is equal to u_2 at bottom and $u_1 > u_2$ (Fig. 1.2). The vertical velocities are initially negligible.

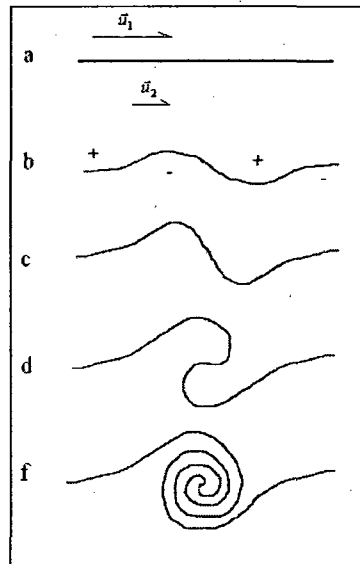


Fig. 1.2 Deformation of the discontinuity surface (time is passing from a to f).

Horizontal discontinuity sheet gradually turns into a shear layer. In this layer vorticity is approximately uniform while it is equal to zero at each side of the layer as velocities are uniform. It is known that the shear layer is potentially unstable and an external perturbation may cause self-attenuating oscillations. Pressure in concavities will become higher than pressure in convexities and the amplitude of the oscillation continues to grow up and eventually the upper part of the sheet is carried by upper fluid instead while the lower part of the sheet is carried by the lower fluid. This phenomenon is known as rolling up (Ref. 52) which also

appears in high Reynolds number turbulent free jets and results in generation of a wide range of eddies and also aerodynamic noise.

1.5 Hydrogen Release Jet from a High Pressure Reservoir (100 atm)

Fossil fuels generate the major part of the energy which we consume every day. They are all carbon-based and therefore their consumption generates a considerable amount of pollution which is of a great environmental concern and is suspected to be the main cause of global warming. Another main concern about these resources is that they are limited and therefore finding a safe, reliable, environmentally clean and also economically reasonable alternative seems to have a great priority. Available fossil resources cannot even satisfy the ever growing energy demand of today's planet and in order to guaranty the energy security of the future generations, a gradual shift towards the alternative energy resources is unavoidable.

Hydrogen is one of the cleanest resources of energy and in theory it can decrease the pollution generated by the vehicles to zero. Its combustion only generates water and therefore many attempts have been made so far in order to manufacture economical vehicles which run on hydrogen. One of the main issues in regard to these vehicles is the storage of hydrogen inside these vehicles. Obviously safe and reliable high pressure reservoirs will be required and therefore the mechanical design and the safety features of these reservoirs are very important. In order to determine the safety requirements in transportation, distribution and also consumption of hydrogen, understanding of the hydrogen flow characteristics in the case of an accidental leakage from high pressure reservoirs is very crucial. Because the pressure of such reservoirs is relatively high, an accidental gas leakage forms a highly underexpanded jet, therefore careful study of underexpanded jets seems to be necessary.

There have been some attempts in the past to analytically analysis the flow characteristics of underexpanded jets. Adamson et al. (1958),⁵³ have presented an analytical method to predict the location of the first normal shock or Mach disk, behind a highly underexpanded nozzle. The method gave good results in comparison to the experimental data for a wide range of pressure ratio (from 5 to 140). Their results however are for steady state conditions and therefore they do not completely represent the unsteady

release of gas from a reservoir. Given the complex nature of the considered flow, applications of experimental as well as numerical methods appear to be desirable.

Ishii et al. (1999),⁵⁴ have experimentally and numerically investigated the time evolution of circular jets released from a shock tube into a large test section. When the shock enters the test chamber, it is diffracted and then gradually moves toward the downstream. Time zero was assumed to be when the shock arrives at the open end of the shock tube. In their work the Reynolds number based on the nozzle diameter was about 100,000. Based on their observation, unsteady development of an underexpanded jet can be divided into four major stages:

- “The first stage of jet evolution is known as the diffraction phenomenon of the shock wave around a corner. The first shock, which passes through the open end of the tube or orifice, begins to diffract around the corner (Fig. 1.3).
- In the second stage, a second shock which is generated in the vortex near the nozzle lip tends to spread towards the jet axis and finally to form a curved shock with an unsteady Mach disk (Fig. 1.3).
- In the third stage, the first shock-cell structure is constructed and for a strong jet, a slip surface is generated downstream of the Mach disk. This surface produces Kelvin-Helmholtz instability waves and is responsible for generating the second vortices (Fig. 1.4).
- In the final stage, a quasi-steady shock cell is formed near the open end and it begins self-sustained oscillation, radiating very strong pressure waves called ‘screech’.”

Pedro et al. (2006),⁵⁵ have also numerically studied the development of the bow shock-wave and the jet structure behind it using FLUENT. Their results also confirm the mentioned jet development stages.

Kameshki (2007),⁵⁶ recently simulated the inviscid hydrogen and air release from a high pressure vessel, initially at pressures equal to 100 and 180 bars, using a Roe-MUSCL numerical method. He has demonstrated how the density of the releasing gas affects the unsteady development of the underexpanded jet.

As it was mentioned before, the final part of this dissertation will be about a simulated hydrogen jet releasing from a high pressure reservoir at 100 atm into a stagnant medium of hydrogen at 1atm pressure.

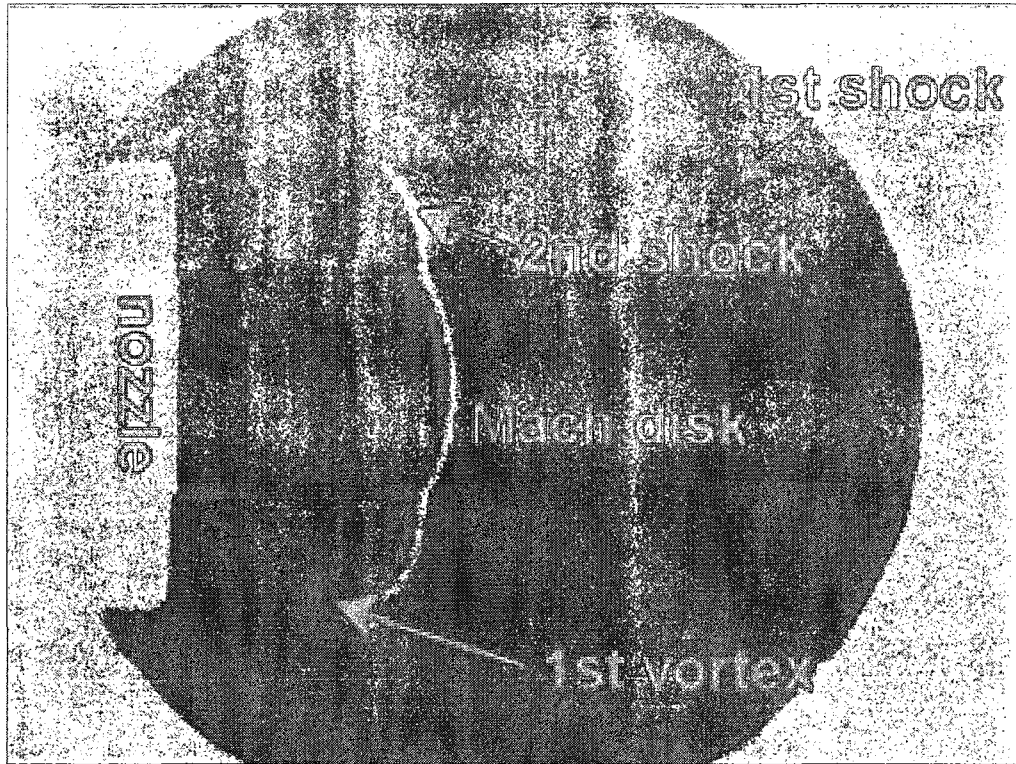


Fig. 1.3 Jet structure at $t = 91\mu\text{sec}$ and $P_{in} / P_{\infty} = 25$ (Ref. 54).

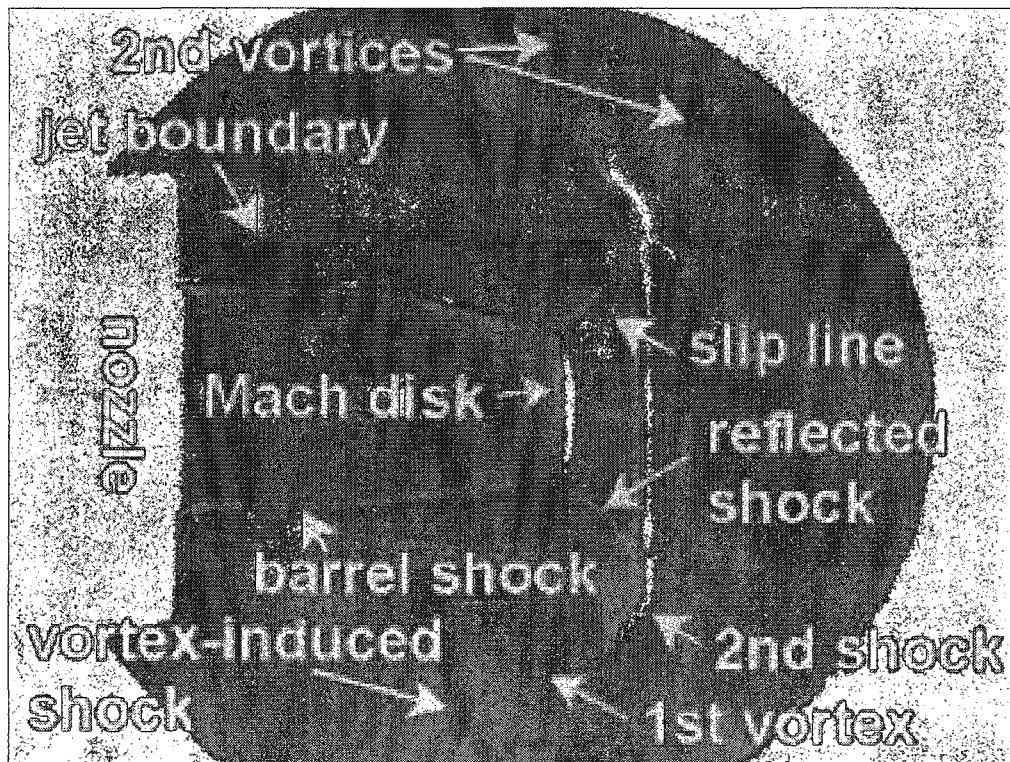


Fig. 1.4 Jet structure at $t = 181\mu\text{sec}$ and $P_{in} / P_{\infty} = 25$ (Ref. 54).

This simulation will provide the opportunity to test the performance of the self-adaptive method for transient supersonic flows and also evaluate its ability to provide accurate realizations for such flows.

Chapter 2

Large Eddy Simulation

THE complex nature of turbulent flows, as demonstrated by Leonardo da Vinci in his sketches has always been intriguing for scientists during the past centuries. It is difficult even for expert researchers to completely agree on a definition for turbulence. It is generally agreed that turbulent flows have three dimensionality, unsteadiness, strong vorticity, unpredictability in details and also a broad spectrum. These complex characteristics are because of many small eddies with different amplitudes, which are present in a typical turbulent flow. These scales interact with each other and exchange energy.

The numerical methods have already been used for many years to study turbulent flows. As it has been mentioned in Ref. 57, not all turbulent flows can be treated by numerical methods. Significant success of different numerical simulations shouldn't persuade us to apply similar numerical methods for the flows which the numerical method has not been properly tuned to handle. Given the complexity and unpredictability of turbulent flows, a combination of numerical and experimental methods is usually applied in order to achieve reliable results.

Among many different numerical methods, Large Eddy Simulation (LES) appears to be very promising and its application is expected to extensively increase in the future. It has already become a user option in different commercial CFD (computational fluid dynamics) packages and an extensive work is underway at different research centers in order to further develop this method.

2.1 Definition and application

The Navier-Stokes equations (NSE) which describe all the flow phenomena in a linear viscous fluid, can be solved directly (without any need for filtration or averaging) for the laminar flows, using different

numerical methods, while for the turbulent flows, the wide range of present eddy scales rules out direct numerical simulation method (DNS). That's specially the case for high Reynolds number flows. Therefore direct numerical simulation of turbulent flows is still out of reach for many industrial flows and most of the DNS simulations which have been carried out in the past were for very simple geometries and at low Reynolds numbers.

In DNS, all the scales from the large energy containing scales (integral scales) to the dissipative scales (Kolmogorov scales) are simulated. DNS is essentially exact and its most important advantage to experiment is that all of the conditions such as initial conditions or boundary conditions that are influential in the flow can be precisely defined. This enables DNS to answer some of the problems and also provide detailed explanations for the probable discrepancies of experimental results.^{58,59}

An alternative approach to DNS is solving the Reynolds-averaged Navier–Stokes (RANS) equations. They are obtained by averaging the Navier–Stokes equations over time, over homogeneous directions, or across an ensemble of equivalent flows. The solution of these equations requires having additional information about the turbulence structure and its relation to the mean flow and therefore it will need a form of turbulence modeling.

Researchers have struggled for quite some time to find a general turbulent model for RANS method that is applicable for a wide range of flows. Unfortunately their attempts have not been successful but have resulted in better understanding of the complex nature of turbulent flows. Even though the subgrid scales compose only a small fraction of the total kinetic energy of the flow, they are far from identical. Their sizes and frequency distribution are different for every flow and their appearance in time and space is quite random. Maybe one of the reasons for this irregular behavior is the remains of old larger structures which have broken into smaller ones. This lack of regularity makes them so difficult to model and therefore it is unlikely to find a simple method for predicting all flows.

Another alternative method for DNS is large eddy simulation (LES) which is discussed in this chapter. The main idea is to resolve the large scale turbulent fluctuations or eddies present in the flow, but to model only the small scales. This method, at least in theory, is superior to RANS because of its ability to resolve more of the complex features of the turbulent flow and therefore to decrease the undesirable effect of the applied turbulence model originated from its inaccuracy.^{42,60–63} In addition, it is less costly than DNS

because it only requires the resolution needed to resolve the most energetic eddies. Given that less energetic eddies are more universal and isotropic, they are preferred to be modeled. ⁶⁴

In LES, the spatially filtered Navier-Stokes equations are numerically solved. The spatial filtering separates and then gathers the effects of small scale eddies in the subgrid scale (SGS) stresses and heat transfer terms. On the other hand, the large energy containing eddies, generated by the older turbulent motions and the dynamic motions inside the flow field and those which are the most interesting in engineering applications are simulated.

As it has been explained in details in Ref. 75, free shear flows at high Reynolds numbers seem to be ideal candidates for LES. For this case, there is a cascade of energy dominantly from the resolved large scales, to the statistically isotropic and universal small scales (Fig. 2.1). There are, therefore, strong reasons to expect LES to be successful for the free shear flows, primary because the quantities of interest and the rate-controlling processes are directly affected by the simulated large scales.

In other applications the situation can be different. For example, in turbulent combustion at high Reynolds number (Ref. 2), molecular mixing and chemical reactions which are the rate-controlling processes occur at the smallest scales. They are not simulated; therefore they have to be modeled the same as in RANS. In this case, LES is not predicted to be very successful; even though it may provide a more realistic prediction of the turbulent flow and therefore obtain more accurate results.

Turbulent boundary layer on the solid walls is another example. In the viscous sublayer the momentum transfer is performed by very tiny structures which are comparable in size to the viscous length scale. In that region there are no large eddies and therefore flow cannot be simulated and it has to be modeled as a result of high computational costs (Refs. 65,66). In this case LES could improve the results but it is not necessarily going to provide the optimal performance. There are many examples of LES done for subsonic and supersonic turbulent boundary layers and transition phenomena (Refs. 67-70) or compression corners (Refs. 71-74) in which good agreement with experimental results has been achieved.

As a conclusion, LES method is supposed to be more reliable when the rate-controlling processes and the affiliated scales are simulated by the method. On the other hand when the rate controlling processes are not simulated and therefore modeled; this modeling causes a fundamental dependency in the results and

therefore LES is expected to perform weaker in these cases. A more detailed discussion about the application of LES has been given in Ref. 75.

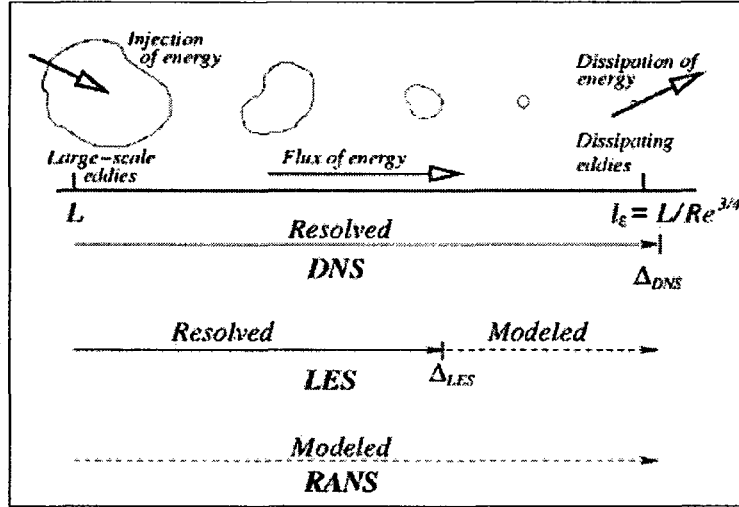


Fig. 2.1 Cascade of energy (Ref. 76).

If we analyze the LES method from the energy point of view, we can say that in LES, the kinetic energy spectrum is decomposed into a resolved part (large scales) and a subgrid part (small scales). It is believed that large eddies are responsible for transports of momentum, energy, and scalars. As it was mentioned in Refs. (75-77) they are assumed to be “anisotropic, subjected to history and nonequilibrium effects, and strongly dependent on geometry and boundary conditions, which make their modeling difficult. Small eddies instead tend to be more isotropic and less flow dependent (universal), which makes their modeling easier”.

Let's assume that we would like to solve the NSE inside a domain with periodic boundary conditions. Let $\hat{u}(K) = FT(\bar{u})$ represent the Fourier transform of the velocity field with dual variable $K(k_1, k_2, k_3)$ in which:

$$k = |K| = (k_1^2 + k_2^2 + k_3^2)^{1/2} \quad (2.1)$$

Energy spectrum is defined as:

$$E(k, t) = \frac{1}{2} \int_{k=0}^{k=|K|} \sum_{i=1}^3 |\hat{u}_i(k)|^2 dk \quad (2.2)$$

and

$$E(k) = \lim_{T \rightarrow \infty} \frac{1}{T} \int_0^T E(k, t) dt \quad (2.3)$$

If the data is plotted on $(\log(k), \log E(k))$ axes, a universal pattern will be discovered (see, e.g., Refs. 77-80). As it is shown in Fig. 2.2, the spectrum starts by a peak at relatively low wave-numbers, which its length scale is an important characteristic of the turbulence and is approximately the integral length scale, L (See Ref. 57):

$$L = \frac{\pi}{2 \times \frac{2}{3} \int_0^{\infty} E(k) dk} \int_0^{\infty} E(k) / k dk = \frac{3\pi \times \int_0^{\infty} E(k) / k dk}{4 \times \int_0^{\infty} E(k) dk} \quad (2.4)$$

After this peak, there is the integral subrange region, whose length is different from a flow to another and is a function of Reynolds number. In this region, $E(k)$ profile has the form of $k^{-5/3}$ through a wide range of wave-numbers. The spectrum finally ends by a sharp decrease at the viscous dissipation-dominated region, whose wave length is scaled by the Kolmogorov scale (η).

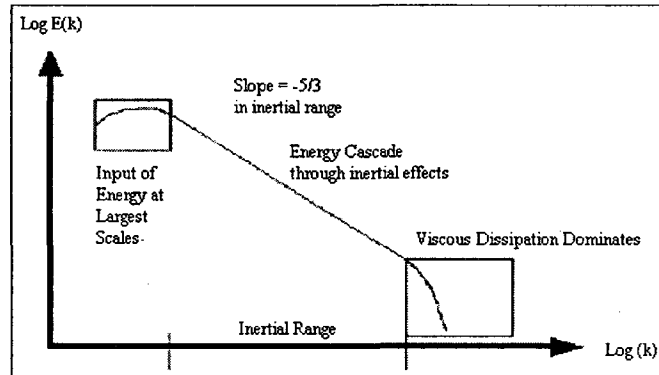


Fig. 2.2 A depiction of observed energy spectrum for isentropic turbulence.

In an LES, it is usually agreed that the computational domain must be as large as the largest turbulent eddy in the flow and therefore its dimensions must be as long as few integral length scales (L). On the

other hand, the grid spacing should not be very smaller than Kolmogorov scale (η) because there is no eddy smaller than that size.

Kolmogorov has provided a theoretical analysis for the inertial subrange (Ref. 81). Considering a region inside a high Reynolds number flow, far away from the solid walls and after passing a long period of time, we can assume that time averages of turbulent quantities depend only on one number, the time-averaged energy dissipation rate:

$$\bar{\epsilon} = \lim_{T \rightarrow \infty} \frac{1}{T} \int_0^T \epsilon(t) dt \quad (2.5)$$

As it has been shown in Layton (2002),⁸¹ two important consequences of the Eq. 2.5 are that the smallest eddy in a turbulent flow has the diameter of $O(\text{Re}^{-3/4})$ and $E(k)$ must take the universal form

$$E(k) = \alpha(\bar{\epsilon})^{2/3} (k)^{-5/3}, \alpha \cong 1.4 \quad (2.6)$$

inside the inertial range. The time-averaged energy dissipation rate ($\bar{\epsilon}$) will be supposedly unique for every turbulent flow. The first estimate of $O(\text{Re}^{-3/4})$ also leads to the required grid resolution of $O(\text{Re}^{-9/4})$ for the DNS of turbulent flows in 3D space.

When a numerical method is used for the LES of turbulent flows, it should be capable to emulate the energy transport with an appropriate slope of $-5/3$ (in log-log domain) at regions where an isotropic fully developed turbulent flow is expected to be present. It is important to mention that turbulence in general is not an equilibrium phenomenon therefore we should be very careful about the conclusion drawn about the slope as well as the behavior of the inertial range. The analysis presented above has been highly simplified. There are even some processes, such as vortex roll-up and pairing that transfer energy from the small scales to larger ones. As mentioned in Ref. 57, there are perhaps many other processes which yet remain to be discovered.

As it was mentioned in Refs. (82,83), based on the conditions, the following parameters affect the quality of an LES:

- The discretization scheme, which affects any LES solution but becomes also responsible of sub-grid scale closure in the implicit LES approach.
- The sub-grid scale model (for non-implicit LES).
- The explicit filtering procedure (for the modeling approaches that require explicit filtering), and the associated filter function (especially for the unstructured implementation).
- The mesh quality and resolution

Each one of these parameters could be assumed to be as a filtering function or an error term (modeling error or numerical error), applied or added to the solved equations. They can potentially have very different behaviors in the spectral domain; sometimes positive but also could be negative, and the final result is always affected by cumulative effects of them together.

As it has been mentioned in Ref. 12, second order schemes are usually the choice for unstructured grids and because of their low order accuracy, normally they generate a strong numerical dissipation which dominates over the subgrid scale term and completely affects its performance. This is obviously an example of negative interaction between the subgrid model and the error terms originated from the applied numerical method. As another example for destructive interaction, in some LES simulations sometimes a theoretically unacceptable situation occurs, where the resolved total turbulent kinetic energy of the LES is greater than the total turbulent kinetic energy of an equivalent DNS (Ref. 83). It is expected that after filtering the DNS results, the amount of turbulent kinetic energy decreases, simply because the turbulent kinetic energy of the subgrid scales supposedly will be absent. However erroneous components which affect the simulation may result into a surprising outcome.

Based on the discussion given in Ref. 82, when the filter size is a function of the grid's size, a good LES is the one which leads to DNS as the grid is refined more towards the Kolmogorov scales. Grid-independent LES under this condition doesn't exist in theory, because a grid independent LES is essentially DNS and the philosophy of LES loses its meaning if it is grid independent. As it was proposed in Ref. 83, the best approach to assess the quality of an LES is to compare the amount of the resolved turbulent kinetic energy to the total turbulent kinetic energy. A good LES should resolve at least 80% of the total turbulent kinetic energy. It is not however an easy task to have an estimate for the total kinetic energy and usually a sort of experimental measurement is required.

Finally, it should be mentioned that in RANS, generally speaking, unsteady motions are regarded as turbulence and therefore turbulence models are usually designed to remove all the unsteadiness in the flow. It sometimes happens that a RANS simulation doesn't converge to a steady state solution and an unsteady result is produced. It may be claimed that these simulations are a form of LES but, given the original purpose and design of RANS turbulence model, this claim doesn't seem to be very convincing and a careful assessment is needed before using the results of such simulations.

2.2 Governing Equations

For an arbitrary function $f(x_i, t)$, filtering is defined as:

$$\bar{f}(x_i, t) = \int_D G(x_i - \xi_i, \Delta) f(\xi_i, t) d\xi_i \quad (2.7)$$

Δ is the filtering size and is related to the size of the computational mesh. For compressible flows the Favre-filtering operation is defined as:

$$\tilde{f}(x_i, t) = \frac{\overline{\rho f}}{\rho} \quad (2.8)$$

By this definition, a variable is decomposed into its Favre-filtered component and fluctuating component according to:

$$f(x_i, t) = \tilde{f}(x_i, t) + f''(x_i, t) \quad (2.9)$$

If we assume that the filtering operations commute with the derivative operators and then apply the definitions in Eqs. (2.7,2.8) to the compressible Navier-Stokes equations; the filtered governing equations are obtained as follows:^{63,65,84,85}

$$\frac{\partial \bar{\rho}}{\partial t} + \frac{\partial \bar{\rho} \tilde{u}_i}{\partial x_i} = 0 \quad (2.10)$$

$$\frac{\partial \bar{\rho} \tilde{u}_i}{\partial t} + \frac{\partial \bar{\rho} \tilde{u}_i \tilde{u}_j}{\partial x_j} = -\frac{\partial \bar{p}}{\partial x_i} + \frac{\partial (\tau_{ij} + \tilde{\sigma}_{ij})}{\partial x_j} \quad (2.11)$$

$$\frac{\partial \bar{\rho} \tilde{e}}{\partial t} + \frac{\partial (\bar{\rho} \tilde{e} + \bar{p}) \tilde{u}_j}{\partial x_j} = \frac{\partial \left(Q_j + \frac{\mu(\tilde{T}) C_p}{\text{Pr}} \frac{\partial \tilde{T}}{\partial x_j} + (\tau_{ij} + \tilde{\sigma}_{ij}) \tilde{u}_i \right)}{\partial x_j} \quad (2.12)$$

$$\bar{p} = \bar{\rho} R \tilde{T} \quad (2.13)$$

\tilde{e} is the filtered total energy per unit mass and is defined as:

$$\bar{\rho} \tilde{e} = \bar{\rho} c_v \tilde{T} + \frac{1}{2} \bar{\rho} \tilde{u}_i \tilde{u}_i \quad (2.14)$$

The molecular viscous stress tensor $\tilde{\sigma}_{ij}$ is approximated by:

$$\tilde{\sigma}_{ij} = \mu(\tilde{T}) \left(-\frac{2}{3} \frac{\partial \tilde{u}_k}{\partial x_k} \delta_{ij} + \frac{\partial \tilde{u}_i}{\partial x_j} + \frac{\partial \tilde{u}_j}{\partial x_i} \right) \quad (2.15)$$

where $\mu(\tilde{T})$ is molecular viscosity and is calculated by Sutherland equation:

$$\mu(\tilde{T}) = (1.711 \times 10^{-5}) \left(\frac{\tilde{T}}{273.15} \right)^{2/3} \left(\frac{383.55}{\tilde{T} + 110.4} \right) \quad (2.16)$$

The applied notation may be further simplified by dropping the tittle and overbar signs and also non-dimensionalize the equations using the reference values $(\rho_\infty, U_\infty, \rho_\infty U_\infty^2, L, T_\infty)$. The governing equations therefore become in the following form assuming that $\bar{F}^{conv} = (F_1^{conv}, F_2^{conv}, F_3^{conv})$ and $\bar{F}^{diff} = (F_1^{diff}, F_2^{diff}, F_3^{diff})$:

$$\frac{\partial q}{\partial t} + \text{div}(\bar{F}^{conv} + \bar{F}^{diff}) = 0 \quad (2.17)$$

$$q = \begin{Bmatrix} \rho \\ \rho u_1 \\ \rho u_2 \\ \rho u_3 \\ \rho e \end{Bmatrix} \quad (2.18)$$

$$F_j^{conv} = \begin{Bmatrix} \rho u_j \\ \rho u_j u_1 + p \delta_{j1} \\ \rho u_j u_2 + p \delta_{j2} \\ \rho u_j u_3 + p \delta_{j3} \\ u_j (\rho e + p) \end{Bmatrix} \quad (2.19)$$

$$F_j^{diff} = \begin{Bmatrix} 0 \\ -\sigma_{j1} - \tau_{j1} \\ -\sigma_{j2} - \tau_{j2} \\ -\sigma_{j3} - \tau_{j3} \\ -\frac{\mu(\tilde{T}) C_p}{\text{Pr}} \frac{\partial \tilde{T}}{\partial x_j} - Q_j - u_k (\sigma_{kj} + \tau_{kj}) \end{Bmatrix} \quad (2.20)$$

2.3 Subgrid Scale Models

In the Eqs. (2.10-2.12), τ_{ij} and Q_j are the subgrid scale stress tensor and the subgrid scale heat flux respectively and they need to be modeled. According to Ref. 48, there are two main strategies in order to address the challenge of subgrid modeling:

- **Functional modeling:** in this method the overall action of the subgrid tensors are approximated by introducing appropriate dissipative or dispersive terms and function into the simulation. ($\frac{\partial \tau_{ij}}{\partial x_j} = F_1(\bar{u}_i)$ and $\frac{\partial Q_j}{\partial x_j} = F_2(\bar{u}_i)$)
- **Structural modeling:** in this method different approximations of the subgrid scale tensors, based on the resolved flow field are considered ($\tau_{ij} = F_1(\bar{u}_i)$ and $Q_j = F_2(\bar{u}_i)$)

In the functional modeling approach, it is generally assumed that the modeled scales are influencing the resolved scales mainly through the energy exchange mechanism which takes place between the resolved and modeled scales. These models can be categorized in three main categories:

- Models based on the resolved scales (such as Smagorinsky model⁸⁶)
- Models based on the energy at the cutoff scale (such as Structure Function model)
- Models based on the subgrid scales (such as Yoshizawa model)

The structural models, on the other hand, are built without considering any knowledge about the nature of the interactions between the subgrid and resolved scales. They can be categorized in several groups:

- Models based on formal series expansions (such as models based on approximate deconvolution or Kosovic's simplified Non-linear Model)
- Differential Subgrid Stress models which are based on transport equations for the subgrid tensor components (such as Deardorff model)

- Deterministic Models of the subgrid structures which are constructed using different assumptions about the structure of subgrid scales (such as S3/S2 Alignment model)
- Models based on Scale Similarity hypothesis (such as Bardina model)
- The mixed models which are based on liner combinations of the functional and structural types (such as Smagorinsky-Bardina model)
- Models based on an explicit reconstruction of the subgrid velocity fluctuations(such as chaotic map model)
- Implicit structural models based on specific numerical algorithms, whose errors are designed to mimic the subgrid forces (MILES) (such as scale residual model)

The functional models generally provide a more accurate and realistic energy transfer between resolved and subgrid scales. However the structural models better approximate the structure of subgrid tensor and therefore are better capable to capture anisotropic effects and disequilibrium in the flow. In this work the Smagorinsky subgrid model is implemented and is described in details in the next section.

2.3.1 Smagorinsky Subgrid Scale Model

The τ_{ij} is the subgrid scale stress tensor which is modeled by compressible extension of the Smagorinsky subgrid-scale as follows:

$$\tau_{ij} = -(\overline{\rho u_i u_j} - \bar{\rho} \tilde{u}_i \tilde{u}_j) = \bar{\rho} C_S \Delta^2 \sqrt{\tilde{S}_{kl} \tilde{S}_{kl}} (2\tilde{S}_{ij} - \frac{2}{3} \tilde{S}_{kk} \delta_{ij}) \quad (2.21)$$

The rate-of-strain tensor is defined as:

$$\tilde{S}_{ij} = \frac{1}{2} \left(\frac{\partial \tilde{u}_i}{\partial x_j} + \frac{\partial \tilde{u}_j}{\partial x_i} \right) \quad (2.22)$$

and the model for the filtering size is:

$$\Delta = (Vol(C_i))^{1/3} \quad (2.23)$$

where $Vol(C_i)$ is the volume of cell C_i which belongs to node i .

The Q_j is the subgrid scale heat flux and is modeled using eddy viscosity model:

$$Q_j = -c_p (\overline{\rho u_j T} - \bar{\rho} \tilde{u}_j \tilde{T}) = \bar{\rho} C_p \frac{C_S}{Pr_t} \Delta^2 \sqrt{\tilde{S}_{kl} \tilde{S}_{kl}} \frac{\partial \tilde{T}}{\partial x_j} \quad (2.24)$$

in which $Pr_t = 0.6$.

2.4 Statistical Analysis of Turbulence

In order to study the fluctuating quantities of turbulent flows, statistical analysis is needed to be performed.

It would enable us to define and calculate the average and the fluctuating quantities for different variables and therefore makes it possible to qualitatively compare the numerical results with experimental data. We assume that $X(j), j = 0, \dots, N-1$ is a set of data with N different data samples. The statistical definitions, used in the proceeding chapters are as follows:

- The **average value** of a variable (X_j) is calculated as:

$$\bar{X} = \frac{\sum_{j=0}^{N-1} X_j}{N} \quad (2.25)$$

in which N is the total number of available data points.

- **Root-mean-square** is defined as follows:

$$X_{rms} = \sqrt{\frac{\sum_{j=0}^{N-1} (X_j - \bar{X})^2}{N}} \quad (2.26)$$

Chapter 3

Numerical Method

3.1 Numerical method for LES

THE importance of applying accurate numerical methods in LES, especially when it involves an upwinding term in the flux calculation has been previously reported in the literature.^{6,69,87} The upwind schemes, regardless of the applied numerical method, add some artificial dissipation and therefore are known to be much more stable than central difference schemes and have been used successfully in the past for RANS simulations. This additional dissipation however can negatively influence the accuracy. Spyropoulos and Blaisdell (1998),⁶⁹ used a 5th order, upwind-biased finite difference scheme for the inviscid flux calculation in order to simulate a spatially evolving supersonic boundary layer. They recognized the fact that the upwinding schemes provide artificial dissipation, and therefore they preferred to use the upwind-biased scheme. Mary and Sagaut (2002),⁸⁷ used a 2rd order MUSCL, cell-centered control volume scheme in order to simulate the flow around an airfoil near stall using structured multi-block meshes. They applied a sensor in order to minimize the numerical dissipation originated from the upwinding. Andersson et al. (2005),⁶ simulated a compressible jet using a 3rd order upwinding scheme in which the contribution of the upwinding term was decreased to one eighth in order to make the numerical method less dissipative.

The additional dissipation of a numerical method highly depends on the nature of the emulated flow and the local resolution of the grid, and under some circumstances it can even be higher than the dissipation of applied subgrid scale model. That is specially the case when a low order numerical discretization as the one applied in this research is used. For example, Hahn and Drikakis (2005),⁸⁸ simulated the decaying

turbulence and the compressible flow around open cavities for low and high Reynolds numbers. They concluded that the numerical dissipation of their numerical method was satisfactory and therefore addition of an explicit subgrid model (SGS) was not justifiable.

In this dissertation a 2nd order Roe-MUSCL flux calculation ($\beta\gamma$ scheme) is used for the LES and the objective is to evaluate and possibly control its numerical dissipative error. In the Roe-MUSCL ($\beta\gamma$ scheme) flux calculation, the contribution of the upwinding term is adjusted using a coefficient (γ) which is directly multiplied into that term during the flux calculation. Coefficient (β) is also used in order to predict the value of variables at the boundaries of control volume cells.

A complete analysis of the accuracy of Roe-MUSCL ($\beta\gamma$ scheme) and its relation to the structure of generated grid has been reported by Carpentier (1980).⁸⁹ In that study, the dissipative and dispersive error terms of 2D advection equation have been analyzed using two different meshes (a uniformly distributed triangular mesh and a structured quadrangular mesh). He concluded that the $\beta = 1/3, \gamma = 0.0$ will result in 4th order dispersive error and 5th order dissipative error. This high order dissipative error requires the scheme not to have any upwinding ($\gamma = 0.0$). It was also observed that these error terms were functions of the CFL number related to the applied 4th order Runge-Kutta time discretization scheme. If $\beta = 1/3$ but $\gamma \neq 0.0$ then the dissipative error will be 3rd order while the dispersive error will still remain 4th order. In addition, it was also found that the uniform triangular mesh potentially has higher dispersive and dissipative error in comparison to quadrangular mesh.

As a result, there have been several attempts in order to lower the applied value of γ and consequently decrease the numerical dissipation of the flux calculation method. For example Bui (1999),⁹⁰ simulated the turbulent flow inside a square duct using Roe scheme and using a structured grid. He tried to use the smallest possible value of γ for which the simulation was still stable. Camarri et al. (2002),⁶¹ applied a 2nd order mixed finite volume-finite element code using Roe-MUSCL method in order to study the contribution of upwinding to the numerical dissipation and its interaction with SGS. They also used the lowest possible fraction of the upwinding term in order to minimize the dissipative error and also satisfy the

stability condition of the simulation. In all of these cases, several simulations were needed to be carried out in order to determine the lowest value of γ that was still able to keep the simulation stable.

Ciardi et al. (2005),¹² recently developed a new scheme for the unstructured meshes based on finite volumes for inviscid and viscous flux calculations. They adjust the contribution of upwinding term using a wiggle detector and therefore there is no need for several simulations to determine the lowest value of γ . In their method the objective is to completely damp the wiggles of a certain size detected by the sensor. This method however, can partially lead to damping the energy in the smallest scales captured in the simulation. Since in LES, the smallest scales of simulation fall within the inertial subrange, it is necessary to preserve the energy of such scales.⁵⁷

In this dissertation a new self-adaptive upwinding method, inspired by Refs. 12 and 13, is developed and implemented. This method is compatible with classic numerical scheme for compressible flows, based on Roe-MUSCL ($\beta\gamma$ scheme) and is also applicable to unstructured grids. It uses a wiggle detector which has been inspired by Ref. 91. The wiggle detector proposed by Ref. 12 detects the wiggles along three consecutive edges which are not necessarily collinear and it could lead to some uncertainty. Therefore a new method, for wiggle detection is proposed here which is expected to be more reliable. In addition, the developed scheme does not completely damp the wiggles detected by the wiggle detector, but instead permits some wiggles to develop up to a preset threshold of intensity inside the computational domain. The importance of that will be shown in the validation step to be crucial in order to adjust the slope of the energy spectrum.

It is generally agreed that turbulent flows are characterized by their unsteadiness and unpredictability and the largest part of the turbulent energy is constructed by truly random motions which could be the remains of old coherent structures.⁵⁷ We also know that in a typical simulation, whenever the grid resolution is not high enough to capture all the scales of the flow (LES), application of a central scheme would generate random fluctuations and wiggles. That is the case when γ is lowered by the wiggle detector. As a result, the developed scheme introduces a degree of randomness into the solution which could be favorable and generate more realistic results.

The applied numerical method in this work is a mixed finite volume-finite element method,^{84,92} which has been developed to solve the unsteady Navier-Stokes equations. It operates on unstructured grids, using 2nd order Roe-MUSCL upwind formulation ($\beta\gamma$ scheme) for the convective fluxes and a 2nd order finite element method for the diffusive fluxes. As it was mentioned in the chapter 2, subgrid scale terms are modeled by the Smagorinsky model. A second order implicit scheme is also used for the temporal discretization. The system of equations is then solved, using an iterative GMRES solver and MPI parallel programming. In our simulations, reference 93 has been used for the purpose of parallel programming.

3.2 Spatial Discretization

In order to spatially discretize and then numerically solve the problem, the weak formulation of the averaged Navier-Stokes is written by multiplying a test function to the Eq. (2.17) and then integrating it on the entire spatial domain (Ω):

$$\int_{\Omega} \left(\frac{\partial q}{\partial t} \Psi + \text{div} \bar{F}^{conv}(q) \Psi \right) dv = \int_{\Omega} [-\text{div}(\bar{F}^{diff}(q)) \Psi] dv \quad (3.1)$$

Then Ω is discretized into separate C_i cells which don't have any overlapping. This approach will break the Eq. (3.1) into sub-equations for every of those cells. The result would be the discrete formulation for every cell (Eq. (3.2)). These equations are obtained by using the characteristic function ϕ_i of the finite volume cell C_i as the test function for the convective part of the equation and the piecewise linear finite element basis function ϕ_i as the test function for the diffusion term:

$$\int_{C_i} \left(\frac{\partial q}{\partial t} + \text{div} \bar{F}^{conv}(q) \right) \phi_i dv = \int_{\sum C_i} [-\text{div}(\bar{F}^{diff}(q)) \phi_i] dv \quad (3.2)$$

Green's theorem now is applied to the convective fluxes, while the viscous terms are integrated by parts. After some manipulations, the variational formulation is achieved as follows:

$$\int_{C_i} \frac{\partial q}{\partial t} dv + \int_{\partial C_i} [\bar{F}^{conv}(q) \cdot \bar{n}_i] d\sigma = \int_{\sum C_i} [\bar{F}^{diff}(q) \cdot \text{div}(\phi_i)] dv - \int_{\Gamma} [(\bar{F}^{diff}(q)\phi_i) \cdot \bar{m}] d\sigma \quad (3.3)$$

where \bar{n}_i is the outward unit vector to the boundary (∂C_i) of cell C_i (Fig. 3.1), such that $\bar{n}_i = (n_{ix} + n_{iy} + n_{iz})$ and \bar{m} is the outward unit vector to the boundary (Γ) of elements ($\sum C_i$) sharing node i . Since the viscous part of the compressible NSE is parabolic, it is discretized using an accurate finite element method. The integral term $\int_{\Gamma} [(\bar{F}^{diff}(q)\phi_i) \cdot \bar{m}] d\sigma$ appears to be small therefore it is not considered.

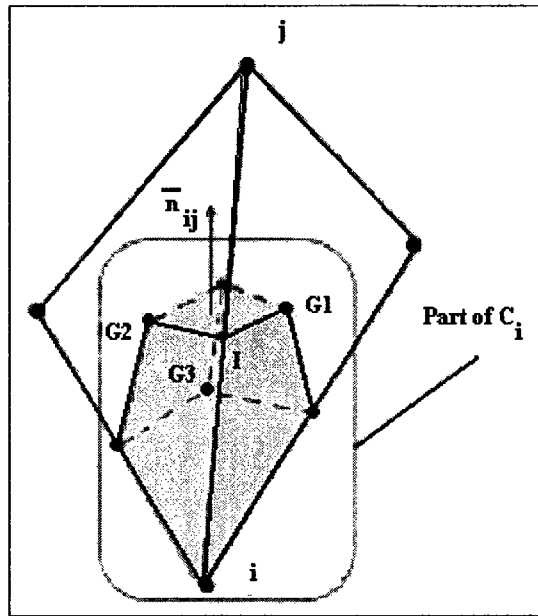


Fig. 3.1 Share of the cell C_i from an adjacent tetrahedron.

3.2.1 Convective Flux Calculation

Roe-MUSCL method is the base for the convective flux calculation in this work. In this method the normal component of the inviscid flux at the boundaries of neighboring cells is defined as a sum of an average term calculated by fluxes of two nodes belonging to the edge which the flux is calculated along it and an upwinding term.

$$\bar{F}^{conv} \cdot \bar{n}_{ij} = \frac{1}{2} (\bar{F}^{conv}(q_+) + \bar{F}^{conv}(q_-)) \cdot \bar{n}_{ij} - \frac{1}{2} |\hat{A}(\hat{q}, \bar{n}_{ij})| (q_+ - q_-) \quad (3.4)$$

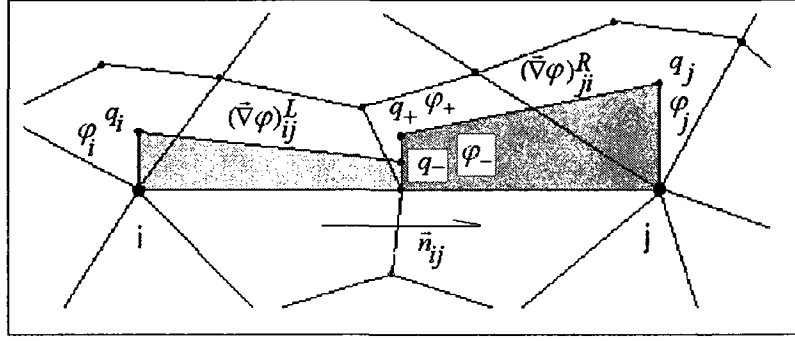


Fig. 3.2 Control volumes and convective flux calculation.

\hat{q} is the average value of q_- and q_+ evaluated at the boundary of a cell or control volume using Roe method. q_- and q_+ are calculated using φ_- and φ_+ which are obtained by approximating the numerical primitive variables of those two nodes at the boundaries of the cell ∂C_i (inter nodal values between nodes i and j) using the following equations:

$$\begin{aligned} \varphi_+ &= \varphi_j - \frac{1}{2} g(\Delta\varphi^C, \Delta\varphi_{ij}^R) \\ \varphi_- &= \varphi_i + \frac{1}{2} g(\Delta\varphi^C, \Delta\varphi_{ij}^L) \end{aligned} \quad (3.5)$$

in which $\Delta\varphi_{ij}^L = (1-\beta)(\varphi_j - \varphi_i) + \beta(\bar{\nabla}\varphi)_{ij}^L \cdot (\bar{X}_j - \bar{X}_i)$, $\Delta\varphi_{ij}^R = (1-\beta)(\varphi_j - \varphi_i) + \beta(\bar{\nabla}\varphi)_{ij}^R \cdot (\bar{X}_j - \bar{X}_i)$, $\Delta\varphi^C = \varphi_j - \varphi_i$ and $\varphi = [\rho, u, v, w, p]$ is the primitive variables' vector. This approach is used in order to improve the precision of the method without changing the approximation space.^{84,92}

The parameter β determines to what extent central interpolation is used in order to calculate φ_+ and φ_- . As it has been recommended in Ref. 89, we set the value of β equal to 1/3 in order to minimize the dissipative and dispersive errors. $(\bar{\nabla}\varphi)_{ij}^L$ and $(\bar{\nabla}\varphi)_{ij}^R$ are defined as left hand and right hand gradients (Figs. 3.2). These gradients are computed respectively on the upstream (L) and downstream (R) tetrahedrons associated with edge ij (Fig. 3.3). Local average gradients also can be used as an approximation. This is an extension of the MUSCL method to the finite element, because the gradient of the primitive variables' vector (φ) is computed using the finite element technique.

Since Roe-MUSCL scheme is based on a linear approximation of the variables in every cell to the boundaries, it can generate oscillations close to the discontinuities. In order to solve this problem, the

values of gradients used in the approximation are bounded using a nonlinear function. This function is called limiter function ($g(x, y)$) and it gives the MUSCL scheme the needed TVD property. In our simulations, the Van Leer–Van Albada limiter is applied and it has the following definition:

$$g(x, y) = \begin{cases} 0 & xy < 0 \\ \frac{(x^2 + \varepsilon)y + (y^2 + \varepsilon)x}{x^2 + y^2 + \varepsilon} & xy \geq 0 \end{cases} \quad (3.6)$$

in which ε is usually a very small number and in our simulations it is set to 10^{-16} .

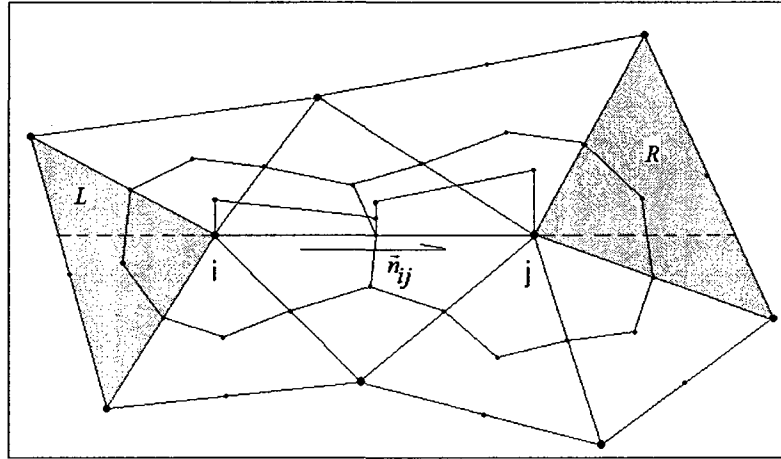


Fig. 3.3 Convective flux calculation.

3.2.2 Self-Adaptive Upwinding Scheme

The Roe-MUSCL scheme has given good results for Euler or laminar simulations but it has been found to be too dissipative for the LES.^{13,61,90} In order to control the amount of Roe upwinding dissipation a coefficient (γ) is used, such that:

$$\bar{F}^{conv} \cdot \bar{n}_{ij} = \frac{1}{2} (\bar{F}^{conv}(q_+) + \bar{F}^{conv}(q_-)) \cdot \bar{n}_{ij} - \gamma \left\{ \frac{1}{2} |\hat{A}(\hat{q}, \bar{n}_{ij})| (q_+ - q_-) \right\} \quad (3.7)$$

where γ can change between 0 and 1. In Eq. (3.7), $\gamma=0$ corresponds to central differencing, and $\gamma=1$ corresponds to the full Roe-MUSCL method. Omitting the Roe upwinding term altogether ($\gamma=0$) causes all

calculations to be unstable therefore for a given grid size, a minimum amount of upwinding dissipation is always required in order to provide stability. In general, a finer grid would require a smaller value of γ .

In order to determine and adjust upwinding parameter (γ) dynamically, a wiggle detector has been implemented. It checks to see if the intensity of the local wiggle is higher than a preset value. If this is the case then the scheme increases γ towards the full Roe-MUSCL scheme, using a linear function. Otherwise the scheme is more centered and γ is decreased.

In the present computations we extend the wiggle definition, given in Ref. 91 for our numerical method. A wiggle is assumed to be present along an arbitrary edge, if the gradients change sign twice along that edge. That is, if for any flow primitive variable Φ ($\Phi \in \varphi = [\rho, u, v, w, p]$)

$$(\Phi_i - \Phi_{i-1})(\Phi_{i+1} - \Phi_i) < 0 \quad (3.8)$$

$$(\Phi_{i+2} - \Phi_{i+1})(\Phi_{i+1} - \Phi_i) < 0 \quad (3.9)$$

are true, then a wiggle is present. A simplified example is illustrated in Fig. 3.4. In this example there is a wiggle along the edge connecting nodes i and $i+1$, but there is no wiggle along the edge connecting nodes $i-1$ and i .

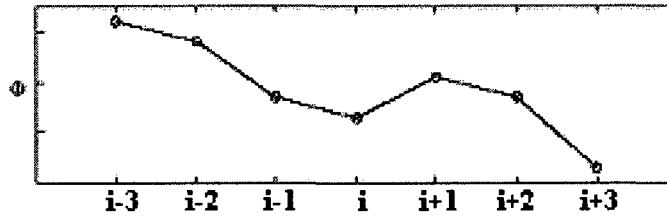


Fig. 3.4 The definition of a wiggle in the present computations (Ref. 91).

A new method is developed here to be a more general and appropriate approach for the purpose of LES. Let's consider a tetrahedron having ij as an edge (Fig. 3.3). Along ij we compute $(\bar{\nabla}\Phi)^C$ ("C" as centered) which $(\bar{\nabla}\Phi)^C \cdot \bar{n}_{ij} = (\Phi_j - \Phi_i) / |\bar{X}_j - \bar{X}_i|$. \bar{X}_i and \bar{X}_j are the position vectors of nodes i and j respectively. Now we replace the inequalities (3.8,3.9) with the followings:

$$[(\bar{\nabla}\Phi)_{ij}^L \cdot \bar{n}_{ij}][(\bar{\nabla}\Phi)^C \cdot \bar{n}_{ij}] = [(\bar{\nabla}\Phi)_{ij}^L \cdot \bar{n}_{ij}][(\Phi_j - \Phi_i) / |\bar{X}_j - \bar{X}_i|] < \theta \leq 0 \quad (3.10)$$

$$[(\bar{\nabla}\Phi)_{ji}^R \cdot \bar{n}_{ij}] [(\bar{\nabla}\Phi)^C \cdot \bar{n}_{ij}] = [(\bar{\nabla}\Phi)_{ji}^R \cdot \bar{n}_{ij}] [(\Phi_j - \Phi_i) / |\bar{X}_j - \bar{X}_i|] < \theta \leq 0 \quad (3.11)$$

If inequalities (3.10,3.11) are satisfied then the local wiggle's intensity is more than the preset value (θ) and γ should be increased. This increment is a linear function of $\theta - \text{Min}\{[(\bar{\nabla}\Phi) \cdot \bar{n}_{ij}] [(\bar{\nabla}\Phi)^C \cdot \bar{n}_{ij}]\}$. On the other hand, when inequalities (3.10,3.11) are not satisfied, it implies that the intensity of the wiggle is less than the preset value (θ) and γ can be decreased. This time, the decrement would be a linear function of $\text{Max}\{[(\bar{\nabla}\Phi) \cdot \bar{n}_{ij}] [(\bar{\nabla}\Phi)^C \cdot \bar{n}_{ij}]\} - \theta$.

In both linear functions, $(\bar{\nabla}\Phi) \in [(\bar{\nabla}\Phi)_{ij}^L, (\bar{\nabla}\Phi)_{ji}^R]$, $\Phi \in [\rho, u, v, w, p]$ and the value of (γ) is chosen between 0 and 1. The value of θ is either negative or zero and usually has a small absolute value (≈ -0.00001 to -0.0001). The idea is to use the products of the gradients as a way to measure the intensity of a local wiggle.

For DNS, the grid is fine enough to capture the smallest scales of eddies present in the flow field. Therefore the highest mode of the flow's energy spectrum ($E(k)$) is lower than the highest mode that the numerical method can capture. In other words, the smallest eddies present in the flow have an average diameter which is fairly bigger than local average size of the grid (h) and therefore no energy is expected to be present in the scales belonging to h . It implies that there should not be any local wiggle present in the flow and θ in the non-equalities (3.10,3.11) must be set to zero.

For LES, however, the situation is different because even in the best cases, the cutoff mode is expected to fall within inertial subrange and therefore there will be some energy in the highest scales which are expected to be captured by the simulation. Therefore, θ is replaced by a negative and relatively small value which will represent the existence of energy in the smallest scales and by changing the value of θ , the amount of that energy is adjusted.

Considering the high computational resources, required for some of the simulations that will be explained in details during the coming chapters, application of the parallel computational method is unavoidable and therefore, parallelization of the self-adaptive upwinding scheme is necessary. In order to parallel the proposed scheme, for every edge that is connected to a node which belongs to the boundaries of a specific subdomain, a search is carried out among all the elements of its own neighboring as well as the

subdomains which share that particular node. During that search, the best candidates for the upstream (L) and downstream (R) tetrahedrons are determined. During the following iterations, the values of those preselected elements are used by the wiggle detector to do the required calculations and therefore the numerical method remains consistent everywhere within the domain.

3.3 Temporal Discretization

The spatial discretization procedure described above leads to a discretized formulation which has to be integrated in time. We use a second order implicit scheme in order to perform the time integration. The governing equation for every cell (Eq. (3.3)) can be rewritten by taking the temporal term to left hand side and the rest of the terms to the right hand side of the equation as:

$$\int_{C_i} \frac{\partial q}{\partial t} dv = \sum_j K(q_i, q_j) \quad (3.12)$$

q_i is the variable vector of the cell C_i and q_j represents the variable vector of any other cell C_j which is exchanging flux with C_i . The discretized temporal term is integrated by assuming constant q_i over the cell C_i :

$$Vol(C_i) \frac{\partial q}{\partial t} \Big|_i^n = \sum_j K(q_i, q_j) \quad (3.13)$$

For 1st order approximation $\frac{\partial q}{\partial t} \Big|_i^n$ can be replaced by $\frac{\Delta q_i^n}{\Delta t^n}$, in which $\Delta q_i^n = q_i^{n+1} - q_i^n$ and $\Delta t^n = t^{n+1} - t^n$.

In order to implement an implicit temporal method, right hand side of Eq. (3.12) is evaluated at time $n+1$. Therefore the equation is rewritten as follows:

$$Vol(C_i) \frac{\partial q}{\partial t} \Big|_i^n = \sum_j K(q_i^{n+1}, q_j^{n+1}) \quad (3.14)$$

Right hand side now can be approximated and more expanded in order to achieve a 2nd order accurate scheme:

$$\begin{aligned}
\sum_j K(q_i^{n+1}, q_j^{n+1}) &\cong \sum_j K(q_i^n, q_j^n) + \sum_j \left(\frac{\partial K(q_i, q_j)}{\partial q_i} \frac{\partial q_i}{\partial t} \right)^n \Delta t^n \\
&+ \sum_j \left(\frac{\partial K(q_i, q_j)}{\partial q_j} \frac{\partial q_j}{\partial t} \right)^n \Delta t^n + \sum_j \left(\frac{\partial K(q_i, q_j)}{\partial q_i} \frac{\partial^2 q_i}{\partial t^2} \right)^n \frac{(\Delta t^n)^2}{2} + \\
&+ \sum_j \left(\frac{\partial K(q_i, q_j)}{\partial q_j} \frac{\partial^2 q_j}{\partial t^2} \right)^n \frac{(\Delta t^n)^2}{2} + O((\Delta t^n)^2)
\end{aligned} \tag{3.15}$$

Derivative terms in Eq. (3.15) are replaced by:

$$\begin{aligned}
\left. \frac{\partial(q_i)}{\partial t} \right|^n &= \frac{(1+2\tau)/(1+\tau)q_i^{n+1} - (1+\tau)q_i^n + \tau^2/(1+\tau)q_i^{n-1}}{\Delta t^n} = \frac{(1+2\tau)/(1+\tau)\Delta q_i^n - \tau^2/(1+\tau)\Delta q_i^{n-1}}{\Delta t^n} \\
\left. \frac{\partial(q_i)}{\partial t} \right|^n &= \frac{(a)(\Delta q_i^n) - (b)(\Delta q_i^{n-1})}{\Delta t^n}
\end{aligned} \tag{3.16}$$

$$\begin{aligned}
\left. \frac{\partial^2(q_i)}{\partial t^2} \right|^n &= \frac{2\tau/(1+\tau)q_i^{n+1} - (2\tau)q_i^n + (2\tau^2)/(1+\tau)q_i^{n-1}}{(\Delta t^n)^2} = \frac{\tau/(1+\tau)\Delta q_i^n - \tau^2/(1+\tau)\Delta q_i^{n-1}}{(\Delta t^n)^2/2} \\
\left. \frac{\partial^2(q_i)}{\partial t^2} \right|^n &= \frac{(c)(\Delta q_i^n) - (b)(\Delta q_i^{n-1})}{(\Delta t^n)^2/2}
\end{aligned} \tag{3.17}$$

in which

$$\tau = \Delta t^n / \Delta t^{n-1} \tag{3.18}$$

$$a = (1+2\tau)/(1+\tau) \tag{3.19}$$

$$b = \tau^2/(1+\tau) \tag{3.20}$$

$$c = \tau/(1+\tau) \tag{3.21}$$

Equation (3.16) has been used for the left hand side of Eq. (3.14). Finally Eq. (3.14) becomes in the form of:

$$\left[a \frac{\text{Vol}(C_i)}{\Delta t^n} - (a+c) \sum_j \left(\frac{\partial K(q_i^n, q_j^n)}{\partial q_i} \right) \right] \Delta q_i^n - (a+c) \sum_j \left(\frac{\partial K(q_i^n, q_j^n)}{\partial q_j} \right) \Delta q_j^n =$$

$$\sum_j K(q_i^n, q_j^n) - (2b) \sum_j \left(\frac{\partial K(q_i^n, q_j^n)}{\partial q_i} \right) \Delta q_i^{n-1} + \frac{\partial K(q_i^n, q_j^n)}{\partial q_j} \Delta q_j^{n-1} + b \frac{\text{Vol}(C_i)}{\Delta t^n} \Delta q_i^{n-1} + O((\Delta t)^2) \quad (3.22)$$

Equations similar to Eq. (3.22) are then considered for every cell inside the domain and then the system of equations is solved, using an iterative GMRES solver.

3.4 Boundary Conditions

By neglecting the viscous terms in the Eq. (2.17), we obtain the Euler equations:

$$\frac{\partial q}{\partial t} + \text{div}(\bar{F}^{\text{conv}}(q)) = \frac{\partial q}{\partial t} + \bar{\nabla} \cdot (\bar{F}^{\text{conv}}(q)) = \frac{\partial q}{\partial t} + \left(\frac{\partial \bar{F}^{\text{conv}}(q)}{\partial q} \right) \cdot \bar{\nabla} q = \frac{\partial q}{\partial t} + \sum_{i=1}^3 \left(\frac{\partial F_i^{\text{conv}}(q)}{\partial q} \right) \times \frac{\partial q}{\partial x_i} = 0 \quad (3.23)$$

We can drive the quasi-linear form of the Euler equations as follows:

$$\frac{\partial q}{\partial t} + \sum_{i=1}^3 \left(\frac{\partial F_i^{\text{conv}}(q)}{\partial q} \right) \times \frac{\partial q}{\partial x_i} = \frac{\partial q}{\partial t} + \sum_{i=1}^3 (A_i \times \frac{\partial q}{\partial x_i}) = \frac{\partial q}{\partial t} + \bar{A} \cdot \bar{\nabla} q = 0 \quad (3.24)$$

in which $A_i = \frac{\partial F_i^{\text{conv}}(q)}{\partial q}$ and they are defined for the real gases as:

$$A_i = \begin{pmatrix} 0 & 1 & 0 & 0 & 0 \\ -u_1^2 + \frac{\gamma-1}{2} |\bar{u}|^2 & (3-\gamma)u_1 & -(\gamma-1)u_2 & -(\gamma-1)u_3 & \gamma-1 \\ -u_1 u_2 & u_2 & u_1 & 0 & 0 \\ -u_1 u_3 & u_3 & 0 & u_1 & 0 \\ -u_1(\gamma - (\gamma-1)|\bar{u}|^2) & \gamma - \frac{\gamma-1}{2} (|\bar{u}|^2 + 2u_1^2) & -(\gamma-1)u_1 u_2 & -(\gamma-1)u_1 u_3 & \gamma u_1 \end{pmatrix} \quad (3.25)$$

$$A_2 = \begin{pmatrix} 0 & 0 & 1 & 0 & 0 \\ -u_1 u_2 & u_2 & u_1 & 0 & 0 \\ -u_2^2 + \frac{\gamma-1}{2} |\bar{u}|^2 & -(\gamma-1)u_1 & (3-\gamma)u_2 & -(\gamma-1)u_3 & \gamma-1 \\ -u_2 u_3 & 0 & u_3 & u_2 & 0 \\ -u_2(\gamma e - (\gamma-1)|\bar{u}|^2) & -(\gamma-1)u_1 u_2 & \gamma e - \frac{\gamma-1}{2} (|\bar{u}|^2 + 2u_2^2) & -(\gamma-1)u_2 u_3 & \gamma u_2 \end{pmatrix} \quad (3.26)$$

$$A_3 = \begin{pmatrix} 0 & 0 & 0 & 1 & 0 \\ -u_1 u_3 & u_3 & 0 & u_1 & 0 \\ -u_2 u_3 & 0 & u_3 & u_2 & 0 \\ -u_3^2 + \frac{\gamma-1}{2} |\bar{u}|^2 & -(\gamma-1)u_1 & -(\gamma-1)u_2 & (3-\gamma)u_3 & \gamma-1 \\ -u_3(\gamma e - (\gamma-1)|\bar{u}|^2) & -(\gamma-1)u_1 u_3 & -(\gamma-1)u_2 u_3 & \gamma e - \frac{\gamma-1}{2} (|\bar{u}|^2 + 2u_3^2) & \gamma u_3 \end{pmatrix} \quad (3.27)$$

The Jacobian matrix for the convective fluxes passing through a surface with the normal vector $\bar{n} = (n_1, n_2, n_3)$ is defined as:

$$\bar{A} \bullet \bar{n} = A_1 n_1 + A_2 n_2 + A_3 n_3 \quad (3.28)$$

In order to change the vector of conservative variables (q) to the primitive variables (V), the appropriate transformation matrix is needed to be multiplied into the Eq. (3.24):

$$M \frac{\partial q}{\partial t} + M(\bar{A})(M^{-1}M) \cdot \bar{\nabla} q = \frac{M \partial q}{\partial t} + (M\bar{A}M^{-1}) \cdot M\bar{\nabla} q = 0$$

$$\frac{\partial V}{\partial t} + (M\bar{A}M^{-1}) \cdot \bar{\nabla} V = \frac{\partial V}{\partial t} + (\bar{A}^p) \cdot \bar{\nabla} V = 0 \quad (3.29)$$

in which $A_i^p = M A_i M^{-1}$ and:

$$V = \begin{pmatrix} \rho \\ u_1 \\ u_2 \\ u_3 \\ p \end{pmatrix} \quad (3.30) \quad M = \frac{\partial V}{\partial q} = \begin{pmatrix} 1 & 0 & 0 & 0 & 0 \\ -u_1/\rho & 1/\rho & 0 & 0 & 0 \\ -u_2/\rho & 0 & 1/\rho & 0 & 0 \\ -u_3/\rho & 0 & 0 & 1/\rho & 0 \\ \frac{1}{2}(\gamma-1)|\bar{u}|^2 & -(\gamma-1)u_1 & -(\gamma-1)u_2 & -(\gamma-1)u_3 & \gamma-1 \end{pmatrix} \quad (3.31)$$

A_i^p are defines as follow:

$$A_1^p = \begin{pmatrix} u_1 & 0 & 0 & 0 & 0 \\ 0 & u_1 & 0 & 0 & \frac{1}{\rho} \\ 0 & 0 & u_1 & 0 & 0 \\ 0 & 0 & 0 & u_1 & 0 \\ 0 & \rho c^2 & 0 & 0 & u_1 \end{pmatrix} \quad (3.32)$$

$$A_2^p = \begin{pmatrix} u_2 & 0 & 0 & 0 & 0 \\ 0 & u_2 & 0 & 0 & 0 \\ 0 & 0 & u_2 & 0 & \frac{1}{\rho} \\ 0 & 0 & 0 & u_2 & 0 \\ 0 & 0 & \rho c^2 & 0 & u_2 \end{pmatrix} \quad (3.33)$$

$$A_3^p = \begin{pmatrix} u_3 & 0 & 0 & 0 & 0 \\ 0 & u_3 & 0 & 0 & 0 \\ 0 & 0 & u_3 & 0 & 0 \\ 0 & 0 & 0 & u_3 & \frac{1}{\rho} \\ 0 & 0 & 0 & \rho c^2 & u_3 \end{pmatrix} \quad (3.34)$$

The Jacobian matrix for the primitive fluxes passing through a surface with the normal vector $\bar{n} = (n_1, n_2, n_3)$ is defined as:

$$\bar{A}^p \cdot \bar{n} = A_1^p n_1 + A_2^p n_2 + A_3^p n_3 \quad (3.35)$$

in the Eqs. (3.32-3.34), it is assumed that $n_1^2 + n_2^2 + n_3^2 = 1$ and $c = \sqrt{\gamma RT}$.

Matrix $\bar{A}^p \cdot \bar{n}$ can be diagonalized using its matrix of eigenvectors. Eigenvectors can be obtained by solving the eigenvalue problem:

$$|\bar{A}^p \cdot \bar{n} - \lambda I| = (\bar{u} \cdot \bar{n} - \lambda)^3 ((\bar{u} \cdot \bar{n} - \lambda)^2 - c^2) = 0 \quad (3.36)$$

The solutions of the Eq. (3.36) are the eigenvalues of matrix $\bar{A}^p \cdot \bar{n}$ and $\bar{A} \cdot \bar{n}$. They are as follows:

$$\begin{aligned} \lambda_1 &= \lambda_2 = \lambda_3 = \bar{u} \cdot \bar{n} \\ \lambda_4 &= \bar{u} \cdot \bar{n} + c \\ \lambda_5 &= \bar{u} \cdot \bar{n} - c \end{aligned} \quad (3.37)$$

By using every calculated eigenvalue, we can calculate the corresponding left eigenvectors. Those eigenvectors can be placed as the rows of a matrix. This matrix will be a diagonalization matrix for

$\bar{A}^P \bullet \bar{n}$:

$$L = \begin{pmatrix} n_1 & 0 & \frac{\rho}{c} n_3 & -\frac{\rho}{c} n_2 & -\frac{n_1}{c^2} \\ n_2 & -\frac{\rho}{c} n_3 & 0 & \frac{\rho}{c} n_1 & -\frac{n_2}{c^2} \\ n_3 & \frac{\rho}{c} n_2 & -\frac{\rho}{c} n_1 & 0 & -\frac{n_3}{c^2} \\ 0 & \frac{\rho}{2c} n_1 & \frac{\rho}{2c} n_2 & \frac{\rho}{2c} n_3 & \frac{1}{2c^2} \\ 0 & -\frac{\rho}{2c} n_1 & -\frac{\rho}{2c} n_2 & -\frac{\rho}{2c} n_3 & \frac{1}{2c^2} \end{pmatrix} \quad (3.38)$$

$$\Lambda = L(\bar{A}^P \bullet \bar{n})L^{-1} = \begin{pmatrix} \bar{u} \cdot \bar{n} & 0 & 0 & 0 & 0 \\ 0 & \bar{u} \cdot \bar{n} & 0 & 0 & 0 \\ 0 & 0 & \bar{u} \cdot \bar{n} & 0 & 0 \\ 0 & 0 & 0 & \bar{u} \cdot \bar{n} + c & 0 \\ 0 & 0 & 0 & 0 & \bar{u} \cdot \bar{n} - c \end{pmatrix} \quad (3.39)$$

When this matrix is multiplied into the primitive vector, the finite variation of characteristic vector is obtained:

$$\Delta w = \begin{pmatrix} \Delta w_1 \\ \Delta w_2 \\ \Delta w_3 \\ \Delta w_4 \\ \Delta w_5 \end{pmatrix} = L \Delta V = \begin{pmatrix} n_1 & 0 & \frac{\rho}{c} n_3 & -\frac{\rho}{c} n_2 & -\frac{n_1}{c^2} \\ n_2 & -\frac{\rho}{c} n_3 & 0 & \frac{\rho}{c} n_1 & -\frac{n_2}{c^2} \\ n_3 & \frac{\rho}{c} n_2 & -\frac{\rho}{c} n_1 & 0 & -\frac{n_3}{c^2} \\ 0 & \frac{\rho}{2c} n_1 & \frac{\rho}{2c} n_2 & \frac{\rho}{2c} n_3 & \frac{1}{2c^2} \\ 0 & -\frac{\rho}{2c} n_1 & -\frac{\rho}{2c} n_2 & -\frac{\rho}{2c} n_3 & \frac{1}{2c^2} \end{pmatrix} \begin{pmatrix} \Delta \rho \\ \Delta u_1 \\ \Delta u_2 \\ \Delta u_3 \\ \Delta p \end{pmatrix} \quad (3.40)$$

$$\Delta w = \begin{pmatrix} \Delta w_1 \\ \Delta w_2 \\ \Delta w_3 \\ \Delta w_4 \\ \Delta w_5 \end{pmatrix} = \begin{pmatrix} n_1 \Delta \rho + \frac{\rho}{c} (n_3 \Delta u_2 - n_2 \Delta u_3) - \frac{1}{c^2} n_1 \Delta p \\ n_2 \Delta \rho + \frac{\rho}{c} (n_1 \Delta u_3 - n_3 \Delta u_1) - \frac{1}{c^2} n_2 \Delta p \\ n_3 \Delta \rho + \frac{\rho}{c} (n_2 \Delta u_1 - n_1 \Delta u_2) - \frac{1}{c^2} n_3 \Delta p \\ \frac{1}{2} \left(\frac{1}{c^2} \Delta p + \frac{\rho}{c} \Delta \bar{u} \cdot \bar{n} \right) \\ \frac{1}{2} \left(\frac{1}{c^2} \Delta p - \frac{\rho}{c} \Delta \bar{u} \cdot \bar{n} \right) \end{pmatrix} \quad (3.41)$$

It can be shown that information inside the flow is transferred by five independent characteristic waves at every location. Every wave travels along its corresponding eigenvector and transfers the characteristic variable with a speed equal to the corresponding eigenvalue. This hyperbolic nature of the flow equations is very important and it is used to define different boundary conditions.

3.4.1 Subsonic Inlet Boundary Condition

At subsonic inlet boundary condition, only the first four characteristic waves are entering into the computational domain while the fifth wave is moving in the opposite direction of the flow and therefore it is traveling from inside toward the exterior of the domain. In this case, the density and the velocity vector are fixed while the pressure is interpolated from the inside of the domain. According to the characteristic method it will be more accurate if the variables are set in such a way that the first four finite variation of the characteristic variables become zero (Eq. (3.41)). Nevertheless it has been shown in the literature that fixing the characteristic variables is satisfactory and will generate acceptable results.

In LES when the level of turbulence intensity at inlet is known or can be reasonably estimated, a fluctuating term is superimposed over the average profile:

$$\bar{U}(\bar{x}, t) = \bar{U}_0(\bar{x}) + \bar{U}'(\bar{x}, t) \quad (3.42)$$

In our research however, as it will be shown in the next chapters, no artificial turbulence forcing at the inlet boundary conditions is used.

3.4.2 Noslip Adiabatic Boundary Condition

For this type of boundary condition, all the velocity components are set to zero but the pressure is extrapolated from inside the domain. Considering that in this case, three of the characteristic values are zero and therefore just one characteristic wave is entering from the boundary inside the domain, only one variable is needed to be set at the boundary. The value of that parameter is set by the adiabatic condition:

$$\bar{\nabla} T \cdot \bar{n} = 0 \quad (3.43)$$

3.4.3 Free Slip Boundary Condition

When this boundary condition is applied on a surface from the boundary, the velocity normal to the surface is set to zero while the components parallel to the surface are not adjusted. Therefore the convective flux normal to the boundary will reduce only to:

$$\bar{F}^{conv} \cdot \bar{n} = \begin{Bmatrix} \rho \bar{u} \cdot \bar{n} \\ \rho \bar{u} \cdot \bar{n} u_1 + p n_1 \\ \rho \bar{u} \cdot \bar{n} u_2 + p n_2 \\ \rho \bar{u} \cdot \bar{n} u_3 + p n_3 \\ \bar{u} \cdot \bar{n} (\rho e + p) \end{Bmatrix} = \begin{Bmatrix} 0 \\ p n_1 \\ p n_2 \\ p n_3 \\ 0 \end{Bmatrix} \quad (3.44)$$

No control volume exists outside the boundary of the domain; therefore the fluxes at the boundary have to be evaluated using the variables of corresponding boundary nodes.

3.4.4 Nonreflective Boundary Condition

As it is shown in Fig. 3.5, the convective flux at a boundary node has two components: the first one is the contribution of the node located on the boundary ($\bar{F}^{conv}(q_I) \cdot \bar{n}$) and the second one is the contribution of an imaginary (virtual) node outside of the computational domain ($\bar{F}^{conv}(q_J) \cdot \bar{n}$).

$$\bar{F}_b^{conv} \cdot \bar{n} = \bar{F}^{conv}(q_I) \cdot \bar{n} + \bar{F}^{conv}(q_J) \cdot \bar{n} \quad (3.45)$$

In the case of nonreflective boundary condition, the characteristic waves constituting these components are modified in order to provide the desirable non reflective characteristic. During the calculation of the flux coming from the domain, all the characteristics waves that are towards the interior domain are removed. On the contrary, when the virtual node's contribution is calculated, only the characteristic waves that move towards the domain are considered and the ones which move away from the boundary are not considered. This procedure will prohibit the reflection of flow's characteristics as it is leaving the computational domain and doesn't permit the shock waves to reflect back inside the domain to contaminate the solution.

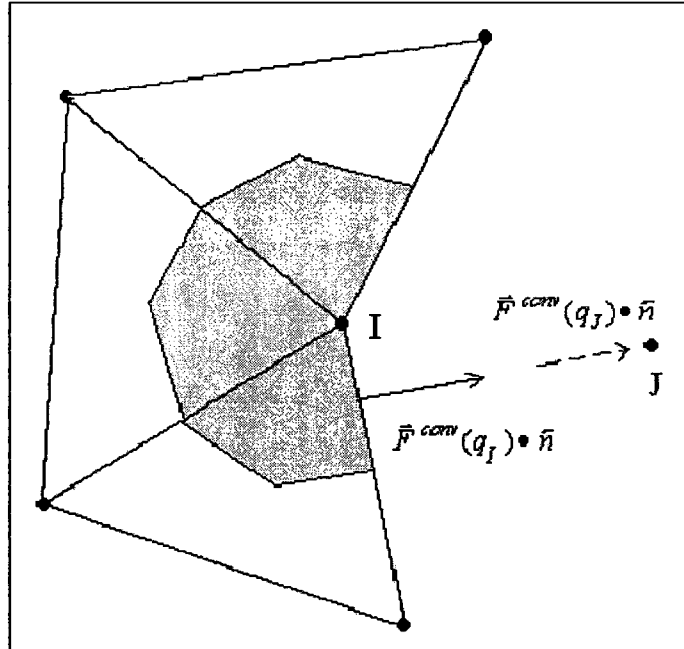


Fig. 3.5 Flux calculation for the nonreflective boundary condition.

3.4.5 Pressure Output Boundary Condition

This boundary condition is imposed based on the same principal as the nonreflective boundary condition. The only difference is that in order to calculate the flux contributed by the virtual nodes (flux from node J as it is shown in Fig. 3.5) a predetermined pressure distribution is considered.

3.4.6 Periodic Boundary Condition

For this boundary condition, we assume that the certain nodes located on the boundaries at different sides of the computational domain are attached (nodes I and J in Fig. 3.6). As a result all the edges connected to one periodic node (for instance the edge connecting the node K to I) makes the necessary contribution to the balance of fluxes of the other node (in this case J) which is presumably attached to it according to the periodic boundary condition. The necessary contribution includes both the viscous and convective fluxes.

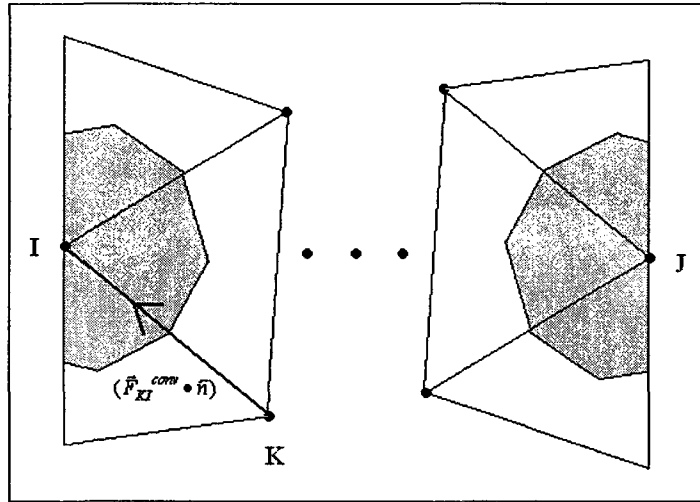


Fig. 3.6 Nodes I and J attached according to the periodic boundary condition.

Chapter 4

Numerical Verifications

IN this chapter at first, a channel flow simulation is carried out to test the stability of the applied numerical method, explained in chapter 3, against strong gradients and fluctuations in the flow and to measure its ability to adjust itself under such circumstances and converge. Then, decaying isotropic turbulence is simulated and the influence of the self-adaptive upwinding scheme over the total kinetic energy and the energy spectrum is studied. Its interaction with the Smagorinsky SGS is also investigated. These test cases serve as validation and calibration steps for the scheme's development.

4.1 Channel Flow Stability Simulation

In the Channel flow test, the stability characteristics of the numerical method against strong gradients and fluctuations, artificially generated by a noise term in the flow initialization, are investigated. It is expected that the computed velocities result in a bounded total kinetic energy. If the scheme fails to satisfy this condition, it can be concluded with certainty that the numerical method is not suited to model turbulent flows. On the other hand, if it fulfills this condition, it does not mean automatically that it is a good model.

In this test, the flow through a channel presented in Fig. 4.1 is simulated. A similar test has been presented for an incompressible fluid simulation in Ref. 94, using hexahedral and tetrahedral elements. In the simulation presented here only tetrahedral elements are used. The discretized domain contains 2302 tetrahedrons, 9658 nodes and 2532 boundary faces. A rather coarse mesh is used in this simulation to reflect the typical situation in the LES of turbulent flows in which there are too few degrees of freedom available for the simulated Reynolds number. The time step (Δt) of the simulation is set to 0.01 as it is the

case in Ref. 94. At each time step, the residual is decreased 6 degrees in order to provide good accuracy.

The inflow boundary condition is defined as:

$$\bar{U}(t,0, y, z) = \begin{pmatrix} 4y(1-y) \\ 0 \\ 0 \end{pmatrix} \quad (4.1)$$

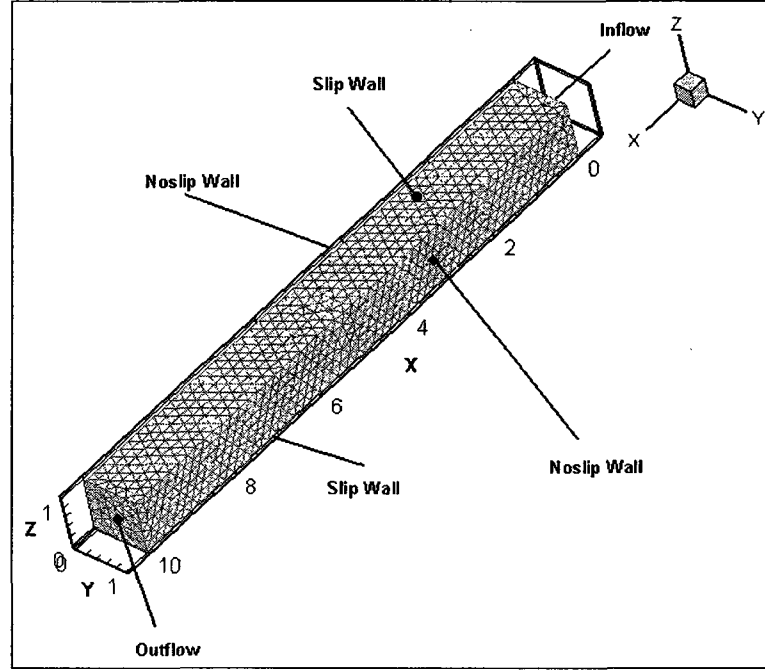


Fig. 4.1 Channel flow's grid and boundary conditions.

On the lateral walls, the noslip boundary condition is imposed and on the top and bottom walls, the free slip boundary condition is applied (Fig. 4.1). The flow leaves the channel at the outflow boundary condition where pressure is fixed over that face. The initial velocity is given by:

$$\bar{U}(0, \bar{X}) = \begin{pmatrix} 4y(1-y) \\ 0 \\ 0 \end{pmatrix} + C_{noise} \begin{pmatrix} -4\pi \sin(4\pi y) \\ -3\pi \sin(3\pi z) \\ 3\pi \cos(3\pi x) \end{pmatrix} \quad (4.2)$$

Without presence of any noise in the initial condition ($C_{noise} = 0.0$)

$$\bar{U}(t, x, y, z) = \begin{pmatrix} 4y(1-y) \\ 0 \\ 0 \end{pmatrix} \quad (4.3)$$

$$P(t, x, y, z) = -8\nu(x-10) + P_0 \quad (4.4)$$

is a solution of the Navier-Stokes equations. Inside the channel, the flow's total kinetic energy (steady condition) is estimated to be 2.666. This is done by integrating the velocity distribution given by Eq. (4.3) over the entire nondimensionalized domain. The nondimensional molecular viscosity is assumed to be $\nu = 10^{-5}$ and the Reynolds number of the flow, based on the average inflow and height of the channel (L) is:

$$\text{Re} = \frac{\overline{UL}}{\nu} = \frac{2}{3} 10^5 = 66667 \quad (4.5)$$

In this simulation the Mach number is set to the value of 0.01 in order to keep the flow regime close to incompressible. The computational domain's total kinetic energy is computed by:

$$E(t) = \sum_{n=1}^N \left(\frac{3}{2} \sum_{i=1}^3 u_i^2(n) \times \text{Vol}(C_n) \right) \quad (4.6)$$

where N is defined as total number of nodes inside the domain and $\text{Vol}(C_n)$ is the volume of cell C_n , which belongs to node n .

In the channel flow simulation, γ is assumed to be chosen within an interval of which the limits are set separately and fixed for every simulation falling within $[0,1]$. This makes it possible to adjust the average effect of upwinding in every test case. To test the stability of the self-adaptive scheme, the permitted intensity of the local wiggles (θ) is set to zero, in order to completely damp the local wiggles. Considering that the grid resolution is very low and θ has been set to zero, we expect a laminar solution (Eqs. (4.3,4.4)), even though the Reynolds number is relatively high.

The different computations, as summarized in Table 4.1, are performed in order to evaluate the stability of the scheme against the strong fluctuations that might be present in every typical LES. When full upwinding (case 1) is considered, the total kinetic energy of the system is somewhat lower than the expected value of 2.666. Recall that the flow is not well resolved by the mesh and therefore Eq. (4.6) is an approximation for the integration operation used to calculate the estimated total kinetic energy of the numerical domain.

Table 4.1 Explanation of different cases for the channel flow simulation.

Case #	Upwinding Parameters			C_{noise}	C_S	E(t)	
	Upper value of γ	Lower value of γ	θ			t = 0	t = 10
1	1.0	1.0	0.0	0.0	0.0	2.6617	2.3296
2	1.0	0.43	0.0	0.0	0.0	2.6617	2.6508
3	1.0	0.1	0.0	0.0	0.0	2.6617	2.9446
4	1.0	0.0	0.0	0.0	0.0	2.6617	3.0023
5	1.0	0.43	0.0	0.01	0.0	2.73813	2.6510
6	1.0	0.43	0.0	0.1	0.0	10.2229	2.6738

In cases 2, 3, and 4, the upwinding parameter's lower limit is decreased (Table 4.1) and it reduces the average upwinding coefficient respectively. By decreasing γ the flux calculation scheme becomes more central which makes the simulation more unstable and therefore the wiggles gradually start to appear inside the domain. The self-adaptive scheme tries to locally adjust γ in order to damp those wiggles and as a result the simulation remains stable. However, as it is illustrated in Fig. 4.2, a gradual increase in the total kinetic energy is observed. In case 4 the effects of those random wiggles appear even further and the total kinetic energy is showing chaotic fluctuations. That is an indication of a fairly unstable flow regime inside the channel even though the total kinetic energy has still remained bounded. In case 2, the total kinetic energy becomes very close to 2.666 and for the next part of this test, the lower limit of upwinding term is kept equal to 0.43.

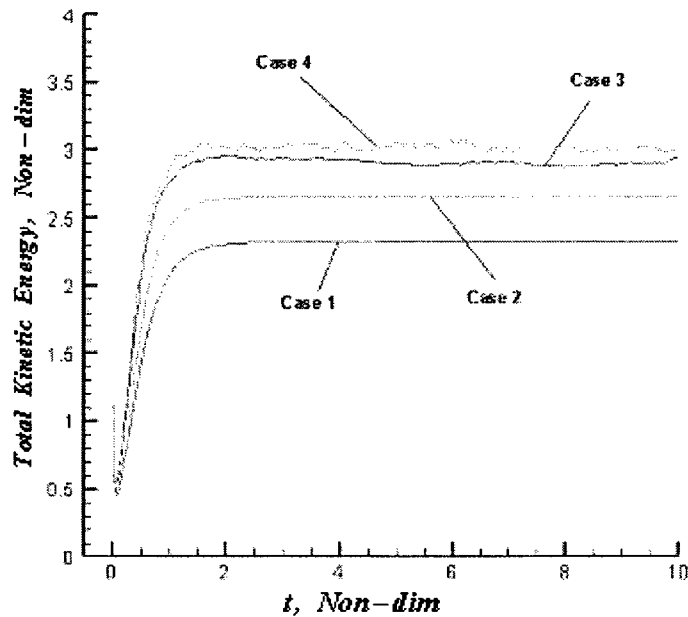


Fig. 4.2 Channel flow simulation (Cases 1, 2, 3, 4).

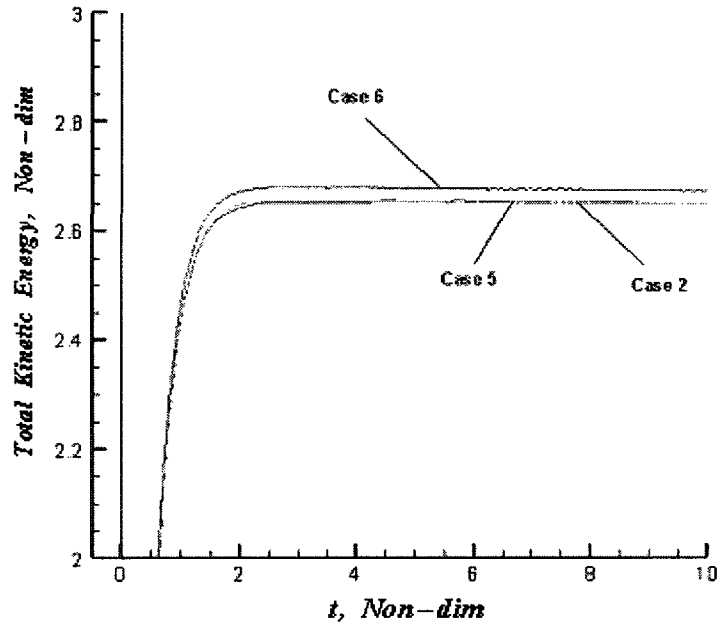


Fig. 4.3 Channel flow simulation (Cases 2, 5, 6).

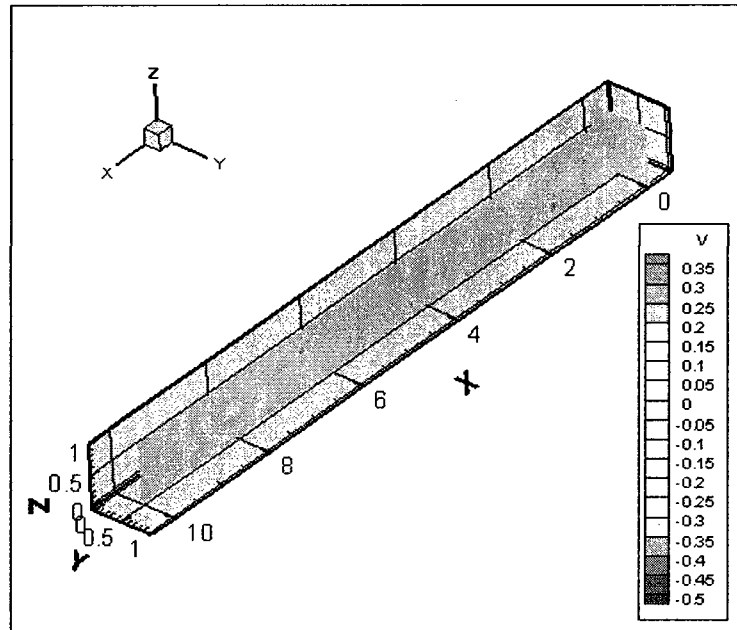


Fig. 4.4 Non-dim. y-velocity (Case 4).

In Fig. 4.3 the effect of noise is investigated using cases 2,5 and 6. As it is seen in this graph, the self-adaptive upwinding method is showing a very good stability characteristic despite the fact that the value of 0.1 for noise coefficient is ten times higher than the value used in Ref. 94.

4.2 Decaying Isotropic Turbulence

The simplest kind of turbulence is isotropic and therefore isotropic turbulence forms a natural starting point for the study and simulation of turbulence. This flow has been considered in many earlier and recent investigations.^{62,77,78,80,95,96} The experiment for the decay of isotropic turbulence by Comte-Bellot and Corrsin (CBC in 1971)⁹⁷ is used to validate our simulation. In that experiment, turbulence was generated using a biplane, square rod grid with mesh size $M = 5.08\text{cm}$ which was placed inside a flow with a uniform upstream velocity of $U_0 = 10\text{m/s}$ (Fig. 4.5). The upstream, hot-wire probe was placed at $U_0 t_{CBC} / M = 42 \pm 2$ downstream of the grid and approximately on the centerline of the wind tunnel. The downstream probe was mounted on a sliding carriage for large motions in the stream direction. The Reynolds number based on the grid spacing is $Re_M = U_0 M / \nu = 34000$.

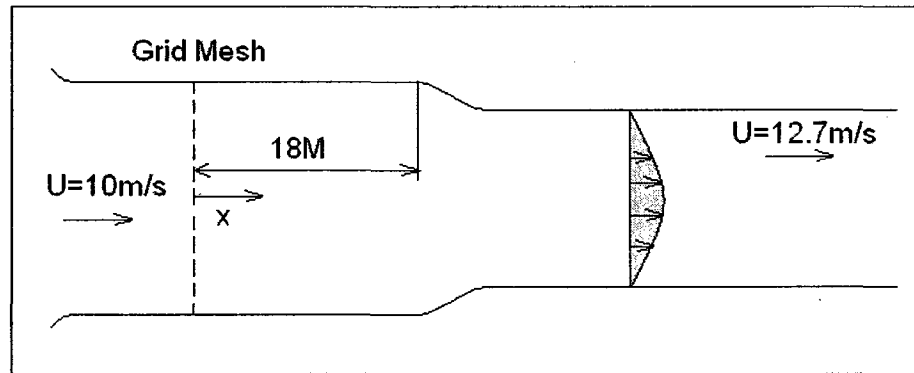


Fig. 4.5 Comte-Bellot and Corrsin's experimental setup.

Different quantities, including the energy spectrum at three consecutive stations ($U_0 t_{CBC} / M = 42, 98$ and 171) were measured. The dimensional time in the experiment (t_{CBC}) is defined as:

$$t_{CBC} = \int_0^x \frac{dx}{U(x)} \quad (4.7)$$

in which x is the downstream distance from the grid and $U(x)$ is the mean velocity. Because the same flow passes through all the stations we can use the measured data to verify the validity of the numerical results at three different computational times.

The simulation is carried out inside a box with a size larger than the integral length scale and much smaller than the wind tunnel's cross section. 32768 nodes and 178746 tetrahedrons are used in this model. Each edge of the box has been divided by 32 nodes into segments of equal size and then all elements are distributed uniformly inside the domain. Periodic boundary condition is imposed on all sides of the box.

In Ref. 97 one-dimensional energy spectrum E_{11} at $U_0 t_{CBC} / M = 42$ is reported which can be approximated by a logarithmic polynomial as bellow: ^{64,95}

$$\log_e E_{11}(k) = A_0 + A_1 \log_e k + A_2 (\log_e k)^2 + A_3 (\log_e k)^3 + A_4 (\log_e k)^4 \quad (4.8)$$

In the isotropic turbulence, the energy spectrum $E(k)$ can be obtained from $E_{11}(k)$ by:

$$E(k) = \frac{1}{2} k^3 \frac{\partial}{\partial k} \left(\frac{1}{k} \frac{\partial E_{11}}{\partial k} \right) \quad (4.9)$$

This yields to:

$$E(k) = E_{11} \left\{ \frac{1}{2} [A_1 + 2A_2 \log_e k + 3A_3 (\log_e k)^2 + 4A_4 (\log_e k)^3]^2 + A_2 - A_1 + (3A_3 - 2A_2) \log_e k + (6A_4 - 3A_3) (\log_e k)^2 - 4A_4 (\log_e k)^3 \right\} \quad (4.10)$$

in which coefficients are reported in Table 4.2.

The initial velocity field for the simulation is created by superimposing Fourier modes having prescribed energy spectrum as Eq. (4.10) but random phases. The method has been completely described in Ref. 64 and 95 and it is briefly described here.

Table 4.2 Coefficients used to define energy spectrum at $U_0 t_{CBC} / M = 42$.

Coefficient	Value
A_0	4.7935398
A_1	-1.3284141
A_2	-0.2146974
A_3	-0.0314604
A_4	-0.0169870

A zero-mean, dimensionless, periodic and random velocity field, which was initially achieved by filtering the LES results of another simulation is considered. This distribution can be expressed by a discrete Fourier series as follows:

$$\bar{u}(\bar{x}) = \sum_{-N_x+1}^{N_x} \sum_{-N_y+1}^{N_y} \sum_{-N_z+1}^{N_z} \hat{u}(l, m, n) e^{i\bar{k} \cdot \bar{x}} \quad (4.11)$$

where the triple sum is over l, m and n, respectively, and

$$\bar{k} = k_l \bar{i} + k_m \bar{j} + k_n \bar{k} \quad (4.12)$$

$$\bar{x} = x\bar{i} + y\bar{j} + z\bar{k} \quad (4.13)$$

The dimensionless wave numbers are defined as:

$$k_l = l \quad (4.14)$$

$$k_m = m \quad (4.15)$$

$$k_n = n \quad (4.16)$$

and

$$N_x = N_y = N_z = N/2 \quad (4.17)$$

where N=32 in accordance with the applied grid. This initial velocity distribution has the following definition in the physical space:

$$\bar{u}(\bar{x}) = u(\bar{x})\bar{i} + v(\bar{x})\bar{j} + w(\bar{x})\bar{k} \quad (4.18)$$

and in Fourier space it is defined as:

$$\hat{\bar{u}}(l, m, n) = \hat{u}(l, m, n)\bar{i} + \hat{v}(l, m, n)\bar{j} + \hat{w}(l, m, n)\bar{k} \quad (4.19)$$

The mentioned Fourier transform of the initial velocity field is modified to achieve zero divergence by the following replacement:

$$\hat{u}(l, m, n) \leftarrow \hat{u}(l, m, n) - \frac{k_l}{k^2} \Delta \quad (4.20)$$

$$\hat{v}(l, m, n) \leftarrow \hat{v}(l, m, n) - \frac{k_m}{k^2} \Delta \quad (4.21)$$

$$\hat{w}(l, m, n) \leftarrow \hat{w}(l, m, n) - \frac{k_n}{k^2} \Delta \quad (4.22)$$

where

$$k^2 = k_l^2 + k_m^2 + k_n^2 \quad (4.23)$$

$$\Delta = \bar{k} \bar{\tilde{u}}(l, m, n) \quad (4.24)$$

The Fourier coefficients need to be further modified in order to agree with the initial energy spectrum of CBC. The local dimensionless turbulence kinetic energy can be written as:

$$E_{kin} = \frac{1}{(2\pi)^3} \int_0^{2\pi} \int_0^{2\pi} \int_0^{2\pi} \frac{1}{2} u_i u_i dx dy dz \quad (4.25)$$

By applying the Parseval's relation we obtain:

$$E_{kin} = \sum_{-N_x+1}^{N_x-1} \sum_{-N_y+1}^{N_y-1} \sum_{-N_z+1}^{N_z-1} \frac{1}{2} (\hat{u}\hat{u}^* + \hat{v}\hat{v}^* + \hat{w}\hat{w}^*) \quad (4.26)$$

where $\hat{u}(l, m, n)^*$ is the complex conjugate of $\hat{u}(l, m, n)$. The initial turbulent kinetic energy can also be derived from the energy spectra $E(k)$:

$$E_{kin} = \int_0^\infty E(k) dk \quad (4.27)$$

where $E(k)$ has been non-dimensionalized by $U_\infty^2 L_\infty$, and k by L_∞^{-1} . The filtered turbulence kinetic energy is

$$E_{kin}|_{filtered} = \int_{k_0}^{k_{N_k}} E(k) dk \quad (4.28)$$

where the range of the integral is divided into N_k equal increments. k_0 and k_{N_k} represent the smallest and largest wave numbers in the simulation,

$$k_0 = 1 \quad (4.29)$$

$$k_{N_k} = \frac{\sqrt{3}}{2}(N-2) \quad (4.30)$$

From Eq. (4.26) and Eq. (4.28)

$$\int_{k_0}^{k_{N_k}} E(k) dk = \sum_{-N_x+1}^{N_x-1} \sum_{-N_y+1}^{N_y-1} \sum_{-N_z+1}^{N_z-1} \frac{1}{2} (\hat{u}\hat{u}^* + \hat{v}\hat{v}^* + \hat{w}\hat{w}^*) \quad (4.31)$$

and using the trapezoidal rule

$$\sum_{i=1}^{N_k} \frac{1}{2} [E(k_i) + E(k_{i-1})] \Delta k = \sum_{-N_x+1}^{N_x-1} \sum_{-N_y+1}^{N_y-1} \sum_{-N_z+1}^{N_z-1} \frac{1}{2} (\hat{u}\hat{u}^* + \hat{v}\hat{v}^* + \hat{w}\hat{w}^*) \quad (4.32)$$

where

$$\Delta k = \frac{k_{N_k} - k_0}{N_k} \quad (4.33)$$

Equation (4.32) is satisfied if:

$$\frac{\Delta k}{2} [E(k_i) + E(k_{i-1})] = \sum_{l,m,n} \frac{1}{2} (\hat{u}\hat{u}^* + \hat{v}\hat{v}^* + \hat{w}\hat{w}^*) \quad (4.34)$$

for $i = 1, \dots, N_k$. The summation is over all modes (l,m,n) in such a way that the affiliated wave number is within a shell which is defined as:

$$\underbrace{1 + (i-1)\Delta k}_{k_{i-1}} \leq k \leq \underbrace{1 + i\Delta k}_{k_i} \quad (4.35)$$

where the dimensionless wave number is $k = \sqrt{l^2 + m^2 + n^2}$. This is accomplished by rescaling the Fourier coefficients according to

$$\hat{u}(l, m, n) \leftarrow \Psi \bullet \hat{u}(l, m, n) \quad (4.36)$$

$$\hat{v}(l, m, n) \leftarrow \Psi \bullet \hat{v}(l, m, n) \quad (4.37)$$

$$\hat{w}(l, m, n) \leftarrow \Psi \bullet \hat{w}(l, m, n) \quad (4.38)$$

$$\Psi = \sqrt{\frac{[E(k_i) + E(k_{i-1})]\Delta k}{\sum_{l,m,n} [\hat{u}\hat{u}^* + \hat{v}\hat{v}^* + \hat{w}\hat{w}^*]}} \quad (4.39)$$

The discrete Fourier series given by Eq. (4.11) in which \hat{u}, \hat{v} and \hat{w} have to be calculated from Eqs. (4.36-4.38) will construct the required initial velocity distribution. In addition, the initial pressure distribution is obtained from the incompressible Poisson equation using the initial velocity field. The result is shown in Fig. 4.6.

A slight difference exists between $E(k)$ reported by CBC data (Ref. 97) and the applied initialization for $E(k)$. It is necessary to mention that during the CBC experiment, one-dimensional energy spectrums ($E_{11}(k)$) were measured at three different locations and then the affiliated energy spectrums ($E(k)$) were calculated using “graphical differentiation of faired curves”. It seems that using polynomial curve fitting, which is implemented here, is more accurate than CBC method. That is however the case only for $U_0 t_{CBC} / M = 42$. Our attempts to use the polynomial procedure to extract $E(k)$ from $E_{11}(k)$ for $U_0 t_{CBC} / M = 98$ and $U_0 t_{CBC} / M = 171$ did not achieve any better result in comparison to CBC. Therefore, we decided to initialize the simulation using $E(k)$ from Eq. (4.10) whereas for comparing the simulated energy spectrum at $U_0 t_{CBC} / M = 98$ and 171 with experiment, the curves provided by CBC are used.

As mentioned earlier, the decaying turbulence is simulated by considering the fluid to be inside a cube. Each side of this cube has the length of L_C which is assumed to be equal to 43.787cm. This length represents the zero-intercept of $E(k)$ in Eq. (4.10).

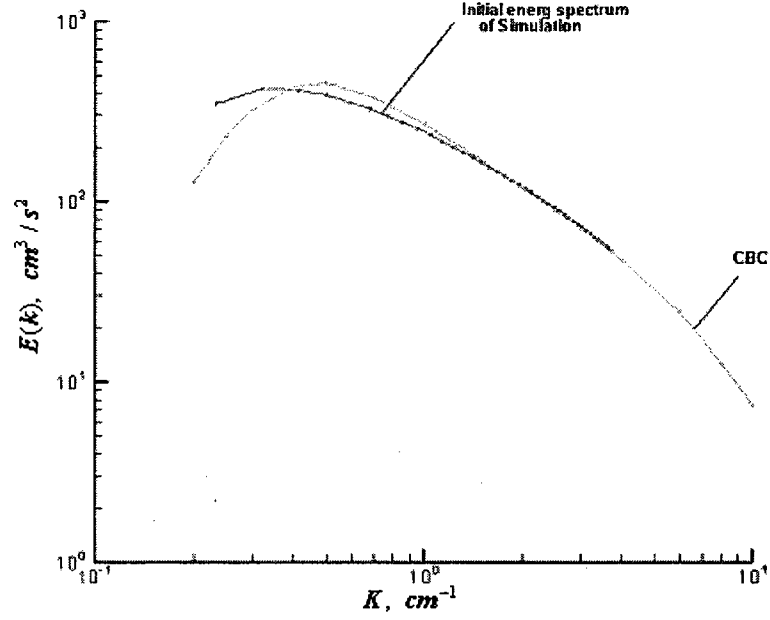


Fig. 4.6 Energy spectrum at $U_0 t_{CBC} / M = 42$.

The length scale $L_\infty = 6.96889\text{cm}$ and $U_\infty = 3420\text{cm/s}$ are chosen for nondimensionalization of the governing Eqs. (2.17-2.20) therefore the dimensionless length of cube's edges becomes equal to 2π .⁹⁵ The dimensionless time of the simulation (t) is related to t_{CBC} by:

$$t = \left(\frac{U_0 t_{CBC}}{M} - 42 \right) \frac{M U_\infty}{U_0 L_\infty} \quad (4.40)$$

and thus

$$t = 2.493 \left(\frac{U_0 t_{CBC}}{M} - 42 \right) \quad (4.41)$$

The flow in the experimental is essentially incompressible. The turbulence Mach number (M_t) of the initialization is equal to $0.98959541 \times 10^{-3}$ where

$$M_t = \sqrt{u_i u_i} / a_\infty \quad (4.42)$$

and $a_\infty = 3420\text{cm/s}$. Isosurfaces of dimensionless vorticity are shown in Fig. 4.7.

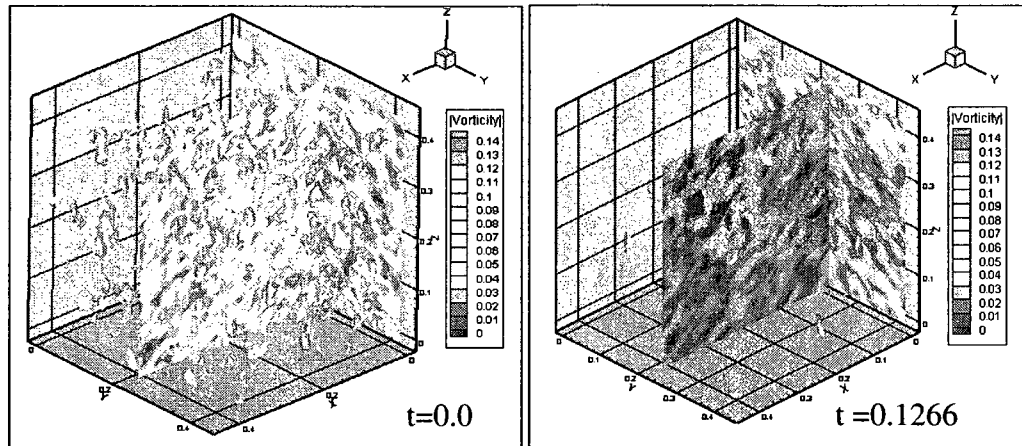


Fig. 4.7 Non-dimensional vorticity at non-dimensional times $t=0.0$ and $t=0.1266$.

In earlier works, spectral methods have been mainly used for simulation of decaying turbulence.^{62,64,77,80,98} For example, in Ref. 77 a fully spectral method with 2nd order Rung-Kutta time discretization has been implemented. The results are very good especially at higher modes. In Ref. 62 a method using pseudo-spectral Fourier collocation has been used which also has shown a very good prediction for higher modes. In that reference, the same resolution as this paper has been considered. The numerical dissipation was relatively negligible and therefore the SGS model has been mainly the factor to determine the overall dissipation of the simulation.

Other numerical methods, however, usually are not as accurate as spectral methods. Therefore an important numerical consideration, when evaluating a LES scheme, is the need to use an analysis, which will exhibit interactions between subgrid model (SGS) and the numerical error. These two terms may be even of the same order of magnitude.

It is not possible only to use the overall judgment to estimate the relative importance of each of these parameters. For example, in Ref. 78 an explicit streamline-upwind finite element method with the second-order accuracy both in time and space has been applied. According to their results, the applied numerical method has no extra dissipation (considering the case with no explicit SGS (NMU case)) and they have even reported an unphysical energy accumulation in the highest modes which is considered as a form of error. On the contrary to the previous example, however there have been cases, reported in the literature, in which numerical dissipation of the method was found to be significant. For example, in Ref. 79 compressible isotropic turbulence at zero molecular viscosity with a wide set of schemes, such as: the

Jameson scheme, TVD-MUSCL scheme (3rd order) and three schemes within the ENO family (ENO, WENO, MENO) have been studied. They concluded that numerical dissipation affects not only the small scales but also the large ones. MUSCL also has been found to be too dissipative at 64³. Another example would be Ref. 12, in which numerical method is based on a finite-volume discretization using MUSCL solver. A “self-adaptive” method has been implemented to remedy the over dissipative nature of MUSCL method and has given acceptable results for 32³. They also reported that the original scheme was over dissipative and for 32³ grid, the numerical dissipation was in general dominant over the sub-grid scale component.

Table 4.3 Explanation of different cases for decaying turbulence simulation.

Case #	Upwinding Parameters			C _s
	Upper value of γ	Lower value of γ	θ	
1	1.0	1.0	-	0.01
2	1.0	0.0	0.0	0.01
3	1.0	0.0	-0.00001	0.01
4	1.0	0.0	-0.0001	0.01
5	1.0	0.0	-0.0001	0.1
6	1.0	0.0	-0.0001	1.0

Considering the discussion above, one of the main concerns in this research is to study the effects of numerical dissipation of Roe-MUSCL scheme and introduce a method (self-adaptive upwinding) in order to control its undesirable influence.

To study the effects of the self-adaptive upwinding, test cases described in Table 4.3 are considered. Case 1 shows the set of conditions representing full upwinding. The numerical dissipation is found to be very high (Fig. 4.8) and therefore it is necessary to significantly decrease the upwinding effect.

In cases 2, 3 and 4 the effect of self-adaptive upwinding is demonstrated. In case 2, self-adaptive upwinding flag is activated and therefore the graph is significantly closer to CBC data points (Fig. 4.8). In this case θ is set to 0.0 which means that the self-adaptive scheme tries to dissipate the wiggles in low length scales (Fig. 4.9). This of course contradicts somehow in principle with the idea of LES in which energy stored at higher modes is expected to play a role in the simulation. Therefore in the next test cases, θ is decreased, hoping that it will improve the energy distribution in the highest modes.

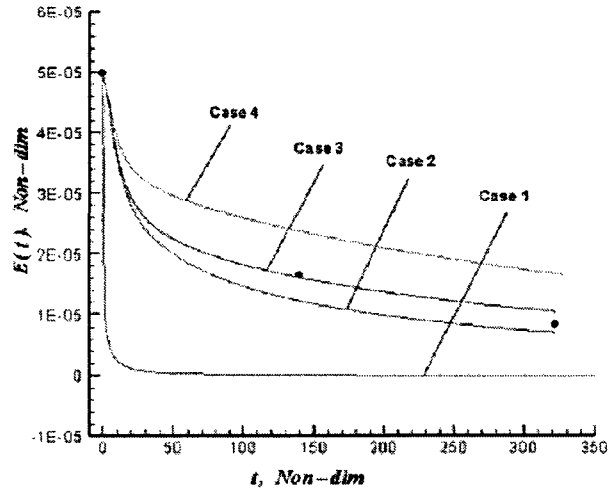


Fig. 4.8 Total kinetic energy (Cases 1, 2, 3, 4).

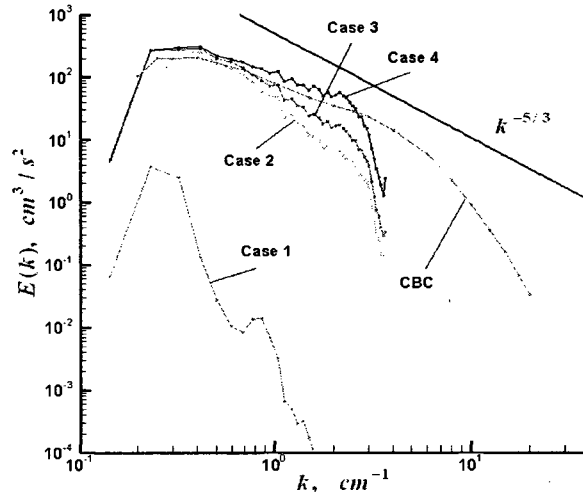


Fig. 4.9 $E(k)$ at $U_0 t_{CBC} / M = 98$ (Cases 1, 2, 3, 4).

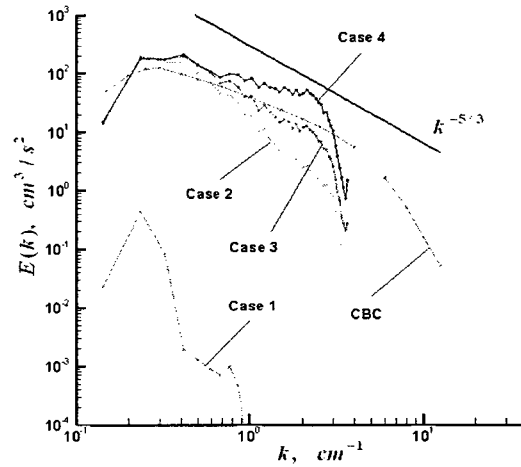


Fig. 4.10 $E(k)$ at $U_0 t_{CBC} / M = 171$ (Cases 1, 2, 3, 4).

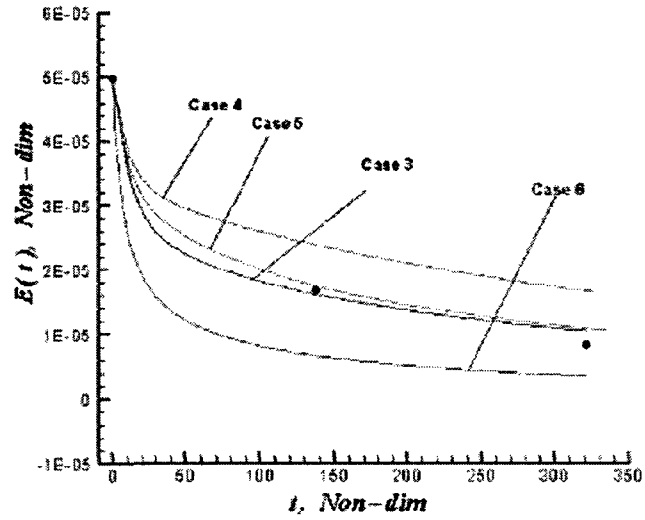


Fig. 4.11 Total kinetic energy (Cases 3, 4, 5, 6).

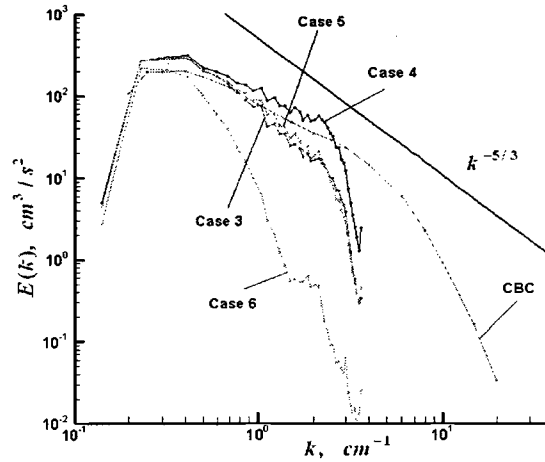


Fig. 4.12 $E(k)$ at $U_0 t_{CBC} / M = 98$ (Cases 3, 4, 5, 6).

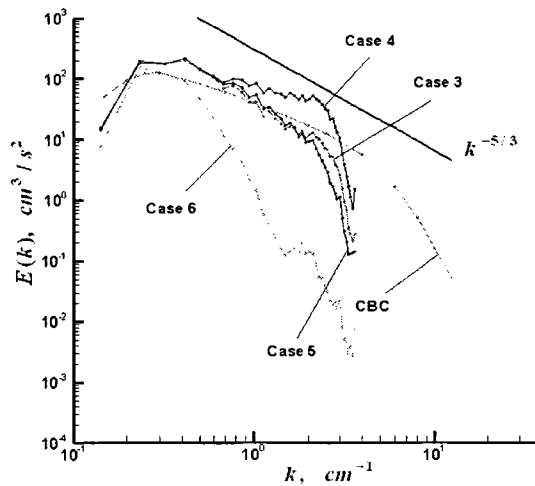


Fig. 4.13 $E(k)$ at $U_0 t_{CBC} / M = 171$ (Cases 3, 4, 5, 6).

In case 3, θ is decreased to -0.00001 and therefore total kinetic energy becomes a very good match of the experimental data. Results of Case 4, however show that the $E(t)$ graph can even elevate further upward by decreasing the θ further. In this case the slope of the energy spectrum is a better match for the CBC data even though the total kinetic energy is clearly higher than the experimental predictions.

As it is seen in Figs. (4.9,4.10) the energy is cascaded from lower modes toward higher modes. The energy spectrum is showing a dissipative nature at higher modes while it is not enough dissipative in relatively low modes and an undesired overshoot is present. By decreasing θ , not only the energy in higher modes is increase, but also some energy in lower modes is accumulated therefore it is difficult to achieve a complete match between numerical and experimental data as it was seen in the case of spectral methods.

In case4, 5 and 6 the effect of explicit SGS is studied (Figs. 4.11-4.13). By increasing the Smagorinsky constant the energy in the domain is more dissipated and that results in different levels of $E(t)$ as seen in Fig. 4.11. We conclude that the self-adaptive upwinding scheme has significantly improved the results as it was explained above. It was also found that the overall dissipative nature of simulation is affected by both SGS model and the numerical method.

4.2.1 Interaction of the Limiter Function and the Upwinding Term

The main idea in CFD is to use a high order method (2^{nd} order here) when the solution is relatively smooth but to apply a low order scheme and increase the amount of numerical dissipation in the neighborhood of discontinuities. Limiter functions are usually providing this switch in the numerical method especially for supersonic flows. The upwinding term, on the other hand, contributes directly to the numerical dissipation and the interaction between scheme's upwinding and implemented limiter function can affect the accuracy and performance of the numerical method.

In our simulations, the Van Leer-Van Albada limiter (Eq. 3.6) is implemented. It controls the spatial approximation's accuracy for the primitive variables and therefore it affects the numerical dissipation. As it is shown in Eq. (3.6), this limiter function shifts the numerical method locally toward a 1^{st} order scheme whenever $g(\Delta\phi^C, \Delta\phi_{ji}^D)$ shifts toward 0. On the other hand, when $g(\Delta\phi^C, \Delta\phi_{ji}^D)$ becomes close to $\Delta\phi_{ji}^D$

then the approximation becomes closer to second order. As it was mentioned before, $\varphi = [\rho, u, v, w, p]$,

$\Delta\varphi^C = \varphi_j - \varphi_i$ and $\Delta\varphi_{ji}^D \in (\Delta\varphi_{ji}^R, \Delta\varphi_{ji}^L)$ are based on the connectivity of an edge.

In order to study the effect of the limiter function, a limiter coefficient is defined for a typical node, j as bellow:

$$\text{Limiter coef.}(\varphi)_j = \frac{\sum_{k=1}^n \left(\frac{g(\Delta\varphi^C, \Delta\varphi_{ji}^D)}{\Delta\varphi_{ji}^D} \right) \times dA_k}{\sum_{k=1}^n dA_k} \quad (4.43)$$

in which n is the total number of edges connected to node j and dA_k is the area affiliated to edge k . Edge k is among the edges that are connected to node j .

The limiter function's average effect over the entire domain is estimated by the average limiter coefficient:

$$\overline{\text{Limiter coef.}(\varphi)} = \frac{\sum_{j=1}^m \text{Limiter coef.}(\varphi)_j}{m} \quad (4.44)$$

m is the total number of nodes inside the domain. Similar approach is used to define upwinding coefficient and average upwinding coefficient:

$$\text{Upwinding coef.}(j) = \frac{\sum_{k=1}^n (\gamma_j \times dA_k)}{\sum_{k=1}^n dA_k} \quad (4.45)$$

$$\overline{\text{Upwinding coef.}} = \frac{\sum_{j=1}^m \text{Upwinding coef.}(j)}{m} \quad (4.46)$$

The average limiter coefficient for cases 1 and 3 (Table 4.3) of the isotropic decaying turbulence simulation is shown in Figs. 4.14 and 4.16. In case 1, the full-upwinding scheme is applied and therefore the average value of upwinding coefficient inside the domain is equal to 1. As it is shown in Fig. 4.14, the initial turbulence velocity distribution has activated the limiter function but at least for velocities the applied spatial approximation is still close to second order.

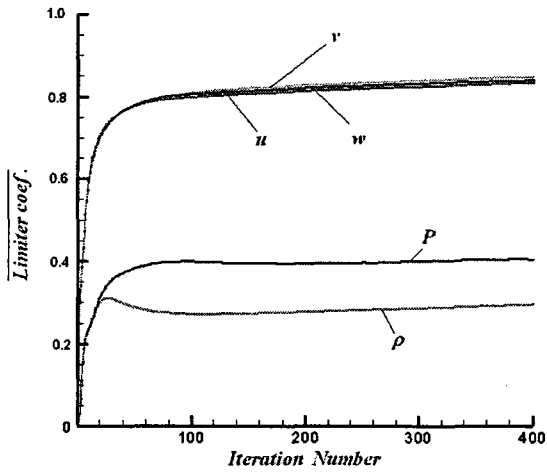


Fig. 4.14 Average limiter coefficient (Case 1).

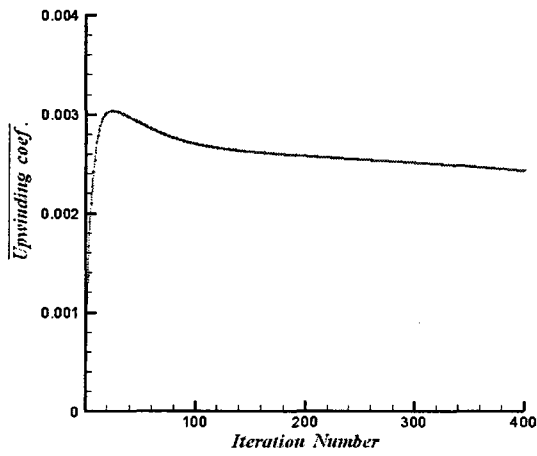


Fig. 4.15 Average upwinding coefficient (Case 3).

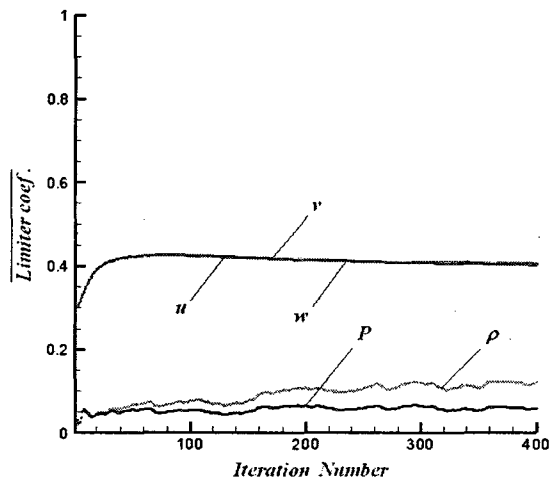


Fig. 4.16 Average limiter coefficient (Case 3).

The average limiter coefficient for density, velocities and pressure is 30%, 80% and 40% respectively. It is also shown in this figure that the velocity graphs for different axial directions (u, v, w) are overlapping. This is an indication of their isotropic distribution.

As it is shown in Fig. 4.15, when the self-adaptive scheme is applied the average upwinding coefficient decreases from 1 to 0.0025 which is resulting in a significant decrease in the introduced numerical dissipation. This also decreases the average limiter coefficient inside the domain. This activation of the limiter function is explained by the existence of more eddies in the simulated flow since they are not diffused when the self-adaptive upwinding method is applied and therefore fluctuations are more preserved by the numerical scheme. The average limiter coefficient for density, velocities and pressure decrease to 10%, 40% and 5% respectively which is in fact showing a shift toward using a more first order approximation and consequently introducing more numerical diffusion. This increase of introduced diffusion is however less than the amount which was removed as a result of decreasing the upwinding's coefficient and therefore the overall amount of numerical dissipation decreases.

Chapter 5

LES of a Round Compressible

Turbulent Free Jet

IN chapter 4, the performance of self-adaptive upwinding scheme was evaluated and the significant improvement resulted from its implementation was demonstrated. In this chapter, the developed numerical method is applied in order to simulate a compressible turbulent free jet ($Re_D = 0.66 \times 10^6$ and $Ma_j = 0.95$). Panda et al. (1999-2004),⁹⁹⁻¹⁰³ have done a series of experiments in order to measure the average and fluctuating density, velocity, pressure, their spectrums, generated noise levels and also $\langle \rho - \rho' \rangle$ and $\langle \rho u^2 - \rho' \rangle$ correlations. They implemented a very reliable experimental procedure and have very well documented their results. Therefore their data is used to verify the accuracy and validity of our LES in this chapter.

5.1 Experimental Setup and Measurements

During the experiments done by Panda et al. (1999-2004),⁹⁹⁻¹⁰³ flow characteristics of unheated-compressible-turbulent free jets in different Mach and Reynolds numbers have been measured. As it has been reported in the literature when the traditional hot-wire technique is used for measuring compressible free turbulent jets, the applied wire shows an undesirable tendency to breakage, especially for high Reynolds numbers. As an alternative approach, Laser Doppler Velocimetry (LDV) or Particle Image Velocimetry(PIV) methods which use particle based optical technique appear to be more suitable to provide the time-averaged measurements. Experimental study and measurement of the compressible

turbulent flows have some technical difficulties and as a result there are not many well documented experiments available in the literature for such jet flows.

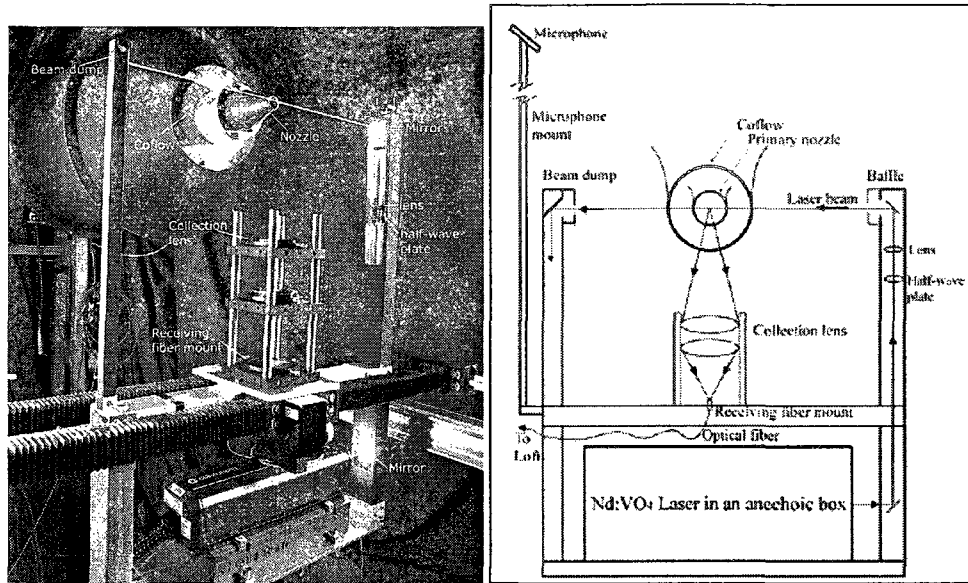


Fig. 5.1 First configuration of jet facility (Refs. 101,102).

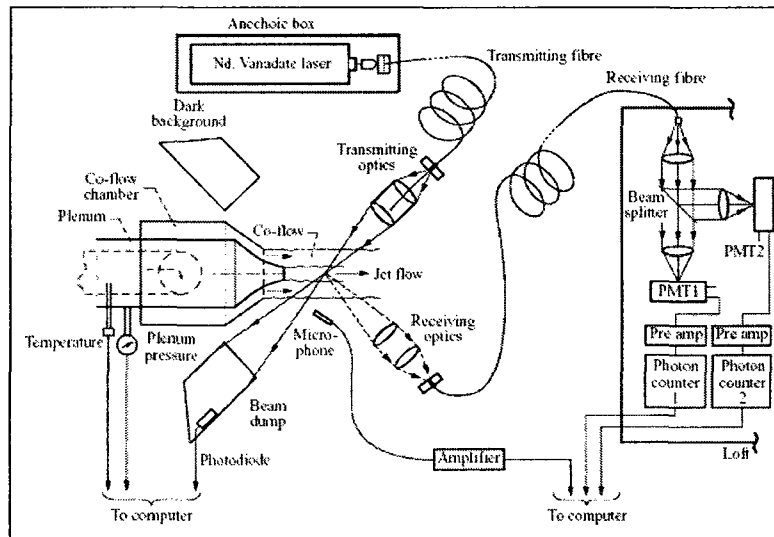


Fig. 5.2 Second configuration of jet facility (Refs. 99,100).

Experiments used for our validation were performed at NASA Glenn Research Center using convergent (for subsonic flow) and convergent-divergent (for supersonic flow) nozzles. These nozzles have been designed according to the method of characteristics and the exit diameter for both nozzles is equal to 25.4 mm. At first, air is compressed and is sent inside a reservoir by a compressor and then it is directed toward

the plenum of pressure and the nozzle. Two different experimental configurations used to do the measurements are shown in Figs. 5.1 and 5.2.

The acoustic absorbent material was mounted around the nozzle, inside the ceiling and the walls of the test room to prohibit any probable sound reflections. A 8" diameter low speed ($\approx 20m/s$) coflow was maintained around the primary jet using a source of filtered air in order to avoid particles through the entrained air. In these experiments, measurements were done based on the Rayleigh scattering method. In this method, a laser beam is passed through the gaseous medium of jet and molecules in the gas scatter the beam. The scattered light then is collected and spectrally resolved using a Fabry-Perot interferometer (Fig. 5.2).

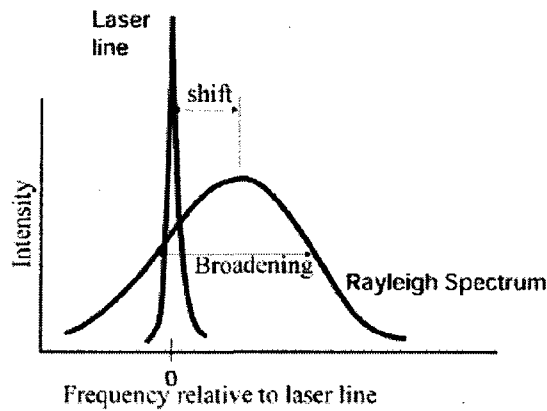


Fig. 5.3 Principle of Rayleigh scattering technique (Ref. 101).

The spectrum of the scattered light has a wider bandwidth (Fig. 5.3). This width is a function of the molecules' motion and is used as an indicator of the temperature. Since the average nonzero velocity of the molecules is superimposed on the random velocity of the molecules, a separation between the peak of the incident laser beam and the scattered Rayleigh spectrum appears. This separation provides a measure of the bulk velocity of the flow. Density is measure by calculating the integral of the Rayleigh scattered spectrum. In order to carry out that calculation, a photo-multiplier tube (PMT1) is used (Fig. 5.4). Since the intensity of the scattered portion is measured based on the number of photoelectrons (N) counted over a given time interval (Δt), the following relationship holds:

$$\rho = \frac{1}{a} \left(\frac{N}{\Delta t} - b \right) \quad (5.1)$$

in the above equations, a and b are constants which were determined through a calibration process.

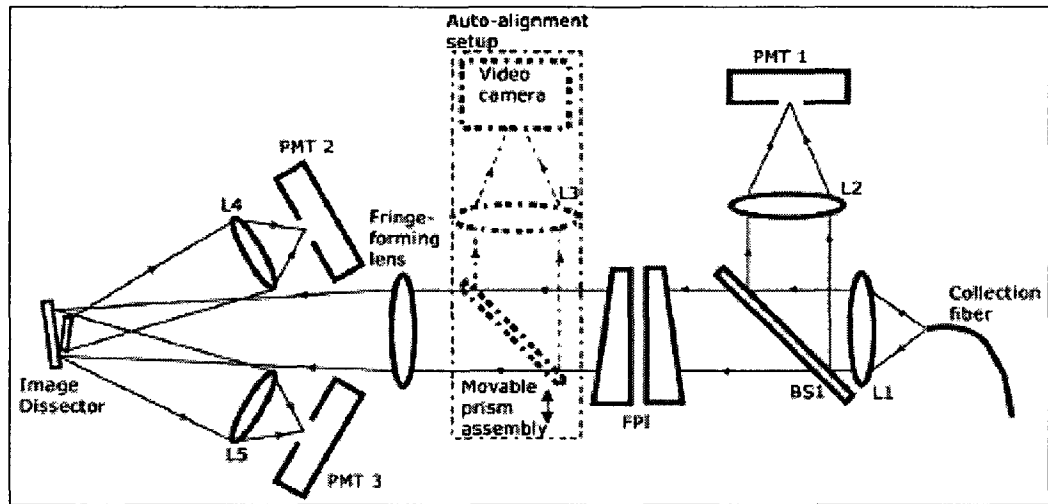


Fig. 5.4 Schematic of optical setup in a quiet, adjoining room to analyze the collected light, L_1 to L_5 are lenses; BS_1 is beam-splitter and FPI_1 is the Fabry-Perot interferometer (first configuration, Ref. 101).

When the distorted portion of the beam passes through the interferometer, it forms an image at the fringe-forming lens (Figs. 5.4,5.5). This image is then dissected into two parts by a concentric, tilted mirror and is measured by PMT2 and PMT2 units.

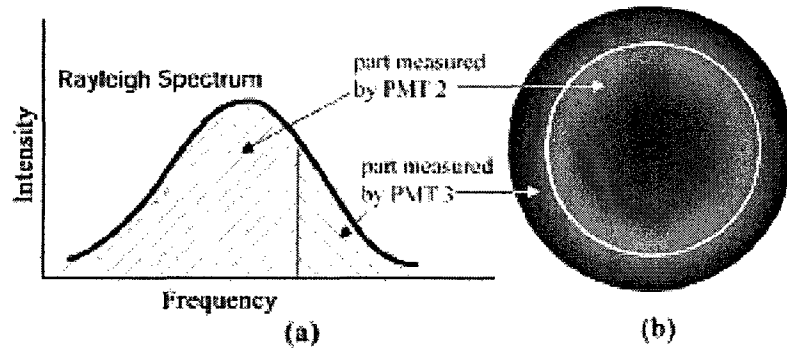


Fig. 5.5 Principles of velocity measurement by Rayleigh scattering technique (Ref. 101).

For small velocity fluctuations ($<150\text{m/s}$) the light intensity in either part of the dissected image is directly proportional to velocity. If N_2 and N_3 are the count rate from the inner and outer PMT2 and PMT2 then:

$$N_2 = c_1 + c_2 U_r \tag{5.2}$$

$$N_3 = c_3 + c_4 U_r \quad (5.3)$$

$$U_r = \frac{c_3 - \frac{N_3}{N_2} c_1}{\frac{N_3}{N_2} c_2 - c_4} \quad (5.4)$$

c_1, c_2, c_3, c_4 are the calibration coefficients and U_r is the radial velocity. The time-averaged measured quantities were reported to be quite accurate and therefore the absolute density numbers were found to be repeatable within $\pm 1\%$ of quoted values. The uncertainty of all reported quantities have been reported to be within $\pm 5\%$ considering the same nondimensionalization as it has been applied in the next section to present the numerical results.

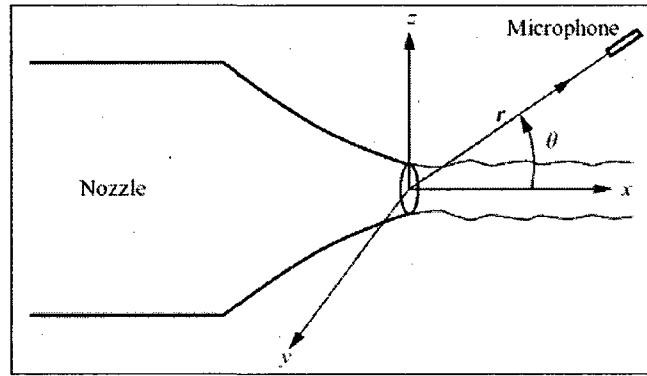


Fig. 5.6 The applied coordinate system and the location of microphones (Ref. 99).

In order to measure the spectrum of the pressure fluctuations, two microphones each with the diameter of $\frac{1}{4}$ in, were used. As it is shown in Fig. 5.6, the traversing system allows for measurements in the horizontal xy -plan while the microphones were located in the vertical xz -plan to minimize the effect of reflection from the large optical lenses and beam traps.

5.2 Numerical Setup

The simulation is carried out inside a cylindrical domain with a diameter equal to $60D$ and a length of $60D$ (D is the diameter of the inlet jet). 1,155,147 nodes and 6,859,200 tetrahedrons are used in this model (Fig. 5.7). Given that the computational time required for this simulation is very long, application of more refined grids is not possible.

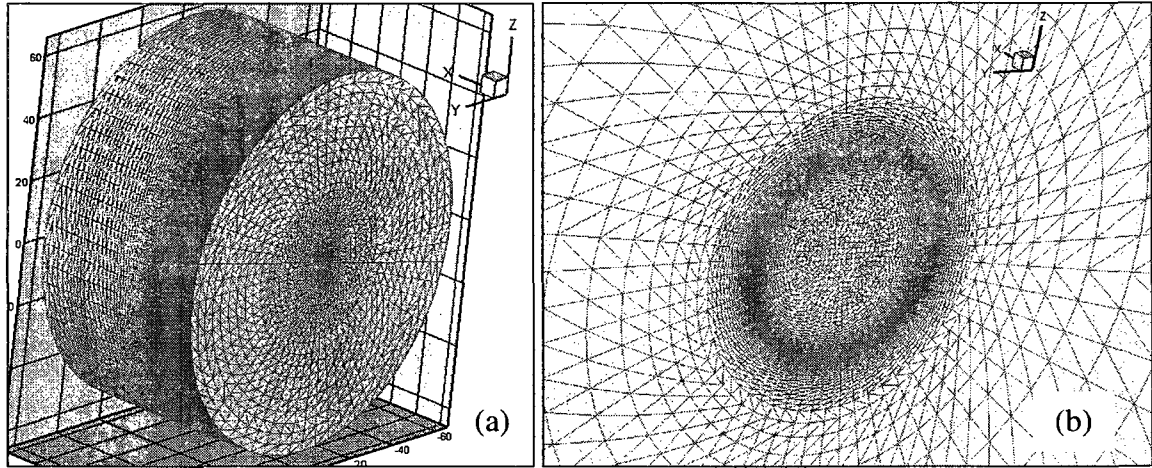


Fig. 5.7 Grid for the free jet simulation: (a) entire computational domain, (b) jet's inlet.

Nodes are separated from each other in the tangential direction by 6° and the grid sizes in the axial (h_x), radial (h_r) and tangential (h_θ) directions were carefully chosen so that generated elements close to the inlet are not very skewed. Elements aspect ratio inside the shear layer at the inlet is equal to 52 ($h_x/h_r \approx 7$ but $h_\theta/h_r \approx 52$). Its value gradually increases towards the downstream and it finally reaches to 2000 ($h_x/h_r \approx 2000$) at the end of the computational domain. This very high aspect ratio at the end of the computational domain creates a sponge zone with very high damping characteristics which removes all the flow's fluctuations and prohibits the outgoing flow to negatively affect the solution at the upstream.

Applied boundary conditions are shown in Fig. 5.8. As it was recommended by Bogey and Bailly (2006),¹⁰⁴ mean profiles of density, velocities and pressure are imposed at the inlet boundary (main jet and co-flow) while the non-reflective boundary condition are imposed over the other side boundaries. The shear layer between the main jet and the co-flow is modeled using a linear profile:

$$u = u(r) = \begin{cases} U_j & r/D < 1/2 - b_0/D \\ U_{co-flow} + \frac{(D/2 + b_0 - r)}{2b_0} (U_j - U_{co-flow}) & 1/2 - b_0/D \leq r/D \leq 1/2 + b_0/D \\ U_{co-flow} & 1/2 + b_0/D < r/D < 100/25.4 \end{cases} \quad (5.5)$$

$$\rho = \rho(r) = \begin{cases} \rho_j & r/D < 1/2 - b_0/D \\ \rho_a + \frac{(D/2 + b_0 - r)}{2b_0} (\rho_j - \rho_a) & 1/2 - b_0/D \leq r/D \leq 1/2 + b_0/D \\ \rho_a & 1/2 + b_0/D < r/D < 100/25.4 \end{cases} \quad (5.6)$$

in which b_0 is the thickness of the shear layer and its value was estimated to be $b_0/D = 0.0031$ by the experiment.

Inlet's pressure is set to the ambient value while the radial and tangential velocities are set to zero. The thickness of the shear layer is very small at the jet's inlet and only 4 nodes fall within that layer. As a result, application of more precise profiles for the variables at the inlet seems to be unnecessary.

It has been shown in Ref. 44 that existence of co-flow stabilizes the flow field and therefore delays the transition and results in a longer potential core. In our jet simulation, $U_{co-flow}/U_j = 0.06$ and therefore the transition is not expected to take place close to the inlet. This conclusion has been also confirmed by the experiment therefore considering an extra entrainment zone doesn't seem to be necessary. All the numerical parameters applied in the simulation have been reported in Table 5.1.

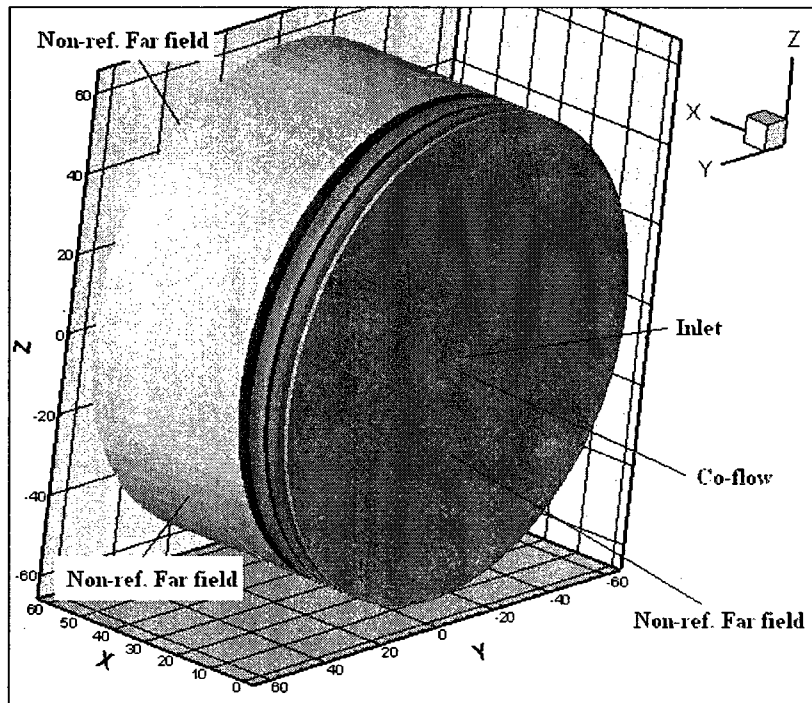


Fig. 5.8 Boundary conditions for compressible turbulent free jet.

In our simulation only the measurements for Mach number of 0.95 are considered and the corresponding operating conditions are given in Table 5.2.

Table 5.1 Comparison of used parameters in different numerical simulation.

Numerical tool	Compressible, Code
Number of nodes	1,155,147
Number of elements	6,859,200
No. of CPUs	128
Maximum CFL	10
Elapsed time of every CPU	144hours
C_s	0.1
Upwinding Parameters	
Upper value of γ	1.0
Lower value of γ	0.0
θ	-0.0001

Table 5.2 Operating conditions for the experimental measurements.

Nozzle Type	Convergent
Re_D	0.66×10^6
Ma_j	0.95
D	25.4 mm
$D_{co-flow}$	200 mm
Jet Velocity, $U_j (m/s)$	316
Co-flow Velocity, $U_{co-flow} (m/s)$	20
Jet Density, $\rho_j (kg/m^3)$	1.36
Estimated Eddy Convection Speed $U_C (m/s) = 0.6U_j - 0.89U_j$	190-282
Jet Static Temperature, $T_j (^\circ K)$	275.4
Ma_a	0.91
Ambient Speed of Sound $C_a (m/s)$	347
Ambient Density $\rho_a (kg/m^3)$	1.16
Ambient Temperature, $T_a (^\circ K)$	300

5.3 Numerical Results

The distribution of instantaneous density and Mach number are shown in Figs. (5.9-5.10). It is shown in Fig. 5.9 that the simulation has been successful in capturing the Kelvin-Helmholtz instabilities as it was explained in chapter 1.4.1. Rolling-up phenomenon initiates inside the shear layer; it intensifies as the flow moves further downstream and it finally destructs the potential core.

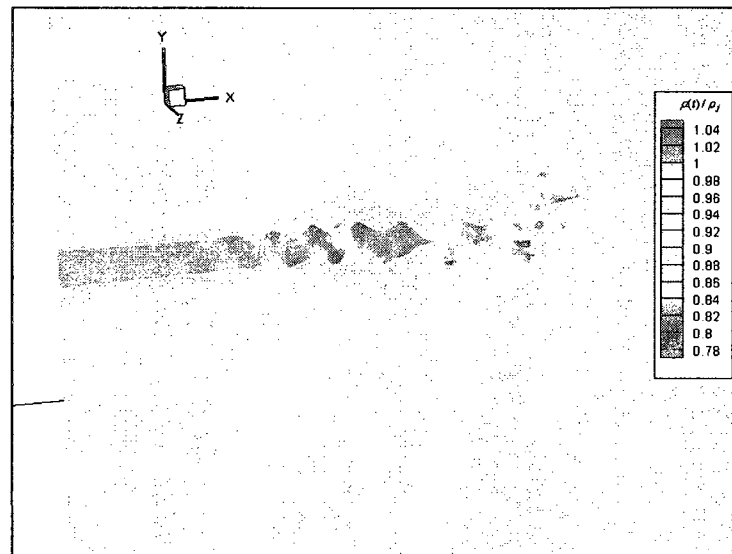


Fig. 5.9 Instantaneous distribution of density ($\rho(t)/\rho_j$).

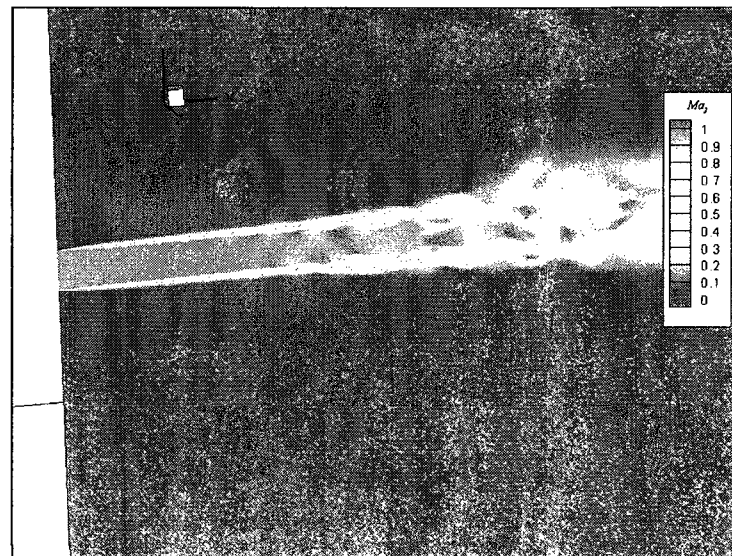


Fig. 5.10 Instantaneous distribution of Mach number (Ma_j).

In Fig. 5.10, some local supersonic waves are observed. That is mainly because Mach number of the simulation is 0.95 and therefore the flow is very close to the sonic state. As it will be shown later, these relatively weak shocks do not significantly affect the average distribution of variables (Fig 5.15). Figure 5.11 shows the dimensionless vorticity distribution. Rolling up phenomena is clearly taking place and generates large scale eddies. These large scale motions will break into smaller eddies and scales as the flow travels downstream.

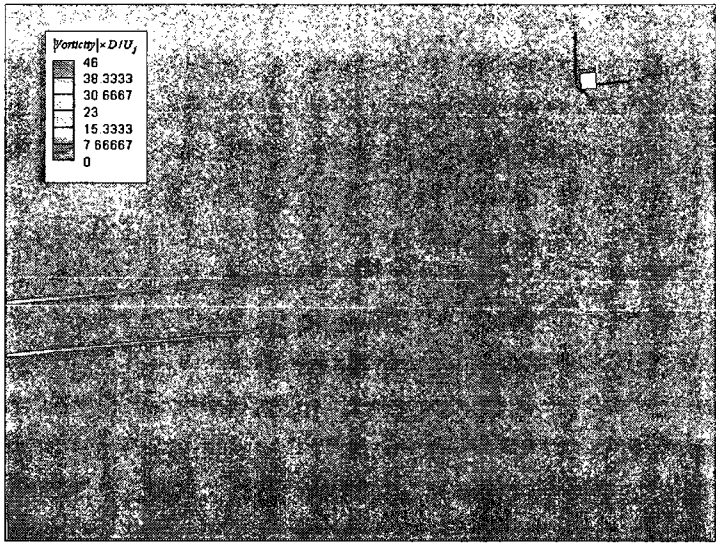


Fig. 5.11 Instantaneous distribution of vorticity ($0 \leq |Vorticity| \times D/U_j \leq 46$).

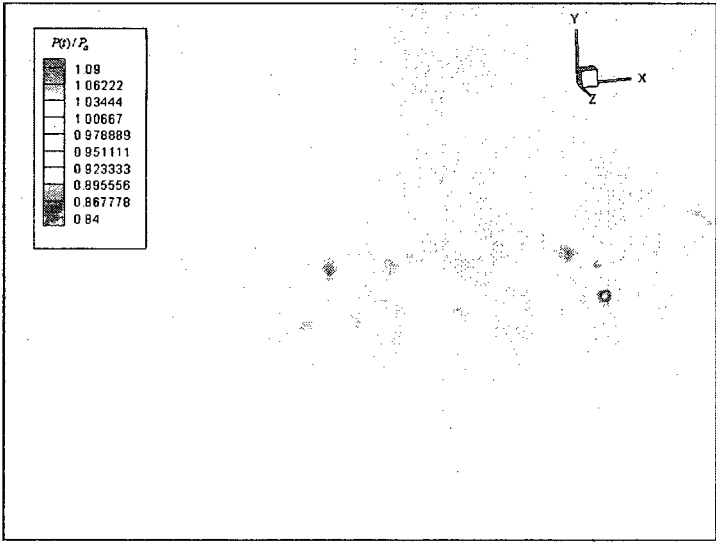


Fig. 5.12 Instantaneous distribution of pressure ($P(t)/P_a$).

Pressure fluctuations generated by roll-ups are also shown in Fig. 5.12. As flow travels further downstream, the Kelvin-Helmholtz instabilities grow stronger and generate instantaneous fluctuations in the pressure field.

In this simulation, maximum CFL is equal to 10 and time step is set equal to $\Delta t = 2 \times 10^{-7} s$. In order to calculate the statistical properties of density, velocity; the data acquisition is performed once every 50 iterations. For every location inside the domain 5130 data samples are stored which is equivalent to 0.0513s in the simulation.

The average axial velocity profile at $X/D = 0.1$ is shown in Fig. 5.13. As it was mentioned before, a co-flow ($U_{co-flow}/U_j = 0.06$) has been considered in this simulation. The effect of this co-flow is present in the mean profile but the reason for its absence in the experimental data is not clear. In Fig. 5.14, the average axial velocity profile at $X/D = 1.0$ is shown. The measured profile demonstrates existence of a higher level of dissipation in the flow in comparison to the simulation. Despite the fact that the Smagorinsky subgrid model's constant, chosen for this simulation is 10 times more than the value found in chapter 4 and also recommended in the literature for the isotropic decaying turbulence there is still a need for higher values.

Similar behavior has been reported by DeBonis (2004),²⁸ even though our applied numerical method is different from that reference. His obtained numerical results showed a strong dependence on the strength of the subgrid model. This phenomenon further demonstrates the need for development and application of reliable subgrid models which are more suitable for LES of highly anisotropic compressible flows. The dashed lines in Figs. 5.13 and 5.14 or the solid lines in Figs. 5.17 and 5.18 represent a curve fitting done in Refs. (99-103).

In Fig. 5.15, the average density profile along the jet's axis is shown. The length of the potential core is under-predicted which further emphasizes on the need for a stronger subgrid contribution at the early stages of the jet's development. Root-mean-square of density fluctuation along the jet's axis is also shown in Fig. 5.16. The fluctuation of density over-predicts the experimental profile. This behavior however has been observed in Ref. 105 and has also been reported in Ref 46. They have detected about 12-15% overshoot in the velocity fluctuation distribution (about 20% in the peak value). Their predicted density fluctuation has

been almost twice the measured data. The results of our simulation seem to be relatively better than those references. The uncertainty of measurements for $Ma_j = 0.95$ has been reported to be approximately 5%.

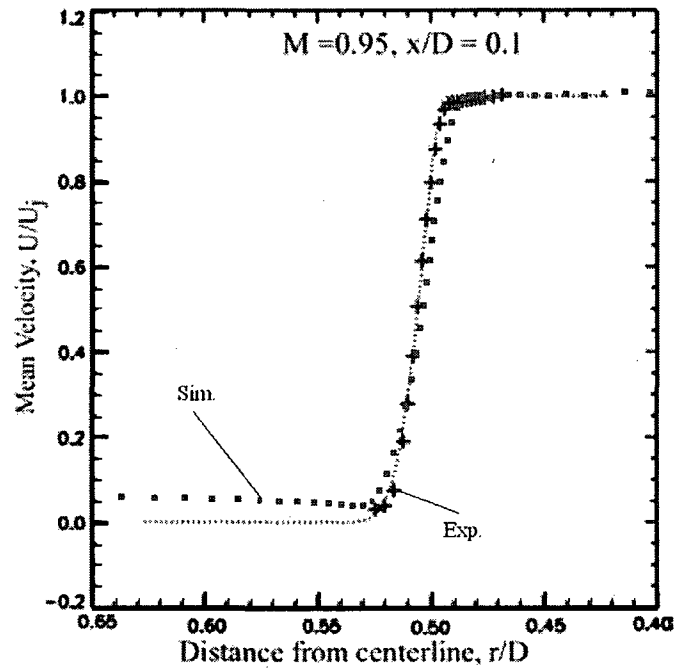


Fig. 5.13 Mean velocity distribution at $X/D = 0.1$.

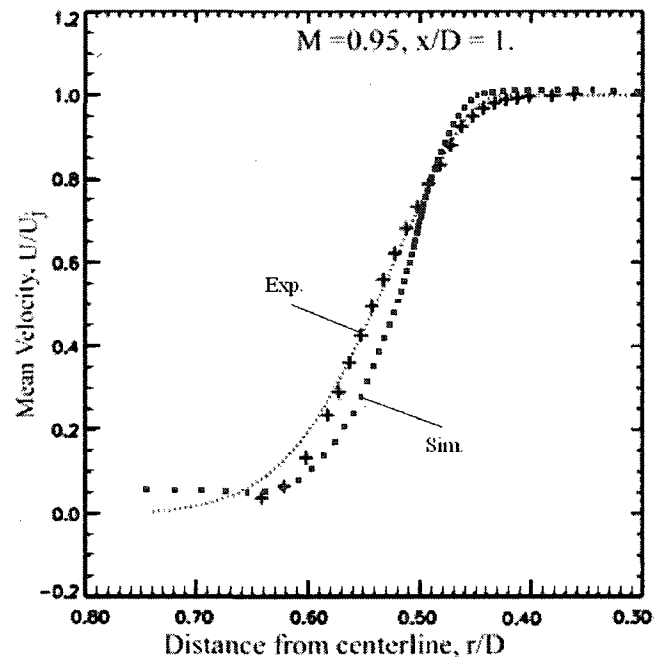


Fig. 5.14 Mean velocity distribution at $X/D = 1.0$.

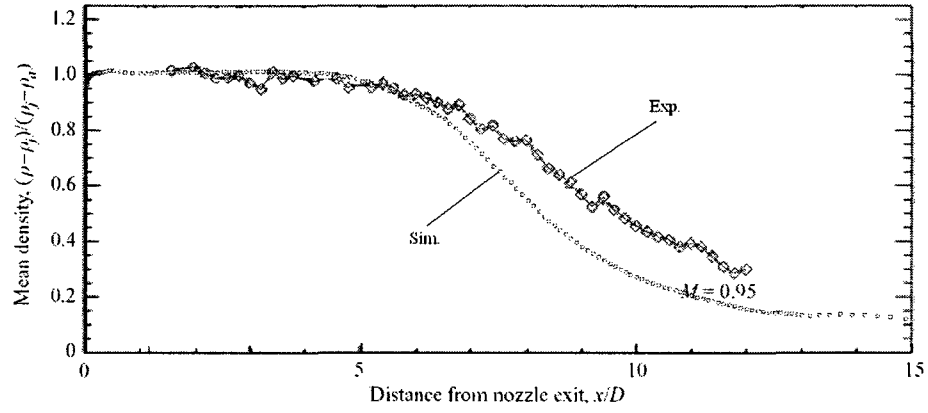


Fig. 5.15 Mean density distribution along the jet's axis.

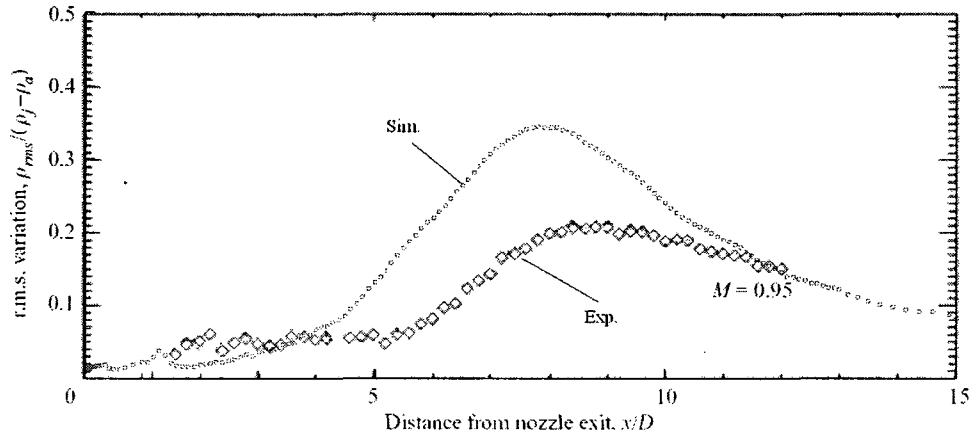


Fig. 5.16 rms of density fluctuations along the jet's axis.

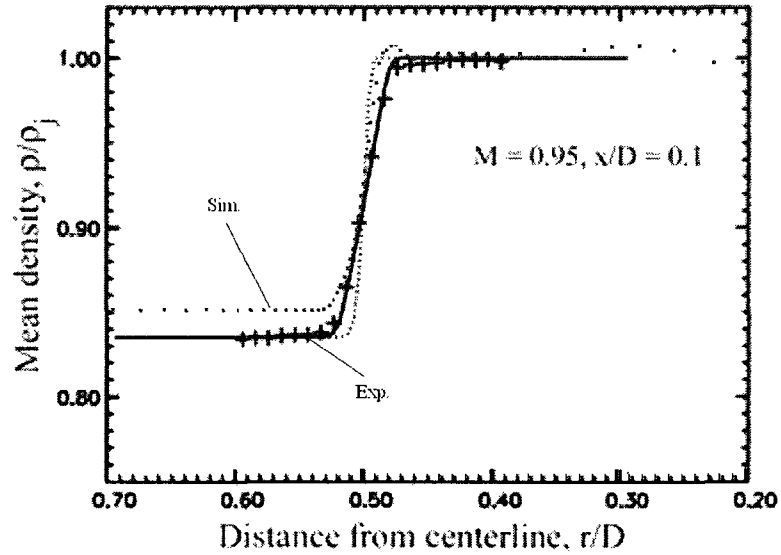


Fig. 5.17 Mean density distribution at $X/D = 0.1$.

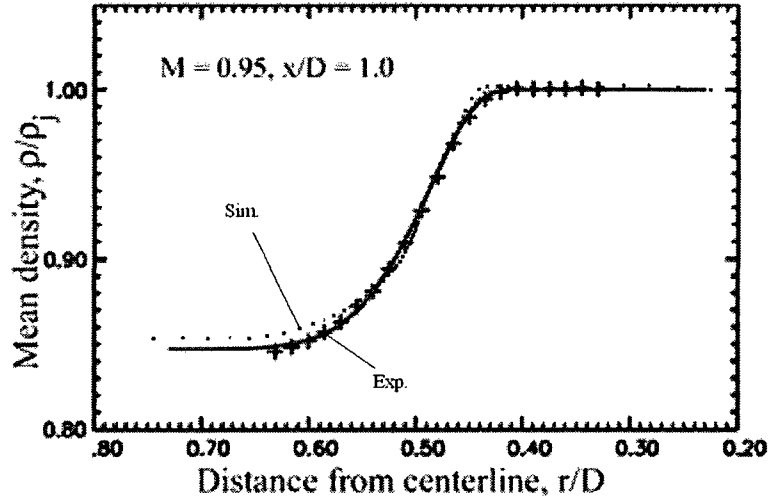


Fig. 5.18 Mean density distribution at $X/D = 1.0$.

In Fig 5.17 and Fig. 5.18, the distribution of mean density at $X/D = 0.1$ and $X/D = 1.0$ are shown respectively. The simulation's profiles match very well with experimental data. The farfield density is $\rho_a / \rho_j = 0.853$ but its effect has not been reflected into the experimental profiles and therefore the simulation results seem to be more realistic than the measurements.

The radial profiles of mean and fluctuating density at different axial locations are shown in Fig. 5.19 and Fig. 5.20. A transient region exists at $5 \leq X/D \leq 12$ wherein a very strong mixing takes place. The simulation over-predicts the fluctuation profiles, especially inside this region and that results in stronger mixing and therefore shorter transient region. In our simulation, the length of the potential core was underpredicted. Similar results also have been reported in Refs. 20 and 21 and many other references which were mentioned in the literature review chapter of this dissertation (chapter I).

In our simulation no artificial turbulent velocity forcing has been introduced at the inlet and therefore the numerical simulation has been expected to predict correctly the Kelvin-Helmholtz instabilities inside the shear layer based on the velocity difference between the jet stream, co-flow and the stagnant environment. In Refs. 7 and 34, the intensity of forced fluctuations has been deliberately adjusted in order to improve the results.

The applied numerical method seems to be able to reasonably predict Kelvin-Helmholtz instabilities and therefore result in acceptable velocity and density variation. The accuracy of the results decreases as the flow travels further downstream which could be because of insufficient grid resolution, especially at

regions far from the inlet. In our simulation, a very strong dependence of the results on the subgrid model has been observed. A considerably higher value of Smagorinsky subgrid model was required in our simulation and a similar conclusion has also been recently reported in Ref. 28.

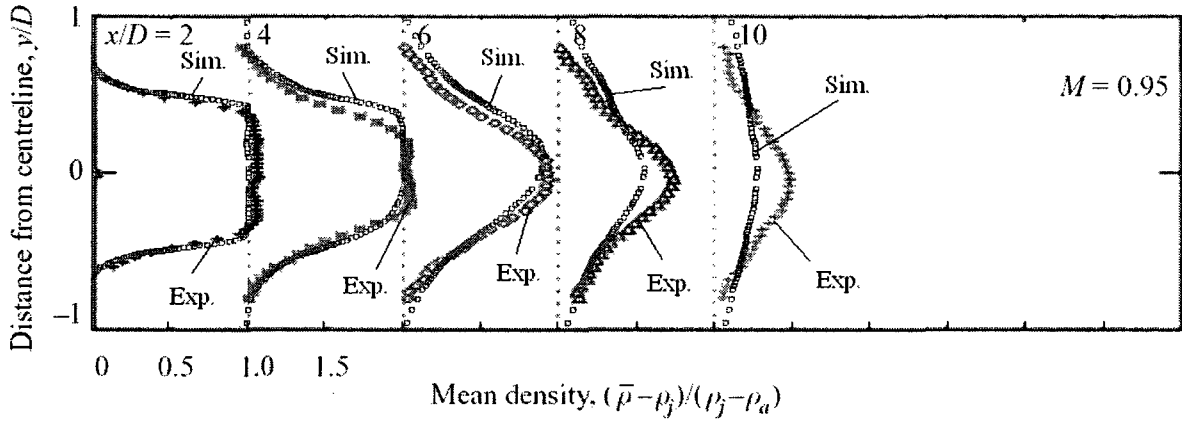


Fig. 5.19. Mean density distribution at different axial locations.

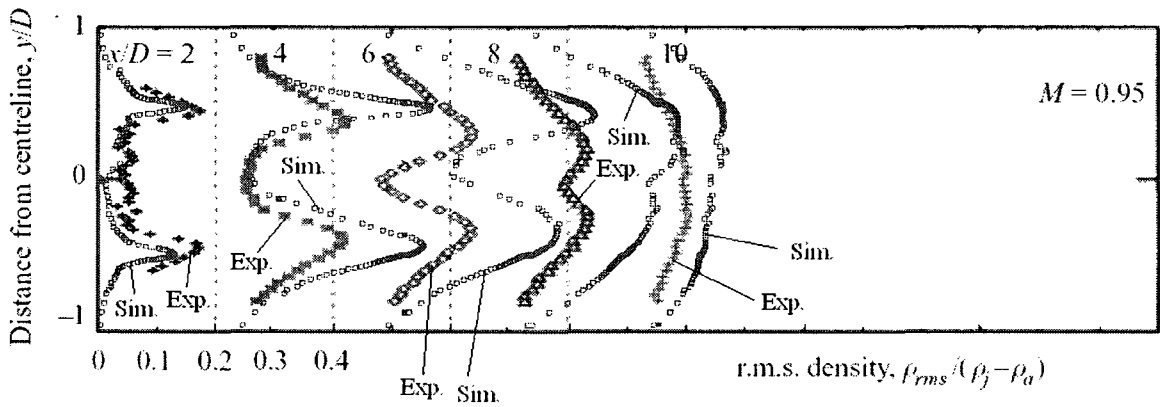


Fig. 5.20 rms of density fluctuation at different axial locations.

Chapter 6

LES of a Hydrogen Jet Releasing from a High Pressure Reservoir (100 atm)

IN this chapter the self-adaptive upwinding method is applied to simulate the hydrogen release from a high pressure reservoir. This simulation evaluates the performance of the self-adaptive scheme for a transient compressible turbulent supersonic flow in which the interaction between the shock waves and the large scale eddies is a fundamental factor in determining the flow regime. Results are compared with a RANS simulation which is carried out by the Roe-MUSCL full upwinding scheme.

6.1 Numerical Setup

The computational domain is composed of two main parts. The first part is the high pressure reservoir which is a 60° cut of a converging channel with an external diameter of $40D$. The diameter of this converging channel reduces to $D = 0.005\text{m}$ before its connection to the second part which is the external environment. The external environment is a cylinder of a diameter equal to $20D$ and is extended to $30D$ in the Z direction (Figs. 6.1 and 6.2). The computational grid contains 12,186,565 elements and 1,901,072 nodes. It has been generated in such way that it has very fine elements at the region where two main parts of the domain connect. The elements however become more skewed and coarser in downstream. The computational fluid in this simulation is hydrogen and it is assumed to be an ideal gas. The flow is initially at rest and its velocity is equal to zero everywhere inside the domain. The pressure inside the high pressure section is set to 100atm while the rest of domain has the atmospheric pressure. The initial temperature is

300° K everywhere inside the computational domain. All the computational conditions are given in Table.

6.1.

A slip boundary condition is applied over the walls of the high pressure reservoir. Pressure is also kept constant at the outlet of the external environment. The computational time step is set to $\Delta t = 2 \times 10^{-8} s$. Given that in LES the fluid equations are presumably not filtered in time and also considering that in this simulation the hydrogen jet is predicted to be supersonic, a rather small time step is chosen.

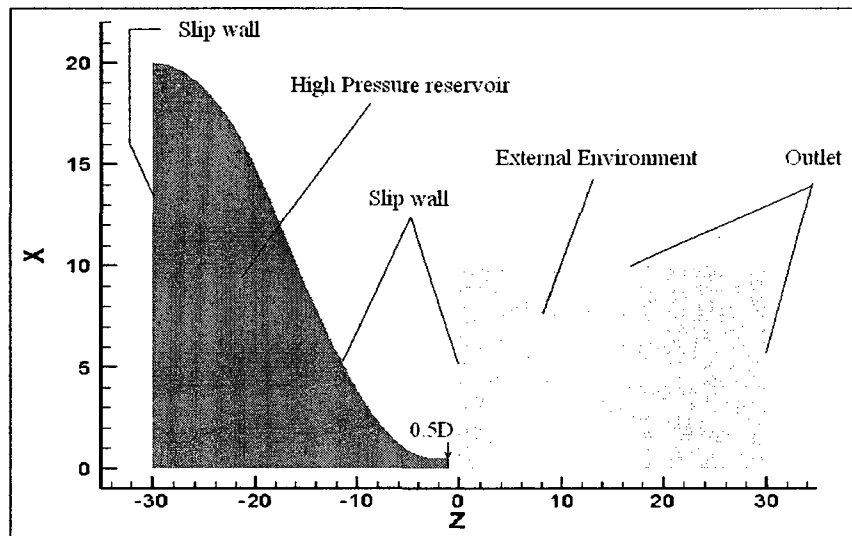


Fig. 6.1 Boundary conditions for the hydrogen release jet.

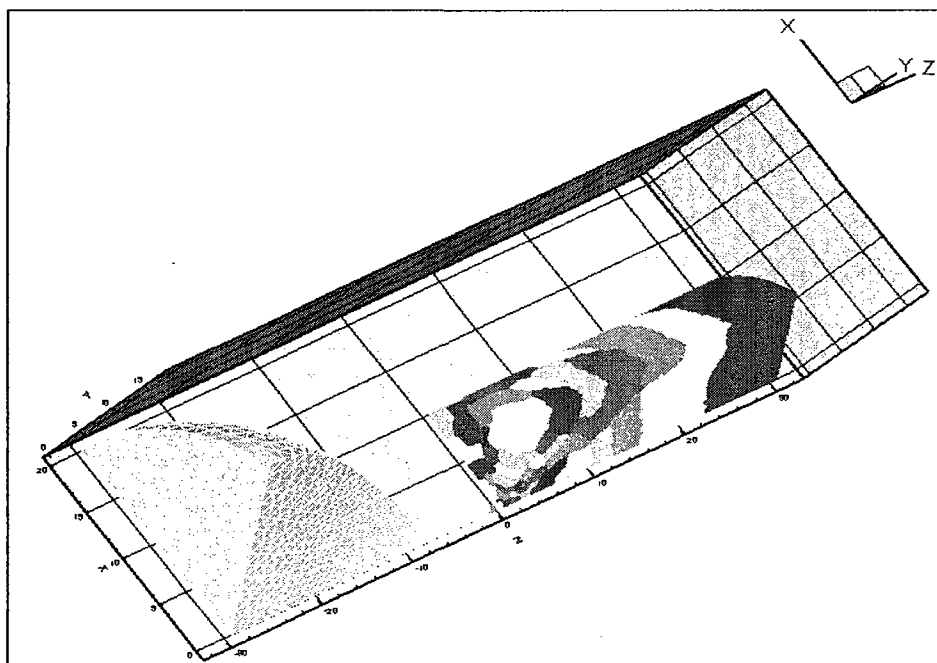


Fig. 6.2 3D grid and subdomains for the hydrogen release jet.

Table 6.1 Operating conditions for the hydrogen release simulation.

Nozzle Type	Convergent
D	0.005 m
Number of Nodes	1,901,072
Number of Elements	12,186,565
No. of CPUs	64
Initial Pressure of Hydrogen Inside the Reservoir, P_{in} (atm)	100
Initial Pressure of Hydrogen Outside the Reservoir, P_{out} (atm)	1
Initial Density of Hydrogen Inside the Reservoir, ρ_{in} (kg / m ³)	8.108275
Initial Density of Hydrogen Outside the Reservoir, ρ_{out} (kg / m ³)	0.08189
Initial Static Temperature (Inside and Outside the Reservoir), T (° K)	300

In order to preserve the stability of simulations against strong fluctuations, a 1st order-full upwinding flux calculation scheme is locally applied inside a small region where the two main parts of the domain connect ($-0.1 < Z/D < 0.1$ and diameter of D). Similar method is also applied whenever the ratio of Mach numbers along an edge becomes more than 1.5. The numerical scheme remains 2nd order in the rest of the computational domain. Given that all the elements attached to the centerline of the nozzle are adjacent to two symmetry faces, the self-adaptive scheme is not going to be able to perform accurately. Therefore the upwinding parameter for the edges, belonging to the first few rows of elements which are very close to the center line, is manually set to 1. The convergence of solution is also ensured through decreasing the residual by 6 degrees at every time step by the GMRES solver.

6.2 Numerical Results

In order to better demonstrate the performance of the self-adaptive scheme, two different test cases are considered (Table 6.2). In Case 1, the full Roe-MUSCL scheme is used without any subgrid model as in a RANS simulation. In Case 2, the self-adaptive upwinding is activated. The value of θ is set to -0.0001 and Smagorinsky subgrid model's constant (C_s) is chosen to be equal to 0.01. The contour graphs for density, Mach number and also temperature distribution of these test cases at different computational times are shown in Figs. (6.3-6.35).

Table 6.2 Explanation of different cases for hydrogen release jet.

Case #	Upwinding Parameters			C_s
	Upper value of γ	Lower value of γ	θ	
1	1.0	1.0	-	0.0
2	1.0	0.0	-0.0001	0.01

The development of both jets seems to be quite similar at the early stages of the simulations (for $t = 5.01\mu s$ and $t = 10.03\mu s$) but a gradual difference in the density, Mach and temperature distributions is observed as the simulation proceeds. The self-adaptive method seems to be more accurate than RANS simulation. As it is shown in Figs. (6.21-6.35), the main features of the jet such as jet boundary, Mach disk, barrel shock, 2nd vortices, slip line, reflected shock, 1st vortex and 1st shock are very well developed in Case 2 (these features have been detailed in Figs. 1.3 and 1.4). As it is shown, the self-adaptive upwinding scheme (Case 2) is much better in preserving the turbulent features of the flow in comparison to the full upwinding (Case 1), while the convergence and stability of the simulation is still provided. This demonstrates the high fidelity of the proposed scheme in a supersonic regime and further encourages us to apply the developed numerical tool for LES of supersonic flows.

In Figs. (6.36-6.38) flow density, Mach number and temperature at $Z/D = 10$ and for $t = 151.96\mu s$ are shown. As it is demonstrated for both test cases, flow evolution is not completely symmetric and therefore a full-360 degree numerical model is expected to produce more accurate results. Given the limitations in the available computational resources, generating a complete model has not been possible in this research.

Distributions of Mach number along the centerline for different computational times for both test cases are shown in Figs. (6.39-6.42). As it is shown in those figures, Mach number variations along the centerline for both test cases are very similar. At some of the computational times, there is often an overshoot right before the shock disk which is suspected to be the result of insufficient grid resolution and applying a low order numerical scheme. As it is seen in Figs. (3.39,6.41), the Mach disk moves towards downstream until it slightly passes $Z/D = 6.7$. Then it returns back and stays fixed in that location. All of this happens in less than a 0.0002s and that justifies choosing a time step in the order of 10^{-8} s.

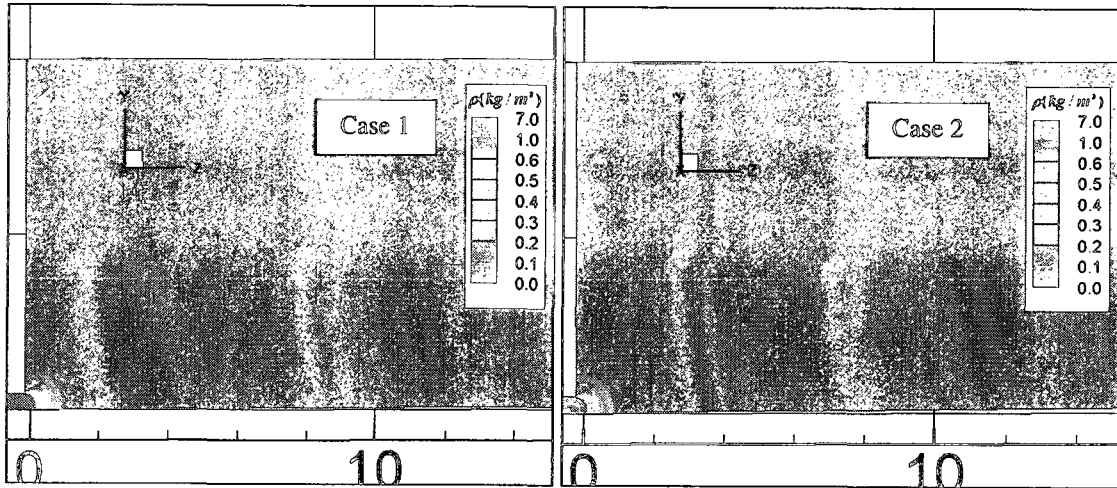


Fig. 6.3 Density contours for $0.0 \leq \rho \leq 1$ ($t = 5.01\mu\text{s}$).

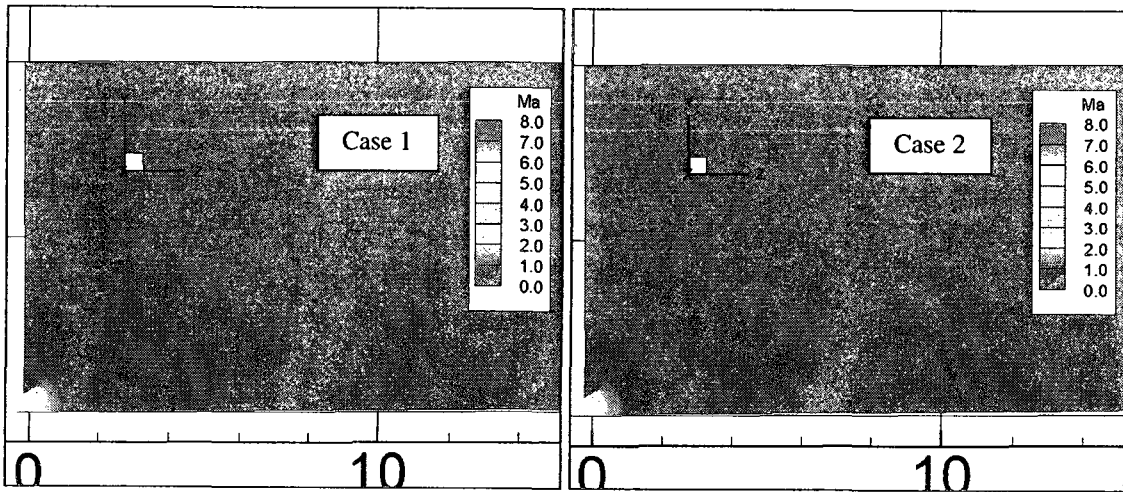


Fig. 6.4 Mach contours ($t = 5.01\mu\text{s}$).

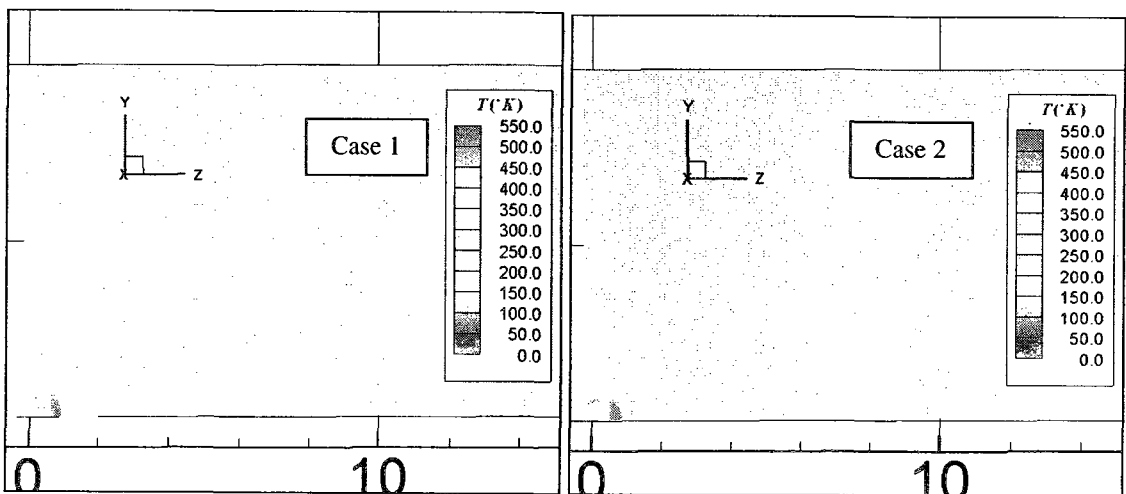


Fig. 6.5 Temperature contours ($t = 5.01\mu\text{s}$).

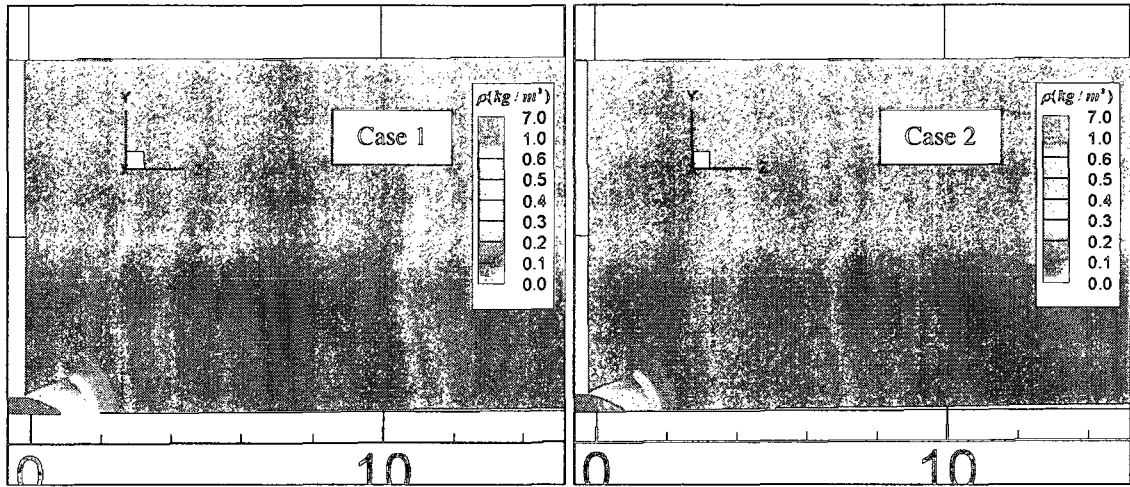


Fig. 6.6 Density contours for $0.0 \leq \rho \leq 1$ ($t = 10.03 \mu s$).

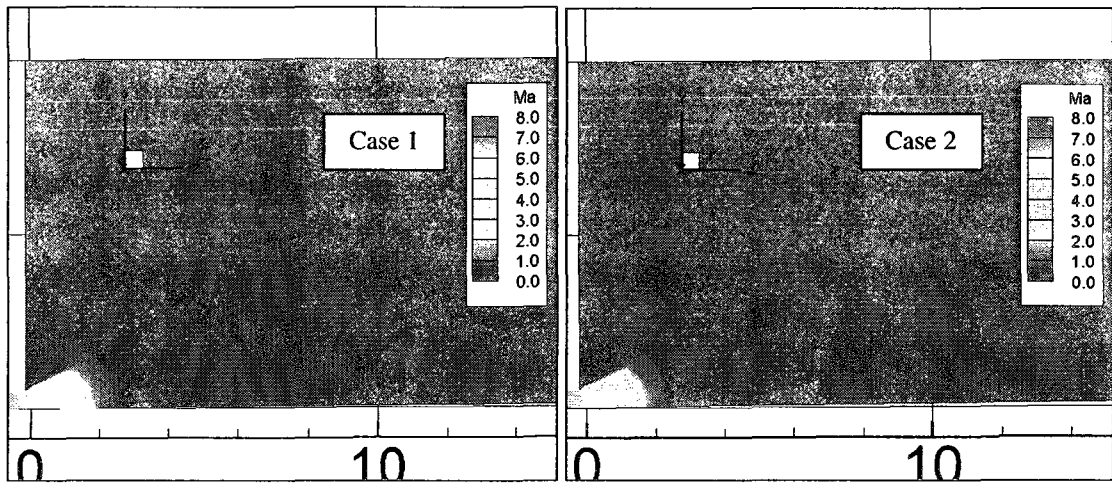


Fig. 6.7 Mach contours ($t = 10.03 \mu s$).

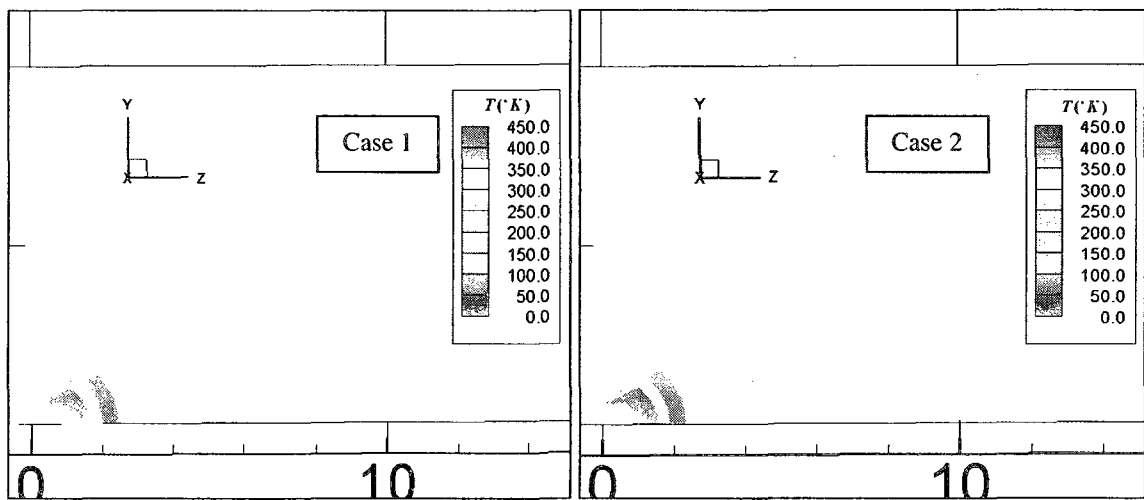


Fig. 6.8 Temperature contours ($t = 10.03 \mu s$).

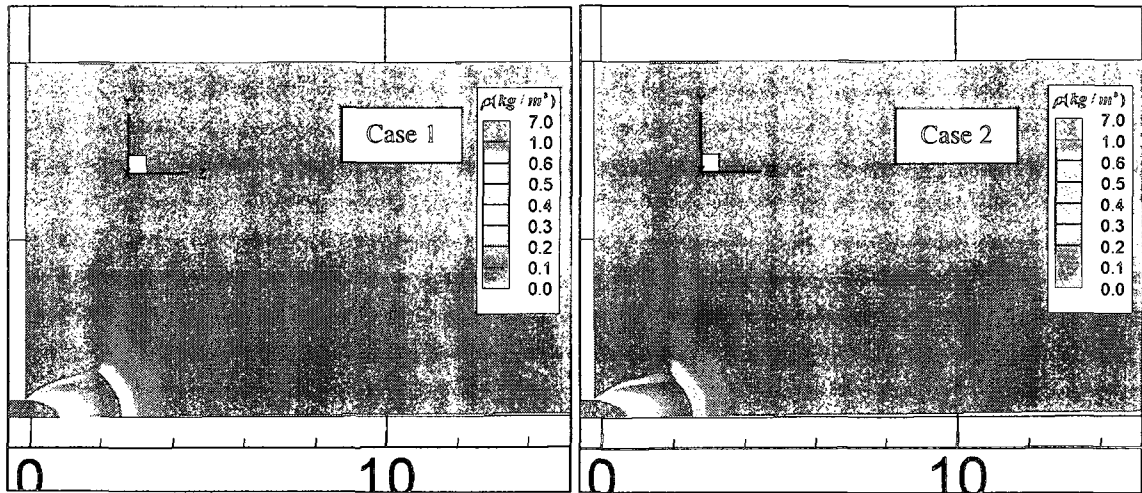


Fig. 6.9 Density contours for $0.0 \leq \rho \leq 1$ ($t = 15.09 \mu s$).

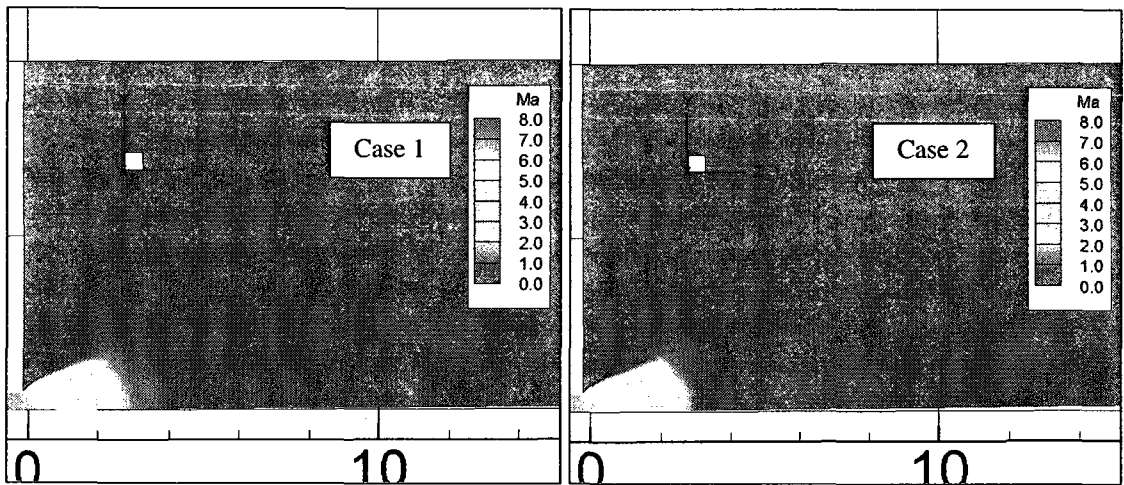


Fig. 6.10 Mach contours ($t = 15.09 \mu s$).

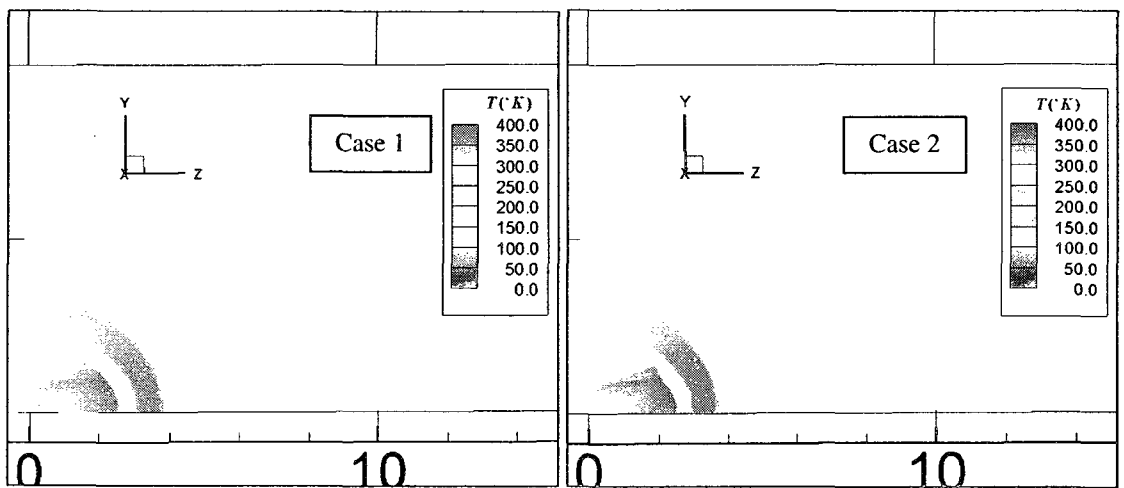


Fig. 6.11 Temperature contours ($t = 15.09 \mu s$).

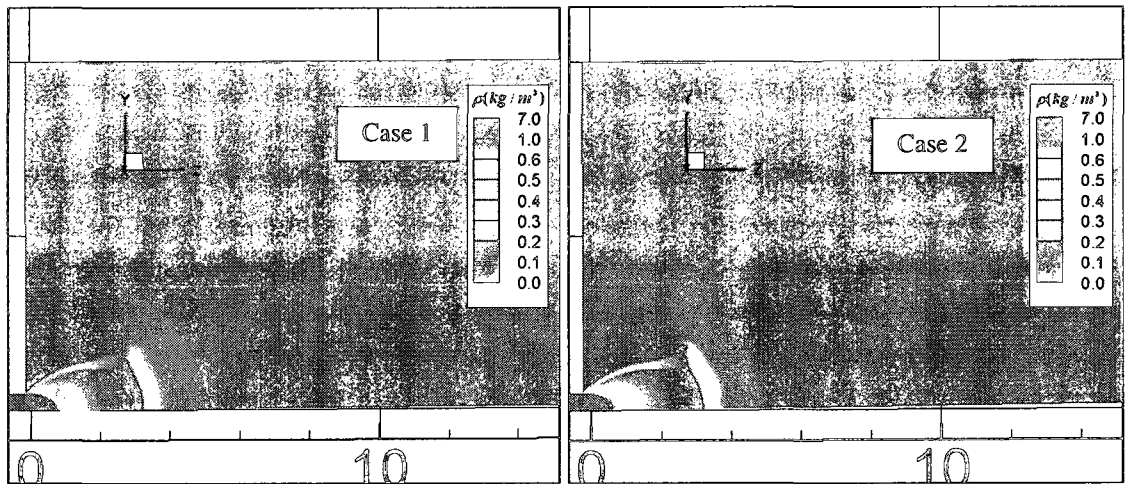


Fig. 6.12 Density contours for $0.0 \leq \rho \leq 1$ ($t = 20.09 \mu s$).

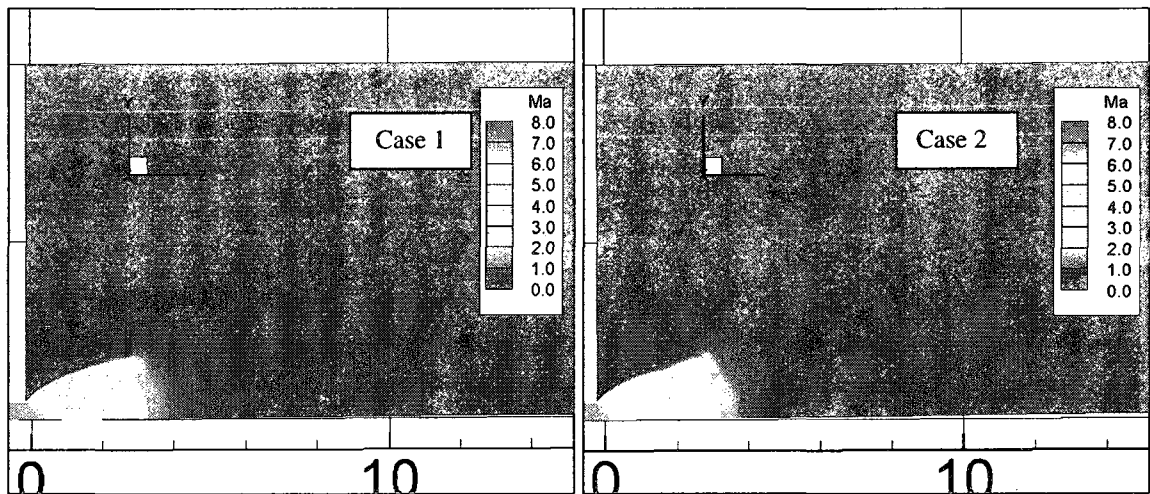


Fig. 6.13 Mach contours ($t = 20.09 \mu s$).

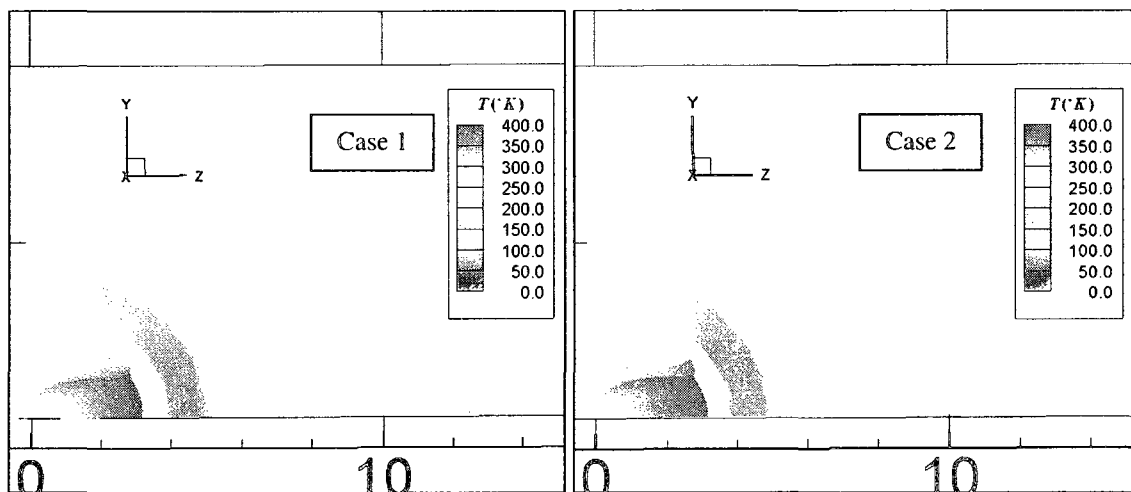


Fig. 6.14 Temperature contours ($t = 20.09 \mu s$).

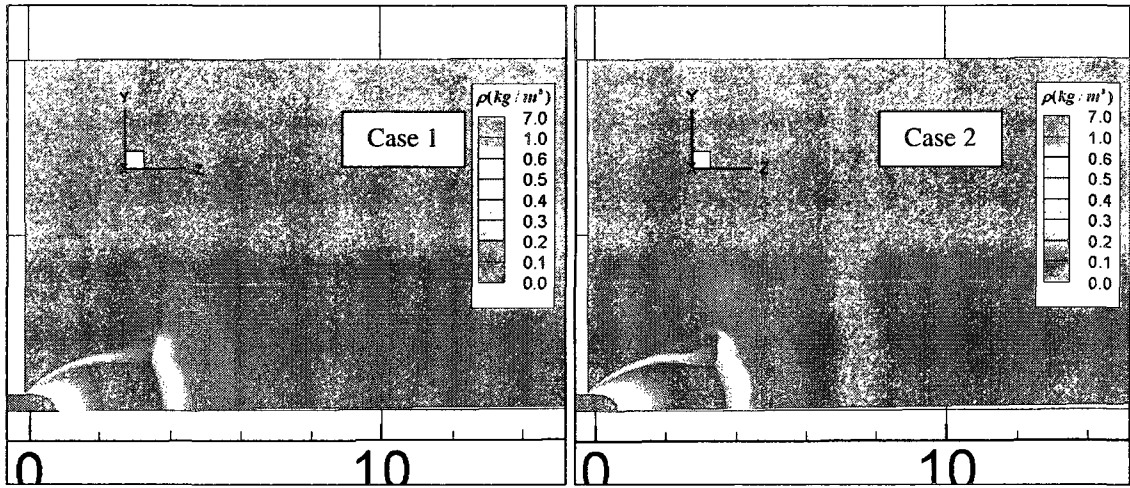


Fig. 6.15 Density contours for $0.0 \leq \rho \leq 1$ ($t = 25.15 \mu s$).

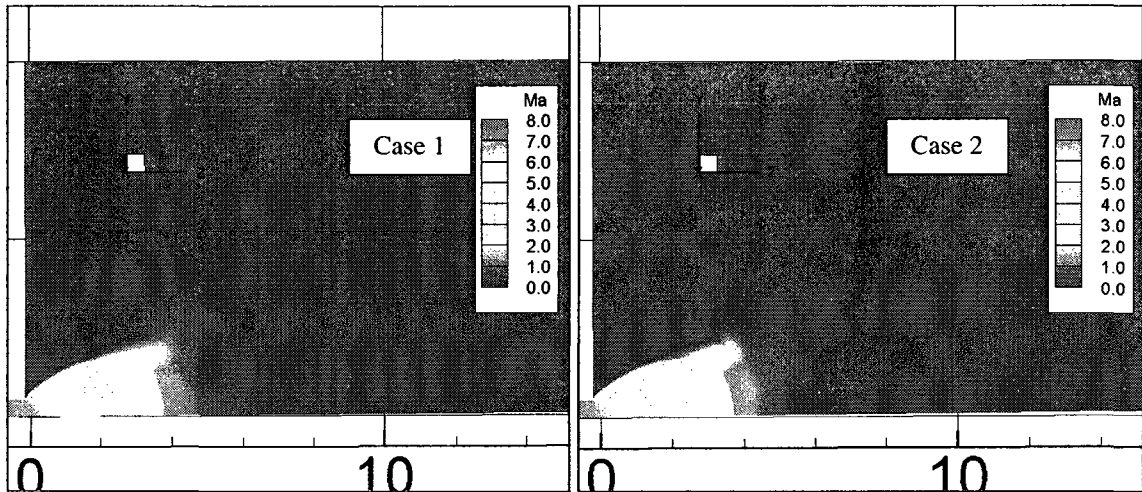


Fig. 6.16 Mach contours ($t = 25.15 \mu s$).

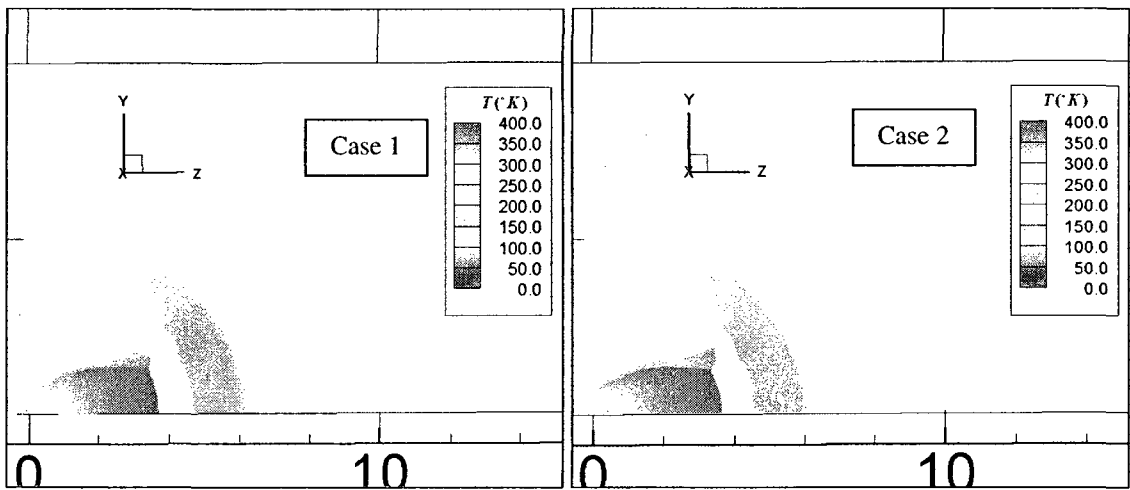


Fig. 6.17 Temperature contours ($t = 25.15 \mu s$).

Fig. 6.20 Temperature contours ($t = 30.21\mu s$).

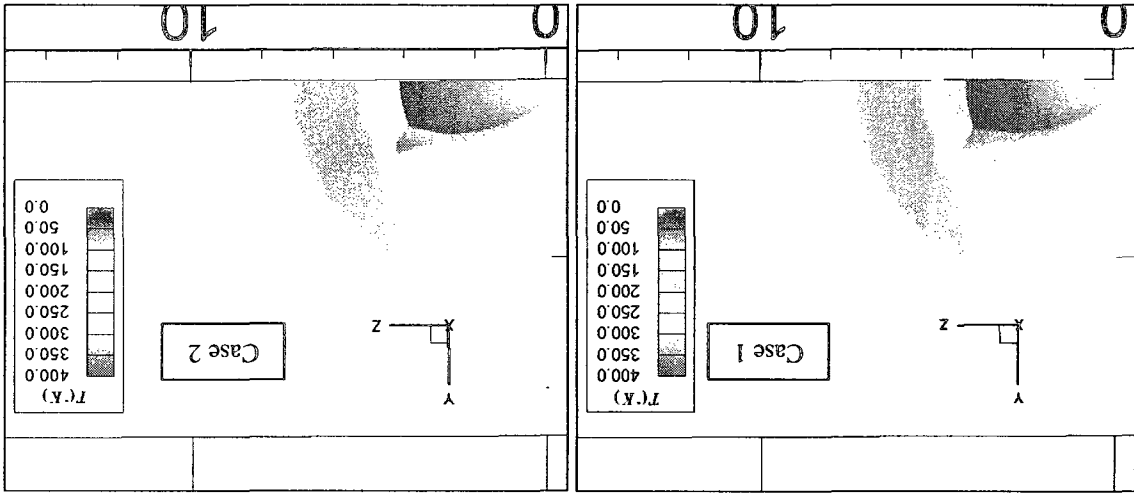


Fig. 6.19 Mach contours ($t = 30.21\mu s$).

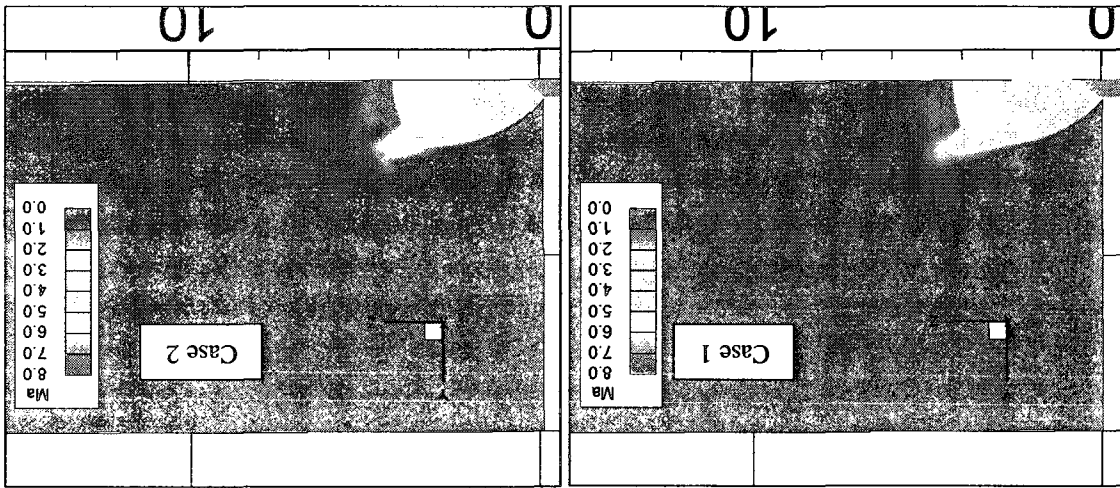
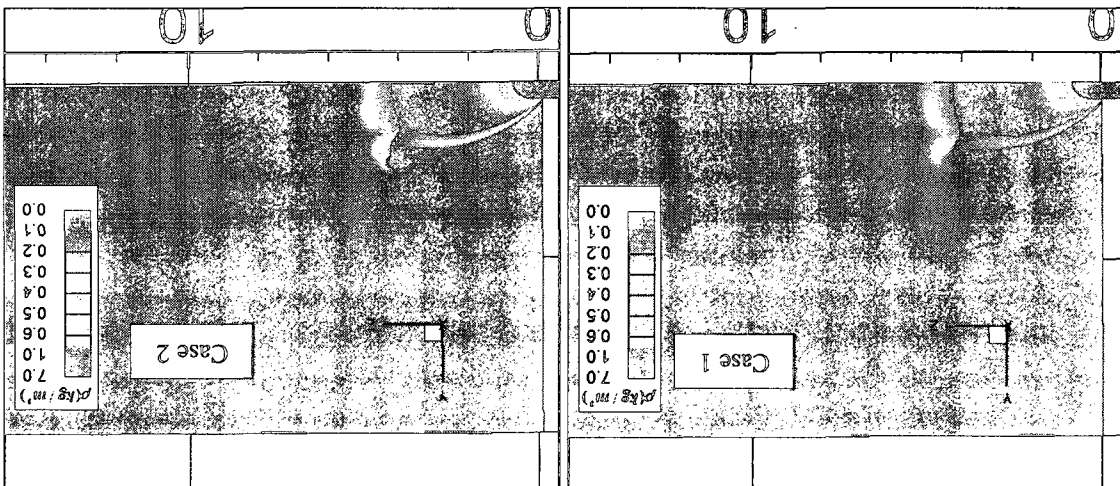


Fig. 6.18 Density contours for $0.0 \leq \rho \leq 1$ ($t = 30.21\mu s$).



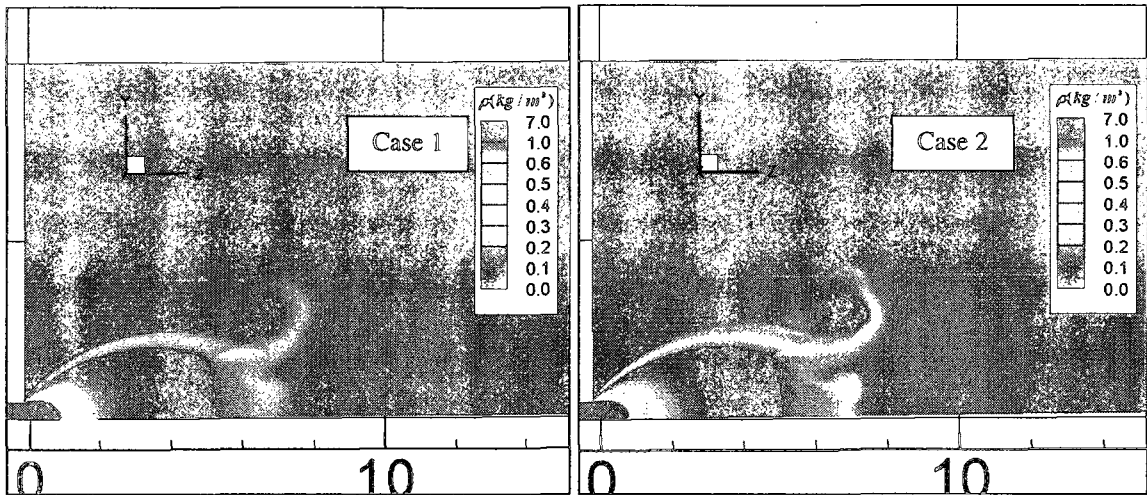


Fig. 6.21 Density contours for $0.0 \leq \rho \leq 1$ ($t = 55.34 \mu\text{s}$).

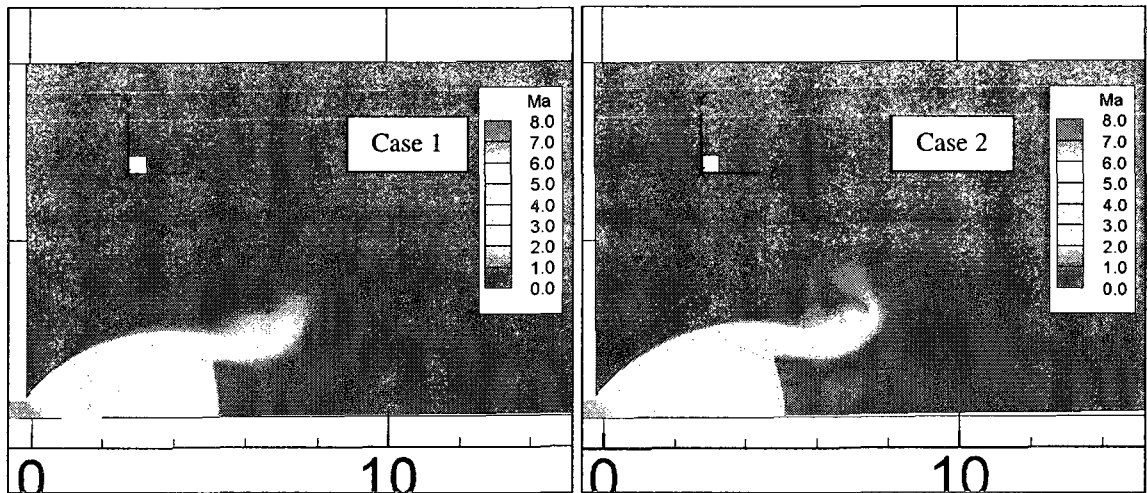


Fig. 6.22 Mach contours ($t = 55.34 \mu\text{s}$).

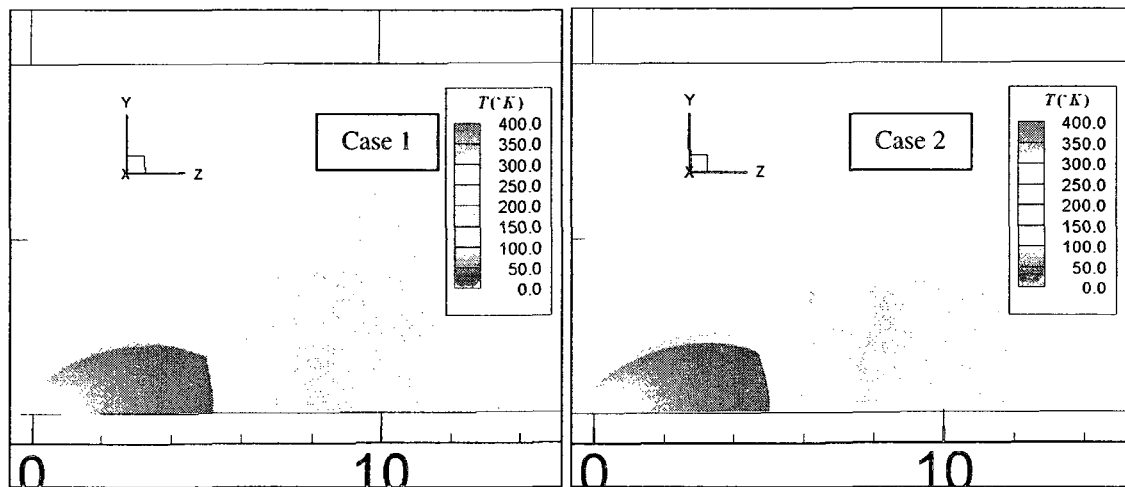


Fig. 6.23 Temperature contours ($t = 55.34 \mu\text{s}$).

Fig. 6.26 Temperature contours ($t = 75.98 \mu s$).

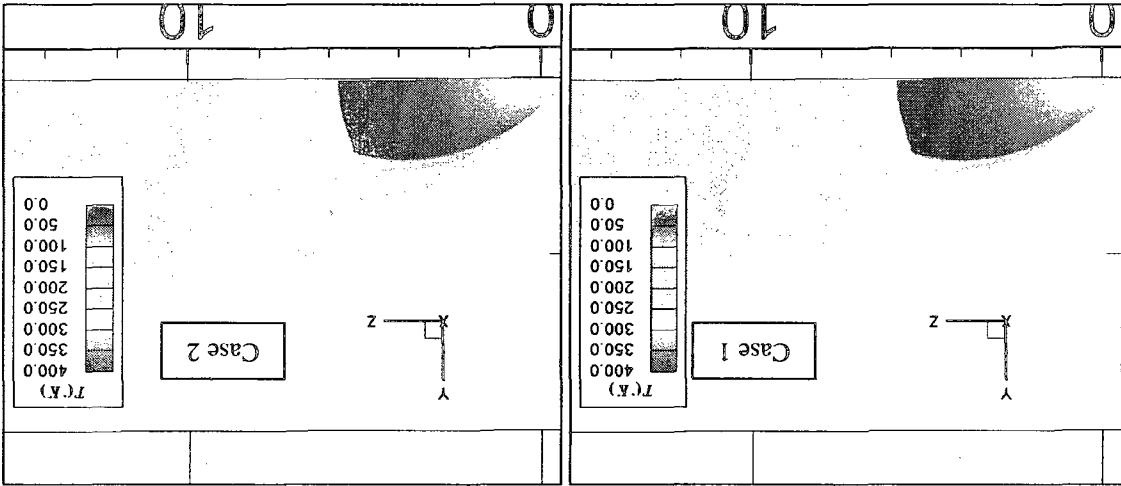


Fig. 6.25 Mach contours ($t = 75.98 \mu s$).

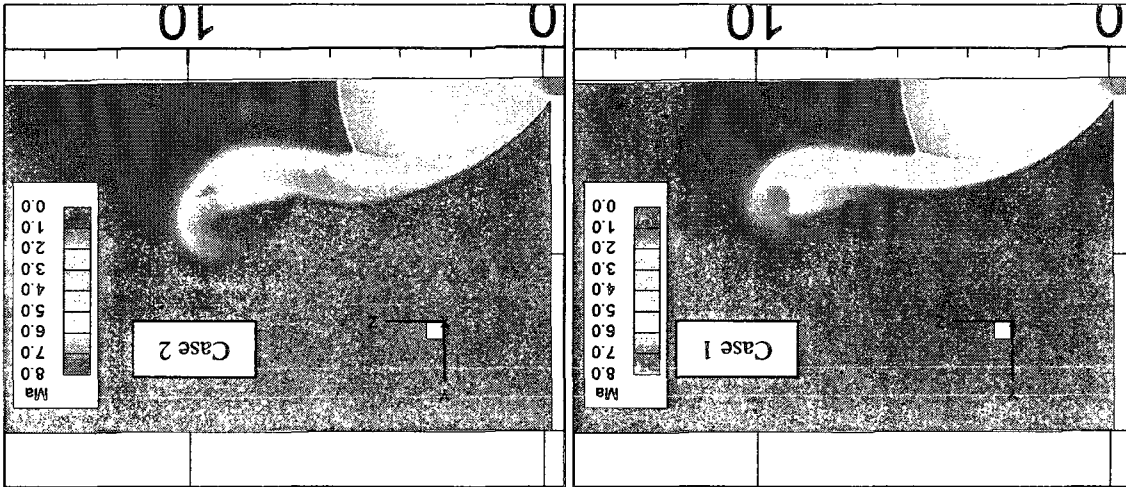
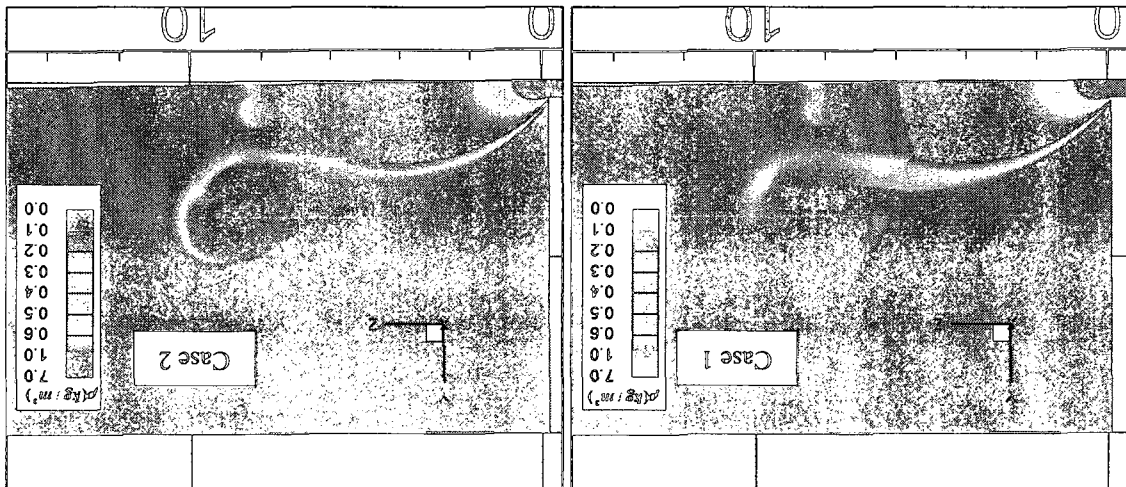


Fig. 6.24 Density contours for $0.0 \leq p \leq 1$ ($t = 75.98 \mu s$).



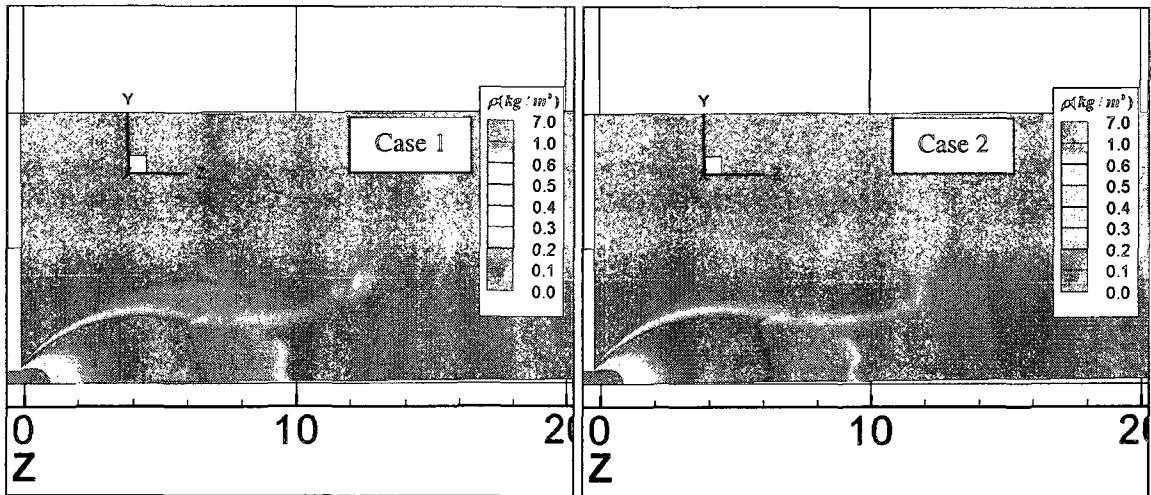


Fig. 6.27 Density contours for $0.0 \leq \rho \leq 1$ ($t = 94.98 \mu s$).

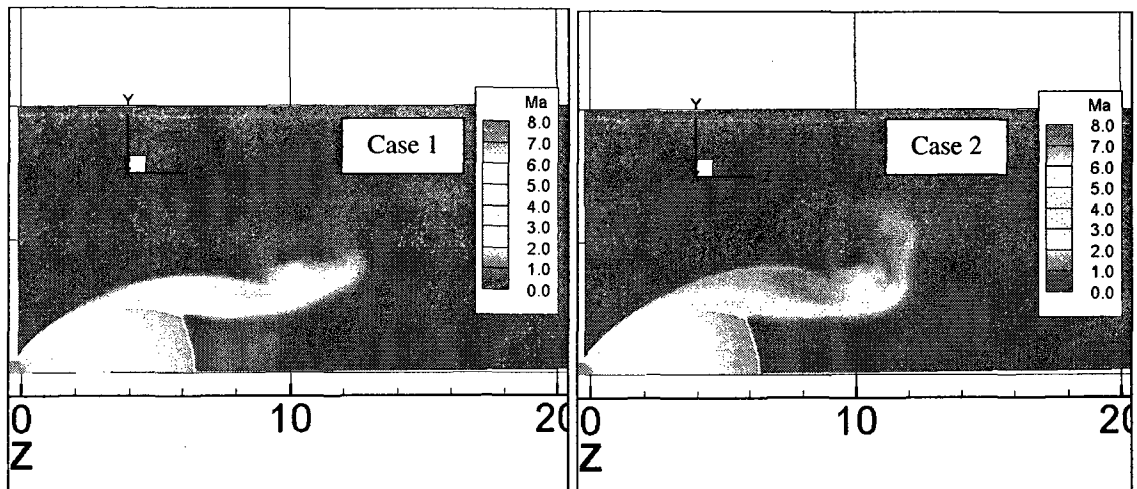


Fig. 6.28 Mach contours ($t = 94.98 \mu s$).

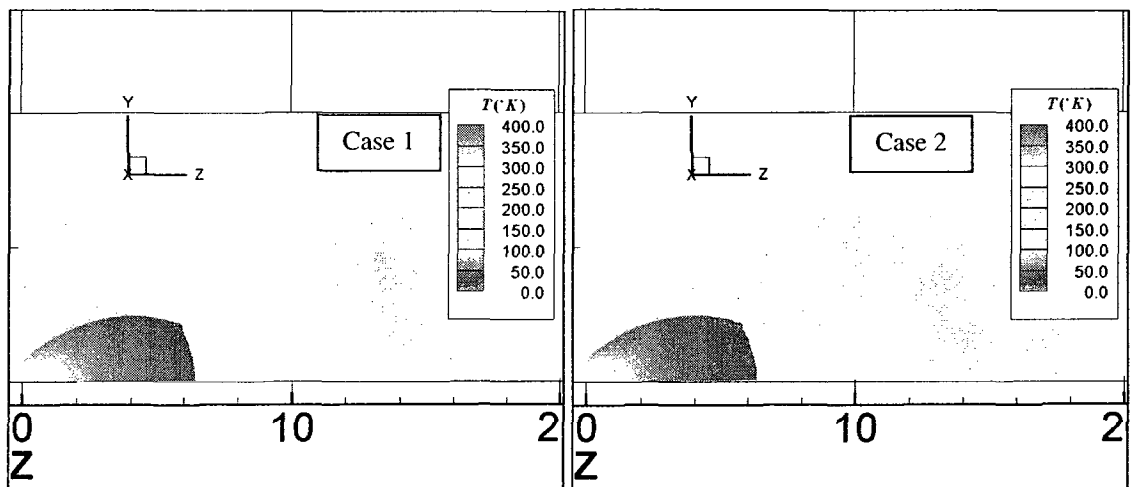


Fig. 6.29 Temperature contours ($t = 94.98 \mu s$).

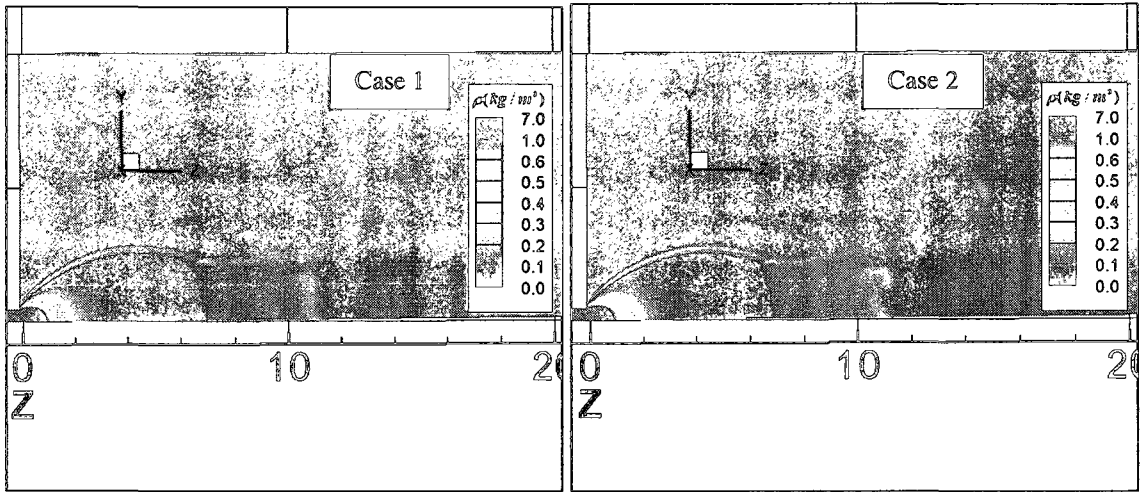


Fig. 6.30 Density contours for $0.0 \leq \rho \leq 1$ ($t = 113.96 \mu s$).

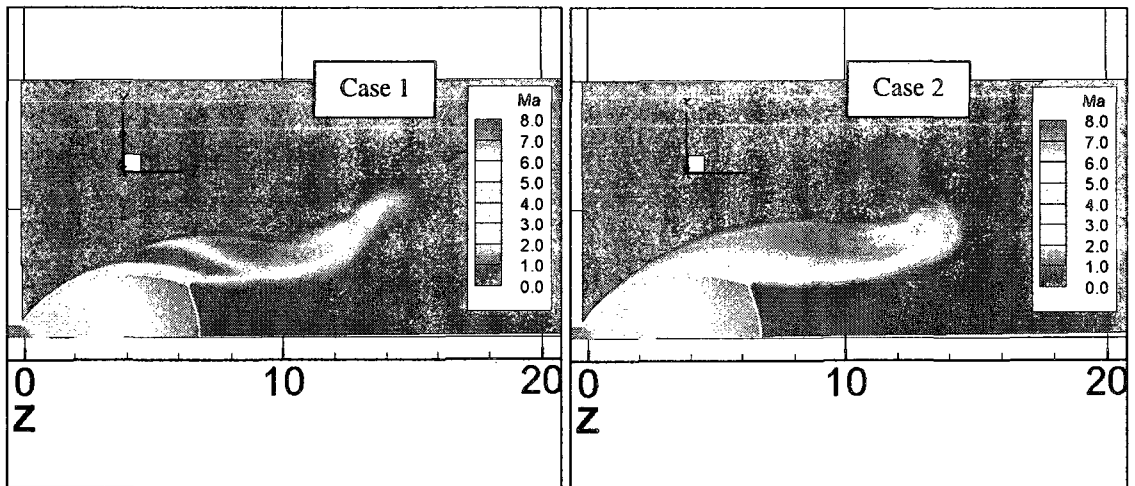


Fig. 6.31 Mach contours ($t = 113.96 \mu s$).

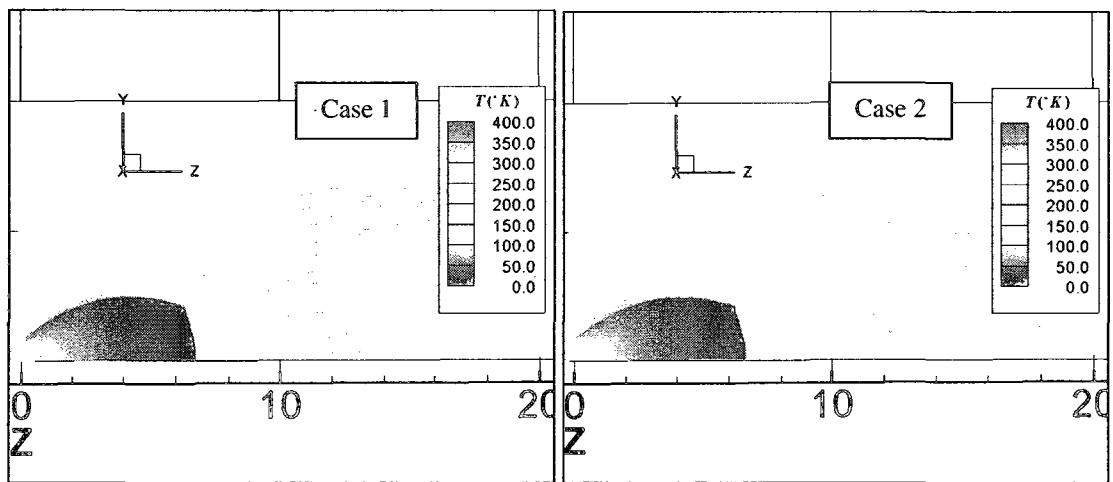


Fig. 6.32 Temperature contours ($t = 113.96 \mu s$).

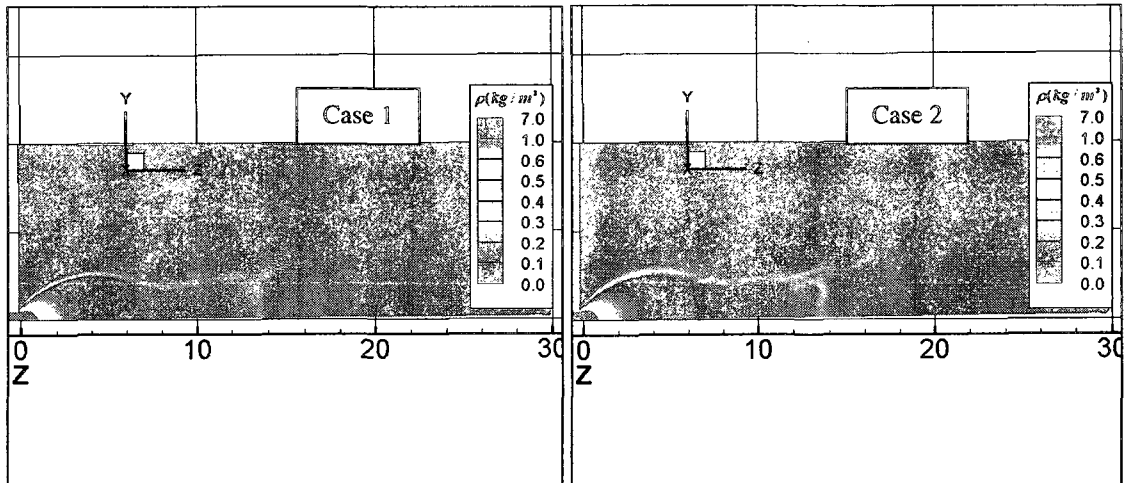


Fig. 6.33 Density contours for $0.0 \leq \rho \leq 1$ ($t = 151.96 \mu s$).

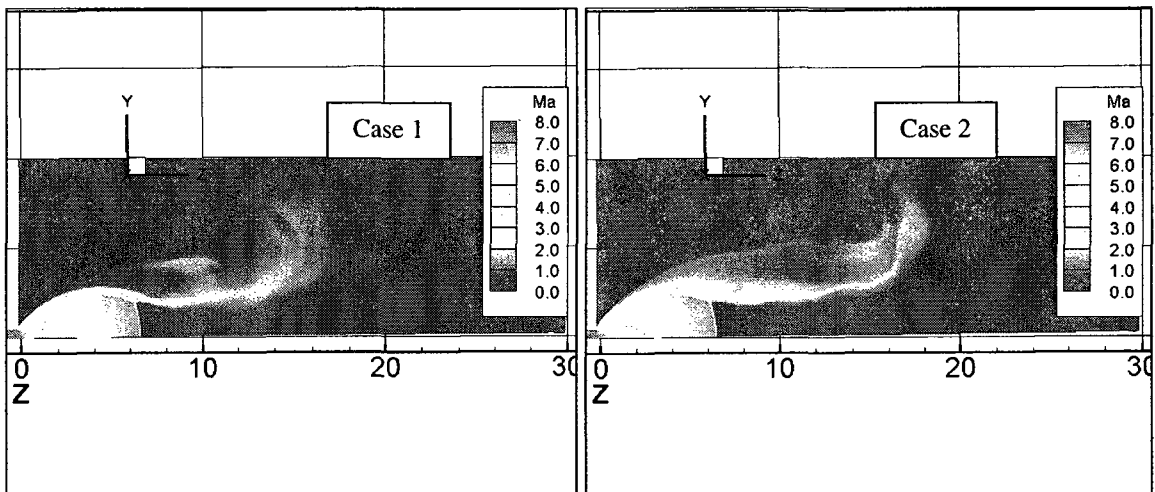


Fig. 6.34 Mach contours ($t = 151.96 \mu s$).

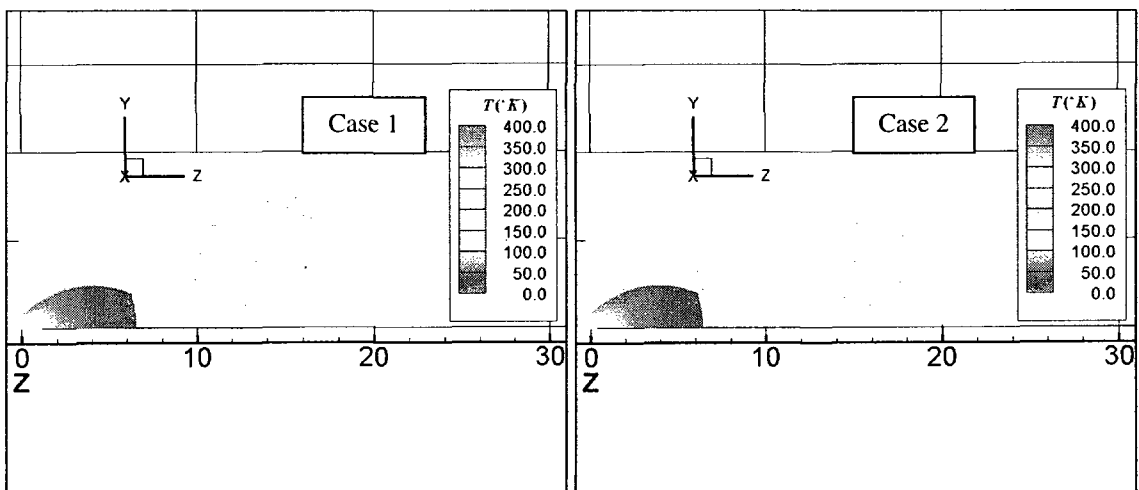


Fig. 6.35 Temperature contours ($t = 151.96 \mu s$).

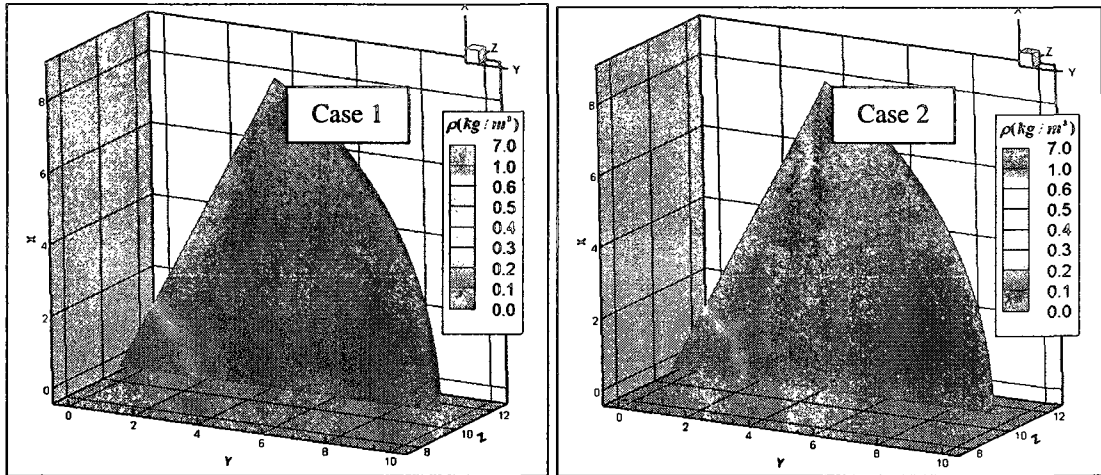


Fig. 6.36 Density contours for $0.0 \leq \rho \leq 1$ and $Z/D = 10$ ($t = 151.96 \mu s$).

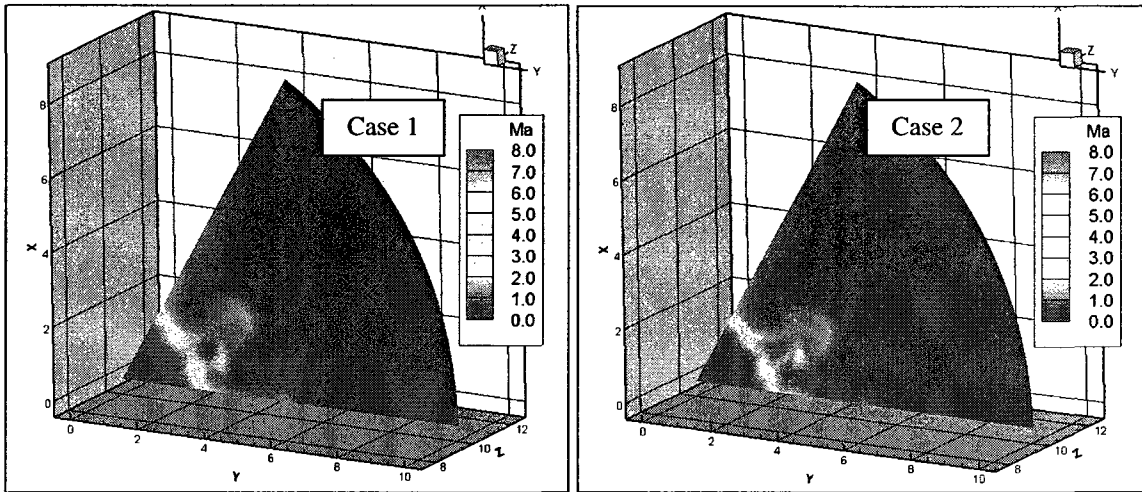


Fig. 6.37 Mach contours at $Z/D = 10$ ($t = 151.96 \mu s$).

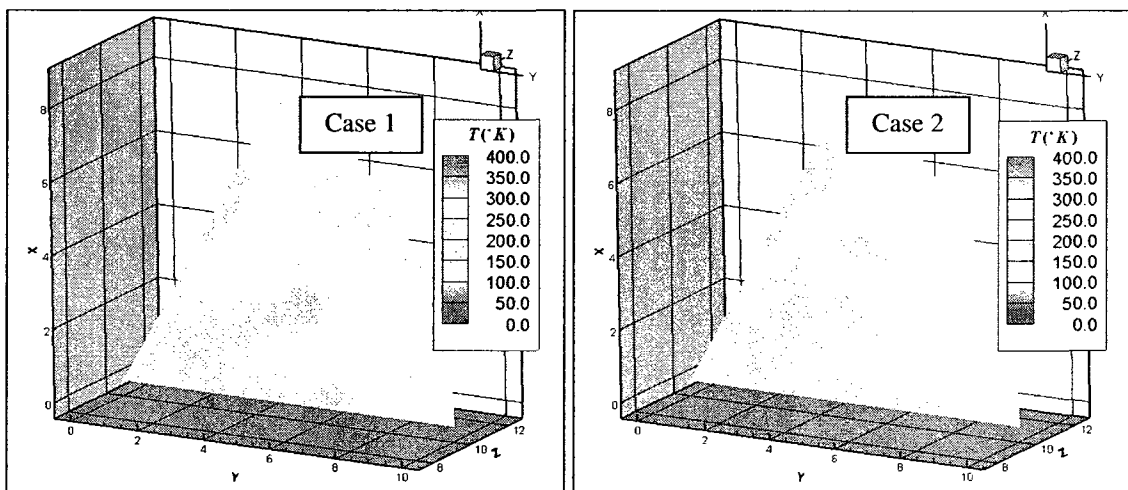


Fig. 6.38 Temperature contours at $Z/D = 10$ ($t = 151.96 \mu s$).

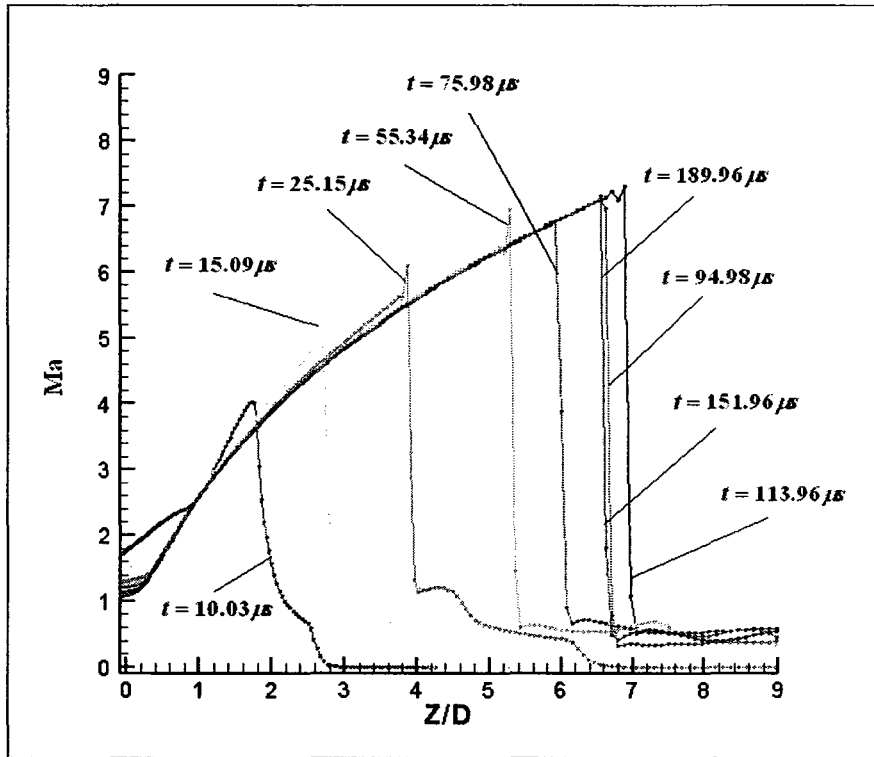


Fig. 6.39 Mach distribution along the centerline (Case 1).

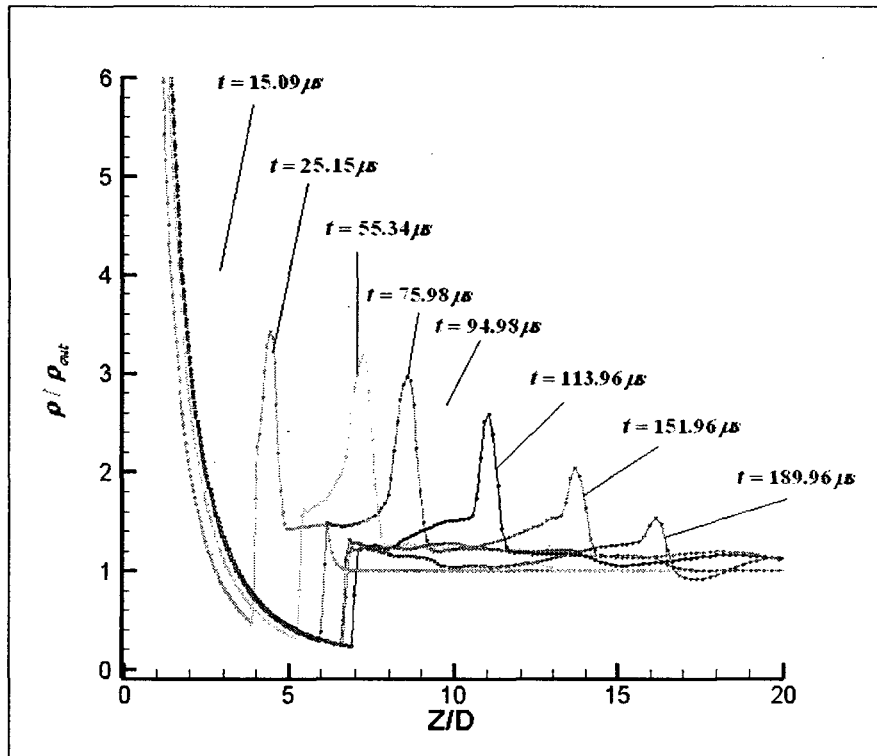


Fig. 6.40 Density distribution along the centerline (Case 1).

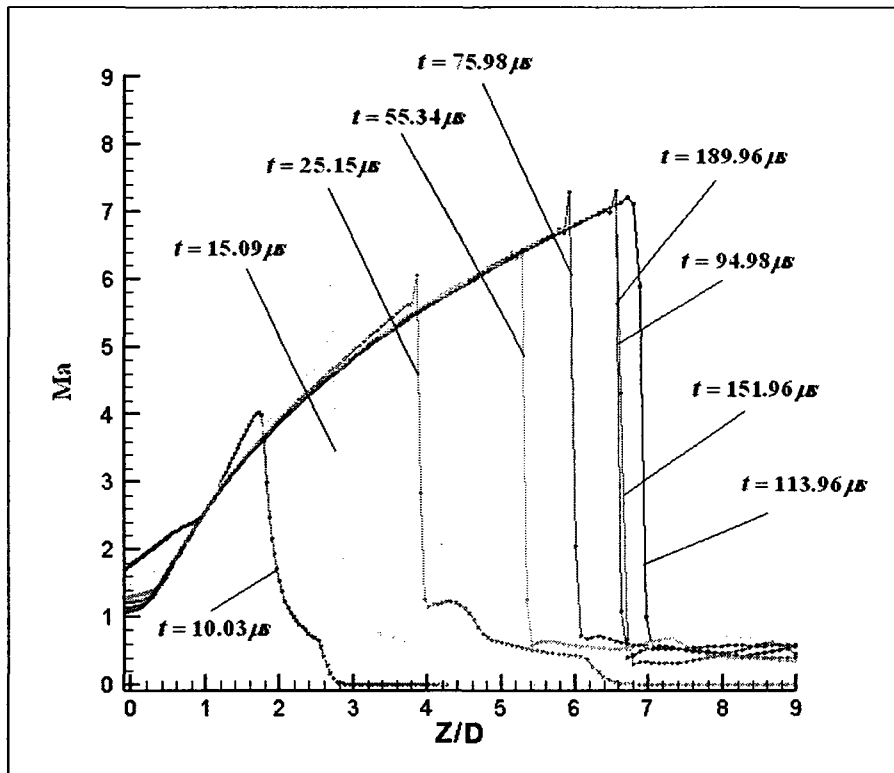


Fig. 6.41 Mach distribution along the center line(Case 2).

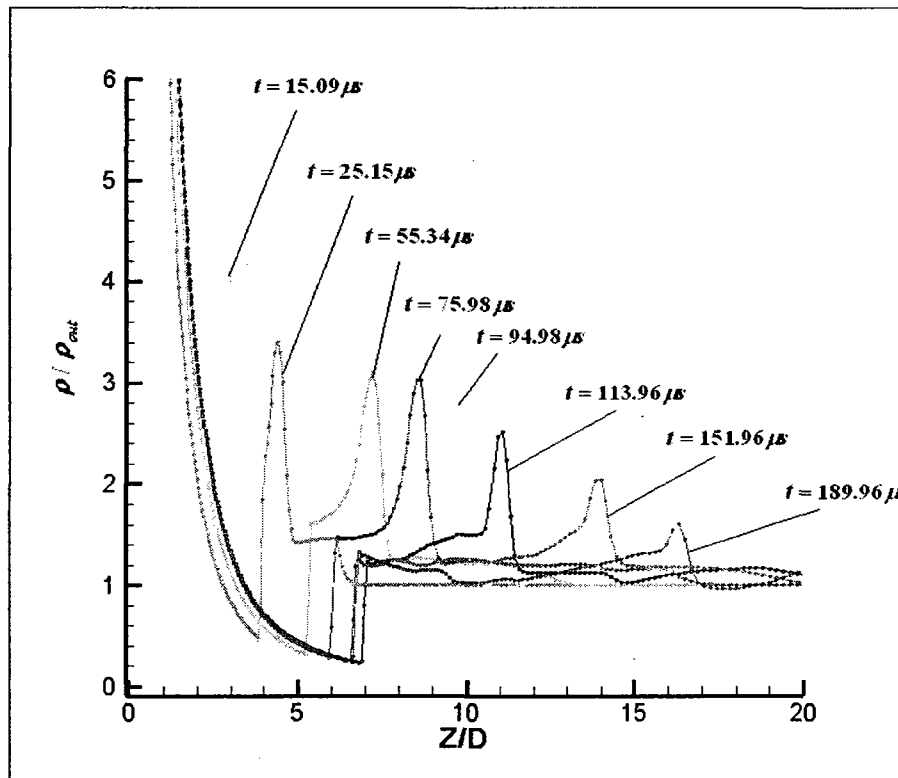


Fig. 6.42 Density distribution along the centerline (Case 2).

Crist et al. (1966),¹⁶ have done a series of experiments about the underexpanded sonic jets for Nitrogen, Argon, Helium, CO_2 and Freon 22. It was found that Mach disk location is insensitive to the ratio of specific heat, condensation, solid boundary geometry and the nozzle tip and absolute pressure level. In their experiment, two different nozzle lip geometries were used with no resultant change in the Mach disk location. According to their results, the Mach disk's location for the pressure ratio equal to 100 is approximately 7 which is very close to our numerical result and the relative error is about 4%.

The distribution of density along the centerline for different computational times is shown in Figs. (6.40,6.42). As it is shown in these figures, a local bump exists in front of the Mach disk which moves downstream. The Mach disk gradually decelerates and stops at $Z/D = 6.7$ but the bump continues its motion. According to Fig. 1.4, this bump represents the 2nd shock wave even though it is not appearing as a real shock in Figs. (6.39,6.41).

Based on the obtained results we can conclude that development of hydrogen underexpanded jet at the region behind the Mach disk is less sensitive than the free jet to the subgrid model or the numerical upwinding. These parameters, however, become very influential after the Mach disk and directly affect the formation of the 2nd vortices.

6.2.1 Interaction of the Limiter Function and the Upwinding Term

In Figs. 6.43 to 6.47, the behavior of limiter coefficients for different primitive variables in cases 1 and 2 are shown. When the limiter coefficient of a primitive variable is locally close to zero, first order spatial approximation is used. This is the case at shocks or turbulent regions. On the other hand, when the limiter coefficient is close to one, a second order approximation is applied. It takes place mostly away from major discontinuities (shocks) or regions with high turbulence.

The limiter coefficient for case 1 appears to be higher than for case 2 as a result of full upwinding's smoothing effects. Lowering the scheme's upwinding in case 2 by applying the self-adaptive upwinding method results in more fluctuations in the flow field which further activates the limiter function. The effect of the limiter function's excessive activation on the numerical diffusion is compensated by the decrease in the scheme's upwinding. Therefore in case 2 the numerical scheme is less dissipative and large scale eddies are better captured (Figs. 6.43-6.47).

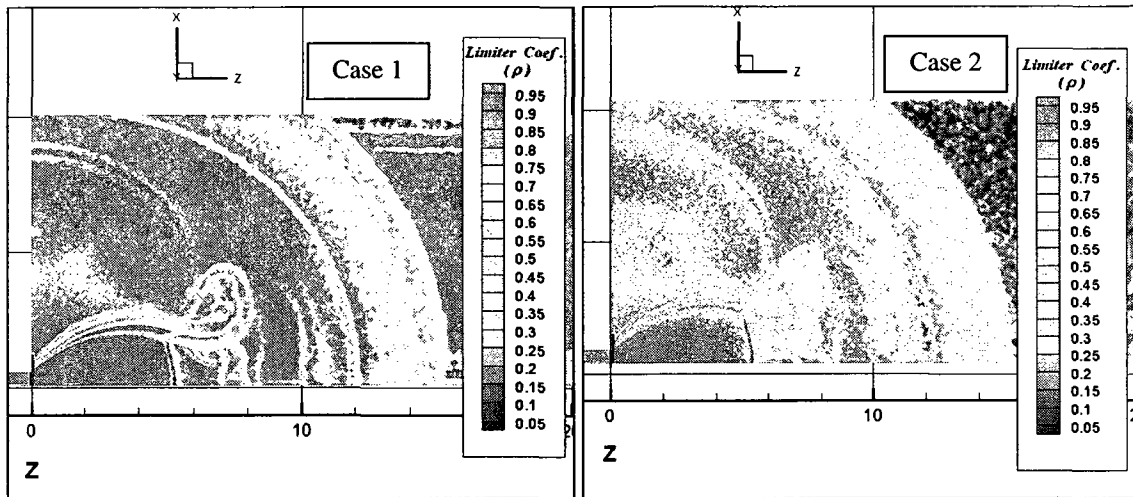


Fig. 6.43 Limiter coefficient for density ($t = 55.34 \mu s$).

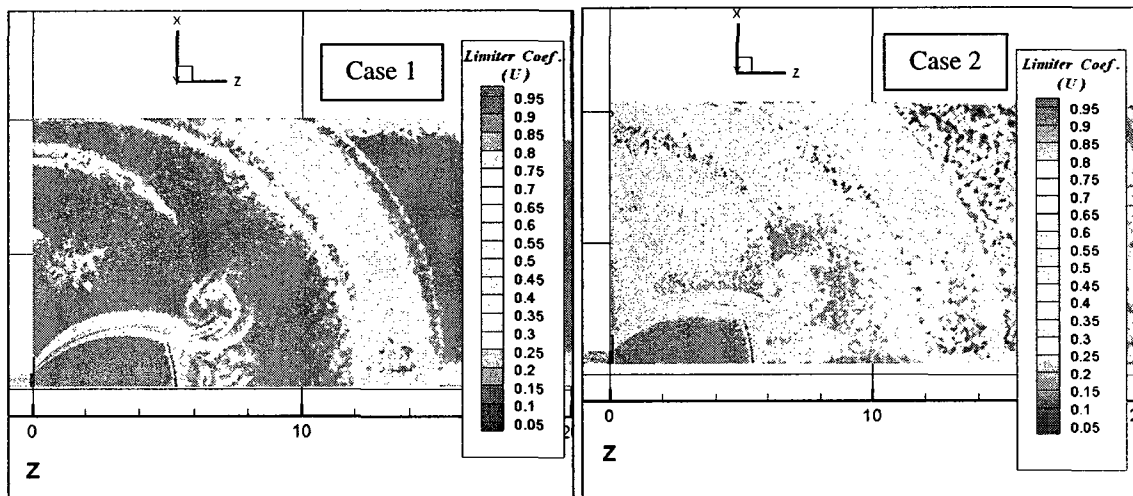


Fig. 6.44 Limiter coefficient for velocity in the x -direction ($t = 55.34 \mu s$).

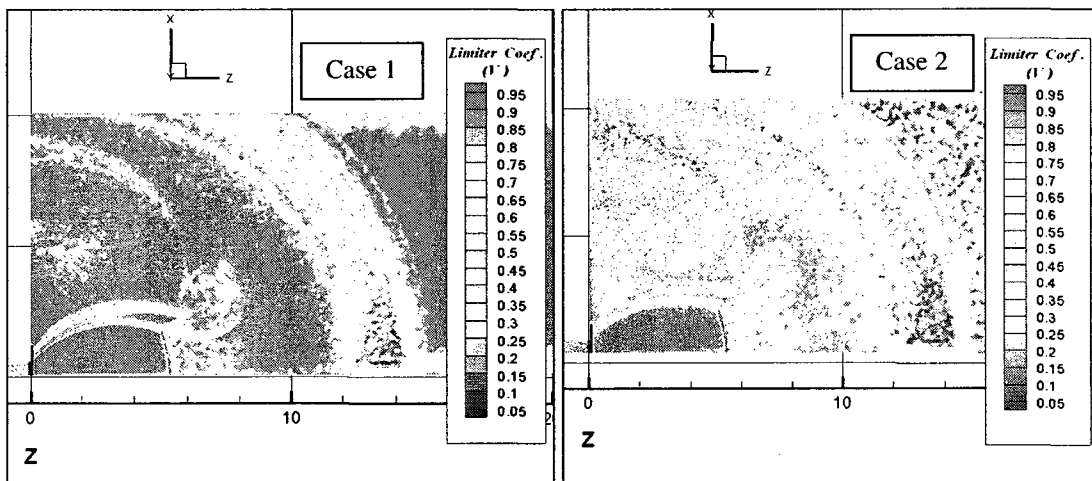


Fig. 6.45 Limiter coefficient for velocity in the y -direction ($t = 55.34 \mu s$).

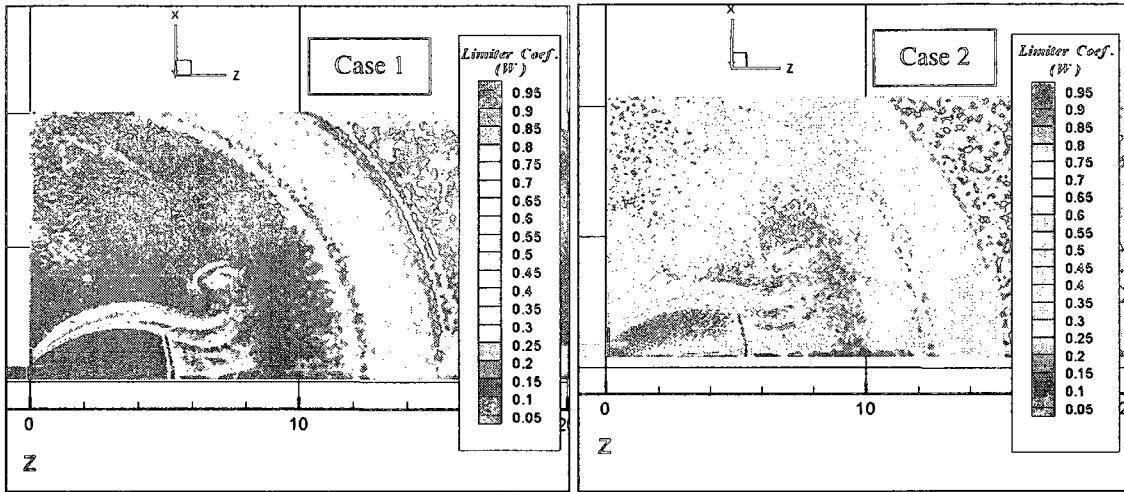


Fig. 6.46 Limiter coefficient for velocity in the z-direction ($t = 55.34\mu\text{s}$).

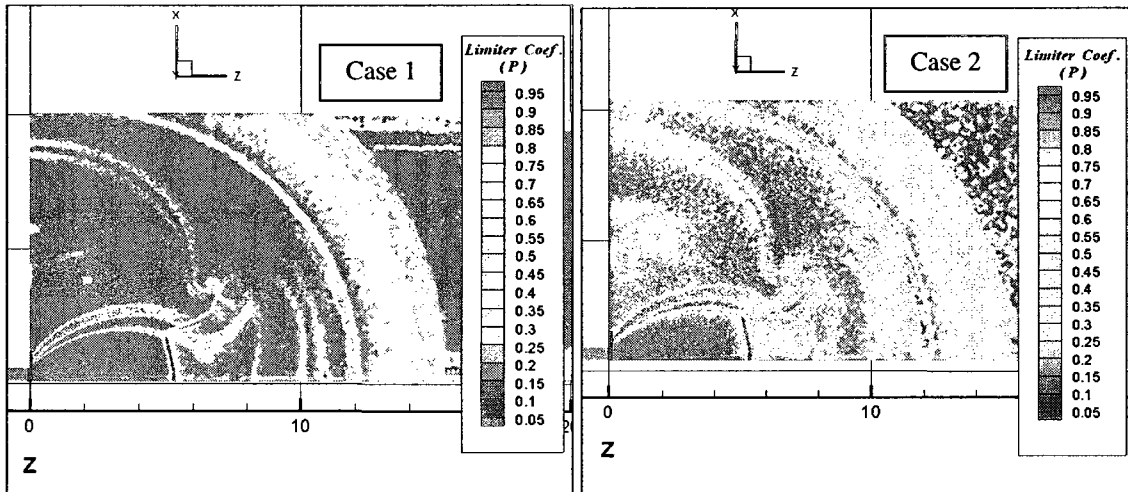


Fig. 6.47 Limiter coefficient for pressure ($t = 55.34\mu\text{s}$).

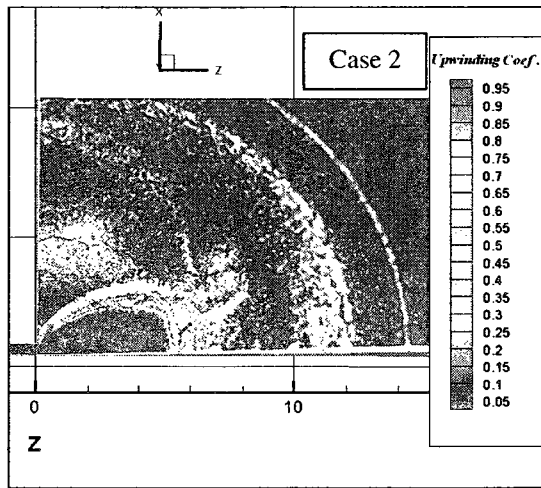


Fig. 6.48 Upwinding parameter ($t = 55.34\mu\text{s}$).

It is also shown that in case 2, the limiter function provides a 1st order spatial approximation scheme at regions far from the jet's inlet. This is because the upwinding coefficient at those regions has been significantly decreased by the self-adaptive upwinding method.

In case 2 there is a thin layer attached to the domain's boundaries where the full-upwinding scheme is applied (Fig. 6.48). There is also a region at the jet's inlet (Figs. 6.43-6.47) where the first order approximation and the full upwinding scheme are imposed to provide the necessary stability and prohibit undesirable fluctuations.

Chapter 7

Conclusions and Future Works

A self-adaptive upwinding method for unstructured finite-volume flow solver was introduced and validated. The scheme tries to regulate the numerical dissipation by adjusting the upwinding term through a sensor that locally detects the intensity of wiggles in the flow variables. It was firstly used in a channel flow simulation to test its stability. It showed very good stability characteristic even when the noise coefficient was very high. Secondly isotropic turbulence was considered. The original scheme appeared to be over-dissipative, preventing SGS model from producing a proper LES solution. The self-adaptive upwinding method, however, improved the decaying behavior of total kinetic energy in time and also slope of the energy spectrum. The wiggle detector made it possible to adjust the amount of energy in the highest modes and therefore improved the results. That adjustment, however, influenced the energy distribution on the entire spectrum and showed some undesirable effects in the lower modes.

The developed numerical tool was then used to simulate a compressible turbulent free jet at $Re_D = 0.66 \times 10^6$ and $Ma_j = 0.95$. The overall physics of the flow such as formation of the potential core, development of the annular mixing layer, gradual generation of Kelvin-Helmholtz instabilities, formation of the transient region with rapid mixing characteristics and also the fully-developed region after the potential region were successfully captured. There were however some discrepancies between the measured data and the results of the simulation, especially at the density fluctuating profile along the jet's axis. In overall the results were acceptable and very promising and it encourages us to implement the method for more complicated flows. It was observed that the length of the potential core predicted by the computation

was slightly less than the value that was measured experimentally. It indicates a rapid development of the annular mixing layer which also results in a fast decay of the mean velocity.

The simulation showed a great dependence on the strength of the applied subgrid model which could be a result of applying a low order numerical method or lack of having the required fine grid resolution. It could also emphasize on the need for applying a more suitable subgrid model considering our special configuration. The values recommended for the coefficient of Smagorinsky subgrid model in the literature have been mainly devised based on the analysis of isotropic decaying turbulence. The flow of a free jet however is highly anisotropic and also under-developed at the regions close to jet's inlet therefore a more suitable subgrid model is necessary.

Finally a hydrogen jet releasing from a high pressure reservoir at 100 atm into a stagnant hydrogen medium at atmospheric pressure was simulated. This simulation was carried out to study the formation of complex shocks generated in different forms at the early stages of the gas release from the reservoir. The self-adaptive method was found to give a much more realistic emulation of the flow and encouraged us to further apply it for supersonic flows. Based on my simulations, the following conclusions are made:

- Decaying isotropic turbulence tests showed that the overall dissipation of the simulation is affected by the contribution of both the subgrid model and the upwinding term;
- Validation tests demonstrated that the upwinding term contributes to the overall dissipation of the scheme to such extent that it makes the original scheme over-dissipative and prevents the SGS model from producing a proper LES solution;
- It was shown in the channel flow stability test that the self-adaptive upwinding scheme is a robust scheme and is able to stabilize the simulation at the presence of strong gradients;
- Effective adjustment of the numerical dissipation is achievable by using the adaptive upwinding method and it can positively affect the energy spectrum's slope;
- The proposed method was successfully able to predict many different features of compressible turbulent free jet (potential core, annular mixing layer, and etc.);

- There was no need for artificial forcing turbulent fluctuations at the inlet in order to initiate the necessary instabilities inside the shear layer. It could be a result of applying an unstructured grid in our simulation;
- In general, density has been predicted more accurately than velocity by the simulation. One of the reasons for discrepancies in the velocity profiles could be the strong effect of co-flow in our simulation. That influence however is not noticeable in the experimental results;
- The length of the potential core was slightly under-predicted;
- Application of a too coarse grid could be the cause of shorter potential core. The annular mixing has not been represented correctly which results in rapid thickening of the shear layer and consequently sooner destruction of the potential core;
- The value required for the Smagorinsky subgrid model's coefficient in the free jet simulation was higher than the isotropic decaying turbulence simulation. This could show the need for development and application of subgrid models which are suitable for anisotropic flows;
- The self-adaptive scheme was more successful than the full upwinding method in simulating the highly under-expanded hydrogen jet releasing from a high pressure reservoir at 100 atm. It could very well generate different features of this flow such as jet boundary, Mach disk, barrel shock, 2nd vortices, slip line, reflected shock, 1st vortex, 1st shock and 2nd shock;
- It also accurately predicted the location of the Mach disk.

The proposed scheme has also been used to simulate the flow separation phenomenon over a NACA0025 profile at angles of attack equal to 0 and 5 degrees. The results of that simulation were not included in this dissertation but were reported in Ref. 106. The original flux calculation scheme appeared to be over dissipative, preventing the flow to separate over the airfoil. The self-adaptive upwinding method reduced the artificial diffusion to the level of flow instability and made it possible for the separation to occur. The proposed scheme produced results which were comparable to experimental data and also more accurate and reliable than results obtained by FLUENT. It was despite the fact that the grid used for FLUENT was much finer than the one applied for the in-house code. In that simulation separation took place only when the subgrid model had a relatively small contribution.

As for the future works, application of more accurate turbulence models seems to be very essential specially when the flow field is highly anisotropic as it the case for free jets. Given that in the LES for engineering applications, the required computational resources are always an issue of concern, application of adaptive grid schemes or hybrid grid generation methods could appreciably improve the accuracy and therefore decrease the required computational resources. This issue is more dominant when there are solid walls included into the computational domain. The turbulent structures near the solid walls have very small dimensions and therefore capturing a reasonable portion of these structures in the LES would require relatively refined mesh which is still out of reach for the current supercomputers. This fact further signifies the need for developing more accurate numerical schemes and also applying hybrid grid generation or grid adaptation methods.

References

- [1] Chuang, S. H., Hong, Z. C., Wang, J. H., "The Application of Turbulent Kinetic Theory to a Reacting Flow of Turbulent Plane Jet," *International Journal of Numerical Methods for Heat & Fluid Flow*, Vol. 8(2), 1998, pp. 153-168.
- [2] James, S., Jaber, F. A., "Large Scale Simulations of Two-Dimensional Nonpremixed Methane Jet Flames," *Combustion and Flames journal*, Vol: 123, 2000, pp. 465-487.
- [3] Majander, P., Siikonen, T., "Large Eddy Simulation of a Round Jet in a Cross-flow," *International Journal of Heat and Fluid Flow*, Vol. 27, 2006, pp.402-415.
- [4] Tkatchenko, I., Kornev, N., Jahnke, S., "Performance of LES and RANS Models for Simulation of Complex Flows in a Coaxial Jet Mixer," *Flow Turbulence Combustions*, Vol. 78, 2007, pp.111-127.
- [5] Jahnke, S., Kornev, N., Tkatchenko, I., Hassel, E., "Numerical Study of Influence of Different Parameters on Mixing in a Coaxial Jet Mixer Using LES," *Heat Mass Transfer*, Vol. 41, 2005, pp.471-481.
- [6] Andersson, N., Eriksson, L. E., Davidson, L., "Large-Eddy Simulation of Subsonic Turbulent Jets and Their Radiated Sound," *AIAA Journal*, Vol. 43, 2005, pp. 1899-1912.
- [7] Uzun, A., Blaisdell, G. A., Lyrintzis, A. S., "Application of Compact Schemes to Large eddy Simulation of Turbulent Jets," *Journal of Scientific Computing*, Vol. 21(3), 2004, pp.283-319.
- [8] Berland, J., Bogey, C., Bailly, C., "Large eddy Simulation of Screech Tone Generation in a Planer Underexpanded Jet," 12th *AIAA/CEAS Aeroacoustics Conference*, School of Aeronautics and Astronautics, Laboratoire de Mécanique des Fluides et d'Acoustique, Ecole Centrale de Lyon & UMR CNRS 5509, Ecully, France, 2006.
- [9] Bodony, D. J., "The Prediction and Understanding of Jet Noise," Center for Turbulence Research, Annual Research Brief, USA, 2005.

- [10] Lighthill, M. J., "On Sound Generated Aerodynamically I. General Theory," *Proceedings of the Royal Society of London. Series A., Mathematical and Physical Sciences*, Department of Mathematics, University of Manchester, UK. Vol. 211, 1952, pp.564-587.
- [11] Lighthill, M. J., "On Sound Generated Aerodynamically II. Turbulence as a Source of Sound," *Proceedings of the Royal Society of London. Series A., Mathematical and Physical Sciences*, Department of Mathematics, University of Manchester, UK. Vol. 222, 1954, pp.1-32.
- [12] Ciardi, M., Sagaut, P., Klein, M., Dawes, W. N., "A Dynamic Finite Volume Scheme for Large-Eddy Simulation on Unstructured Grids," *J. of Comp. Physics*, Vol. 210, 2005, pp. 632-655.
- [13] Camarri, S., Salvetti, M. V., Koobus, B., Dervieux, A., "A Low-Diffusion MUSCL Scheme for LES on Unstructured Grids," *Journal of Computers and Fluids*, Vol. 33, 2004, pp.1101-1129.
- [14] Donaldson, C. D., Gray, K. E., "Theoretical and Experimental Investigation of the Compressible Free Mixing of Two Dissimilar Gases," *AIAA Journal*, Vol. 4(11), 1966, pp. 2017-2025.
- [15] O'connor, T. J., Comfrot, E. H., Cass, L. A., "Turbulent Mixing of an Axisymmetric Jet of Partially Dissociated Nitrogen with Ambient Air," *AIAA Journal*, Vol. 4(11), 1966, pp. 2026-2032.
- [16] Crist, S., Sherman, P. M., Glass, D. R., "Study of the Highly Underexpanded Sonic Jet," *AIAA Journal*, Vol. 4, 1966, pp. 68-71.
- [17] Gamet, L., Estivalezes, J. L., "Application of Large-Eddy Simulations and Kirchhoff Method to Jet Noise Prediction," *AIAA Journal*, Vol. 36(12), 1998, pp. 2170-2178.
- [18] Zhao, W., Frankel, S. H., Mongeau, L., "Large Eddy Simulation of Sound Radiation from Subsonic Turbulent Jets," *AIAA Journal*, Vol. 39(8), 2001, pp. 1469-1477.
- [19] Freund, J. B., "Noise Sources in a Low-Reynolds-Number Turbulent Jet at Mach 0.9," *J. Fluid Mechanics*, Vol.438, 2001, pp.277-305.

- [20] DeBonis, J. R., Scott, J. N., "Large-Eddy Simulation of a Turbulent Compressible Round Jet," *AIAA Journal*, Vol. 40(7), 2002, pp. 1346-1354.
- [21] Andersson, N., Eriksson, L. E., Davidson, L., "Large-Eddy Simulation of a Mach 0.75 Jet," 9th *AIAA/CEAS Aeroacoustics Conference*, Department of Applied Mechanics, Chalmers University of Technology, Goterborg, Sweden, 2003.
- [22] Andersson, N., Eriksson, L.-E., Davidson, L., "Investigation of an Isothermal Mach 0.75 Jet and Its Radiated Sound Using Large-Eddy Simulation and Krichhoff Surface Integration," *International Journal of Numerical Methods for Heat & Fluid Flow*, Vol. 26, 2005, pp. 393, 410.
- [23] Sagaut, P., Garnier, E., Tromeur, E., Larcheveque, E. L., Labourasse, "Turbulent Inflow Conditions for Large Eddy Simulation of Supersonic and Subsonic Wall Bounded Flows," 41st *Aerospace Sciences Meeting and Exhibit, Aeroacoustics Conference*, Universite Pierre et Marie Curie, Paris, France, 2003.
- [24] Andersson, N., Eriksson, L. E., Davidson, L., "Effects of Inflow Conditions and Subgrid Model on LES for Turbulent Jets", 11th *AIAA/CEAS Aeroacoustics Conference*, Department of Applied Mechanics, Chalmers University of Technology, Goterborg, Sweden, 2005.
- [25] Andersson, N., Eriksson, L. E., Davidson, L., "LES Prediction of Flow and Acoustic Filed of a Coaxial Jet," 11th *AIAA/CEAS Aeroacoustics Conference*, Paper No. AIAA 2005-2884, Department of Applied Mechanics, Chalmers University of Technology, Goterborg, Sweden, 2005.
- [26] Morris, P. J., Long, L. N., Scheidegger, T. E., Boluriaan, S., "Simulation of Supersonic Jet Noise", *International Journal of Aeroacoustics*, Vol. 1(1), 2002, pp. 17-41.
- [27] Suto, H., Matsubara, K., Kobayashi, M., Kaneko, Y., "Large Eddy Simulation of Flow and Scalar Transport in a Round Jet," *Heat Transfer-Asian Research*, Vol. 33(3), 2004, pp.175-188.

- [28] DeBonis, J., "A Large Eddy Simulation of a High Reynolds Number Mach 0.9 Jet," 10th AIAA/CEAS Aeroacoustics Conference, , Paper No. AIAA 2004-3025, NASA Glenn Research Center, Cleveland, Ohio, USA, 2004.
- [29] Boersma, B. J., "Large Eddy Simulation of the Sound Field of a Round Turbulent Jet," *Journal of Theoretical Computational Fluid Dynamics*, Vol. 19, 2005, pp. 161-170.
- [30] Cutler, A. D., Diskin, G. S., Drummond, J. P., White, J. A., "Supersonic Coaxial Jet Experiment for Computational Fluid Dynamics Code Validation," *AIAA Journal*, Vol. 44(3), 2006, pp. 585-592.
- [31] Bogey, C., Bailly, C., "Large Eddy Simulation of Round Free Jets Using Explicit Filtering With/Without Dynamic Smagorinsky Model," *International Journal of Numerical Methods for Heat & Fluid Flow*, Vol. 27(2), 2006, pp. 603-610.
- [32] Babu, P. C., Mahesh, K., "Upstream Entrainment in Numerical Simulations of Spatially Evolving Round Jets," *Physics of Fluids*, Vol. 16(10), 2004, pp. 3699-3705.
- [33] Babu, P. C., Mahesh, K., "Direct Numerical Simulation of Passive Scaler Mixing in Spatially Evolving Turbulent Round Jets," 43th AIAA Aeroacoustics Sciences Meeting, , Paper No. AIAA 2005-1121, School of Aerospace Engineering and Mechanics, University of Minnesota, Minnesota, USA, Jan. 2005.
- [34] Bogey, C., Bailly, C., Juvé, D., "Noise Investigation of a High Subsonic, Moderate Reynolds Number Jet Using a Compressible Large Eddy Simulation," *Journal of Theoretical Computing Fluid Dynamics*, Vol. 16, 2003, pp. 273-297.
- [35] Bogey, C., Bailly, C., "LES of a High Reynolds, High Subsonic Jet: Effects of the Inflow Conditions on Flow and Noise", 9th AIAA/CEAS Conference, paper No. 2003-3170, Ecole Centrale de Lyon, Ecully, France, 2003.
- [36] Lew, P. T., Blaisdell, G. A., Lyrantzis, A. S., "Investigation of Noise Sources in Turbulent Hot Jets using Large Eddy Simulation Data," 45th AIAA Aerospace Sciences Meeting and Exhibit, School of Aeroacoustics and Astronautics, Purdue University, West Lafayette, IN., USA, 2007.

- [37] Bogey, C., Bailly, C., "Computation of a High Reynolds Number Jet and Its Radiated Noise Using Large Eddy Simulation Based on Explicit Filtering," *Theoretical Computers & Fluids*, Vol. 35, 2006, pp. 1344, 1358.
- [38] Park, N., Mahesh, K. "Numerical and Modeling Issues in LES of Compressible Turbulence on Unstructured Grids," *45th AIAA Aerospace Science Meeting and Exhibit*, School of Aerodynamics and Astronautics, University of Minnesota, Minneapolis, MN., USA, 2007.
- [39] Park, N., Mahesh, K., "Analysis of Numerical Errors in Large Eddy Simulation Using Statistical Closure Theory," *Journal of Computational Physics*, Vol. 222, 2007, pp. 194-216.
- [40] Ghosal, S., Moin, P., "The Basic Equations for the Large Eddy Simulation of Turbulent Flows in Complex Geometry," *J. of Computational physics*, Vol. 118, 1995, pp. 24-37.
- [41] Constantinescu, G. S., Lele, S. K., "A Highly Accurate Technique for the Treatment of Flow Equations at the Polar Axis in Cylindrical Coordinates Using Series Expansions," *J. of Computational physics*, Vol. 183, 2002, pp. 165-186.
- [42] Fureby, C., Grinstein, F. F., "Large Eddy Simulation of High-Reynolds-Number Free and Wall-Bounded Flows," *Journal of Computational Physics*, Vol. 181, 2002, pp. 68-97.
- [43] Shur, M. L., Spalart, P. R., Strelets, M. Kh., "Noise Prediction for Increasingly Complex Jets. Part I: Methods and Tests," *International Journal of Aeroacoustics*, Vol. 4(3&4), 2005, pp. 213-247.
- [44] Shur, M. L., Spalart, P. R., Strelets, M. Kh., "Noise Prediction for Increasingly Complex Jets. Part II: Applications", *International Journal of Aeroacoustics*, Vol. 4(3&4), 2005, pp. 247-266.
- [45] Shur, M. L., Spalart, P. R., Strelets, M. Kh., Travin, A. K., "Towards the Prediction of Noise from Jet Engines," *International Journal of Numerical Methods for Heat & Fluid Flow*, Vol. 24, 2003, pp. 551-561.

- [46] Wagner, C., Huttli, T., Sagaut, P., *Large Eddy Simulation for Acoustics*, Cambridge University Press, New York, NY, USA, 2007.
- [47] Bodony, D. J., Lele, S. K., "Current Status of Jet Noise Predictions Using Large Eddy Simulation," *AIAA Journal*, Vol. 46(2), 2008, pp. 364-380.
- [48] Sagaut, P., *Large Eddy Simulation for Incompressible Flows*, Springer, New York, 2001.
- [49] Anderson, J. S., Anderson, M. B., *Noise, its Measurement, Analysis, Rating and Control*, Cambridge University Press, Great Britain, 1993.
- [50] Lau, J. C., Morris, P. J., Fisher, J., "Measurements in Subsonic and Supersonic Free Jets Using a Laser velocimeter," *J. Fluid Mechanics*, Vol. 93, 1979, pp. 1-27.
- [51] Lighthill, M. J., "Jet Noise," *AIAA Journal*, Vol. 1(7), 1963, pp. 1507-1517.
- [52] Grinstein, F. F., Margolin, L. G., Rider, W. J., *Implicit Large Eddy Simulation, Computing Turbulent Fluid Dynamics*, Cambridge University Press, New York, USA, 2007.
- [53] Adamson, T. C., Nicholls, J. A., On the Structure of Jets from Highly Underexpanded Nozzles into Still Air, Engineering Research Institute, University of Michigan Ann Arbor, UMR0017,1958.
- [54] Ishii, R., Fujimoto, H., Hatta, N., Umeda, Y., "Experimental and Numerical Analysis of Circular Pulse Jets," *J. Fluid Mechanics*, Vol. 392, 1999, pp. 129-153.
- [55] Pedro, G., Peneau, F., Oshikai, P., Djilali, N., "Computational Analysis of Transient Gas release from a High Pressure Vessel," *Conference CFD2006*, Kingston, Canada, 2006.
- [56] Kameshki, M. R., "Simulation of Hydrogen Jet exiting a High Pressure Reservoir," M.Sc. thesis, Concordia University, Montreal, Quebec, Canada, 2007.

- [57] Ferziger, J. H., "Direct and Large Eddy Simulation of Turbulence," CRM Proceedings and Lecture Notes, Centre de Recherches Mathématiques, Université de Montréal, Montréal, Québec, Canada, Vol. 16, 1998.
- [58] Wasistho, B., "Spatial Direct Numerical Simulation of Compressible Boundary Layer," Ph.D. thesis, Twente University, Indonesia, 1966.
- [59] Maeder, T., Adams, N. A., "Direct Simulation of Turbulent Supersonic Boundary Layers by an Extended Temporal Approach," *J. fluid mechanics*, Vol. 429, 2001, pp. 187-216.
- [60] Grinstein, F. F., Fureby, C., "Recent Progress on MILES for High Reynolds Number Flows," *ASME*, Vol. 124, 2002, pp. 848-861.
- [61] Camarri, S., Salvetti, M.V., Koobus, B., Dervieux, A., "Large-Eddy Simulation of a Bluff-Body Flow on Unstructured Grids," *International Journal for Numerical Methods in Fluids*, Vol. 40, 2002, pp. 1431-1460.
- [62] Spyropoulos, E. T., Blaisdell, G. A., "Evaluation of the Dynamic Subgrid-Scale Model for Large Eddy Simulations of Compressible Turbulent Flows," *33rd Aerospace Sciences meeting and Exhibit*, Purdue University, West Lafayette, Indiana, USA, 1995.
- [63] Quémeré, P., Sagaut, P., "Zonal Multi-Domain RANS/LES Simulations of Turbulent Flows," *International Journal for Numerical Methods in Fluids*, Vol. 40, 2002, pp. 903-925.
- [64] Erlebacher, G., Hussaini, M. Y., Speziale, C. G., Zang, T. A., "Toward the Large-Eddy Simulation of Compressible Turbulent Flows," *J. Fluid Mech.*, Vol. 238, 1992, pp. 155-185.
- [65] Larcheveque, L., Sagaut, P., Mary, I., Labbé, O., "Large-Eddy Simulation of a Compressible Flow Past a Deep Cavity," *Physics of Fluids*, Vol. 15, 2003, pp. 193-210.
- [66] Wang, M., Moin, P., "Dynamic Wall Modeling for Large-Eddy Simulation of Complex Turbulent Flows," *Physics of Fluids*, Vol. 14(7), 2002, pp. 2043-2051.

- [67] Ducros, F., Comte, P., Lesieur, M., "Large-Eddy Simulation of Transition to Turbulence in a Boundary Layer Developing Spatially over a Flat Plate," *J. fluid Mechanics*, Vol. 326, 1996, pp. 1-36.
- [68] Dahlström, S., Davidson, L., "Large Eddy Simulation of flow Around an Airfoil," *39th AIAA Aerospace Sciences Meeting and Exhibit*, Chalmers University of Technology, Sweden, 2001.
- [69] Spyropoulos, E. T., Blaisdell, G. A., "Large-Eddy Simulation of a Spatially Evolving Supersonic Turbulent Boundary Layer Flow," *AIAA Journal*, Vol. 36(11), 1998, pp. 1983-1990.
- [70] Yan, H., Knight, D., Zheltovodov, A. A., "Large-Eddy Simulation of Supersonic Flat-Plate Boundary Layers Using the Monotonically Integrated Large-Eddy Simulation (MILES) Technique," *ASME*, Vol 124, 2002, pp. 868-875.
- [71] Teramoto, S., "Large-Eddy Simulation of Transitional Boundary Layer with Impinging Shock Wave", *AIAA journal*, Vol. 43, 2005, pp. 2354-2363
- [72] Yan, H., Urbin, G., Knight, D., "Compressible Large Eddy Simulation Using Unstructured Grid: Supersonic Boundary Layer and Compression Ramps," *10th International conference on methods of aerophysical research*, Rutgers University, Piscataway, New Jersey, USA, 2000,.
- [73] Garnier, E., Sagaut, P., "Large Eddy Simulation of Shock/Boundary-Layer Interaction," *AIAA journal*, Vol. 40(10), 2002, pp. 1935-1944.
- [74] Stolz, S., Adams, N. A., Kleiser, L., "The Approximation Deconvolution Model for Large-Eddy Simulations of Compressible Flows and Its Application to Shock-Turbulent-Boundary Layer Interaction," *Physics of Fluids*, Vol. 13(10), 2001, pp. 2985-3001.
- [75] Pope, S. B., "Ten Questions Concerning the Large-Eddy Simulation of Turbulent Flows," *New J. of Physics*, Vol. 6, 2004, pp. 1-24.
- [76] Scheidegger, T., "Overview: LES in Fluent 6.2," CFD summit presentation, June 8, 2005.

- [77] Jiménez, J., Wray, A. A., Saffman, P. G., Rogallo, R. S. "The Structure of Intense Vorticity in Isotropic Turbulence," *J. Fluid Mechanics*, Vol. 225, 1993, pp. 65-90.
- [78] Uddin, A., Kato, C., Yamade, Y., Ohishima, N., Tanahashi, M., Miyauchi, T., "Large Eddy Simulation of Homogeneous Isotropic Turbulent Flow Using the Finite Element Method," *JSME*, Vol. 49(1), 2006, pp. 102-114.
- [79] Garnier, E., Mossi, M., Sagaut, P., Comte, P., Deville, M., "On the Use of Shock-Capturing Schemes for Large Eddy Simulation," *Journal of Computational Physics*, Vol. 153, 1999, pp. 273-311.
- [80] Passot, T., Pouquet, A., "Numerical Simulation of Compressible Homogeneous Flows in the Turbulent Regime," *J. Fluid Mechanics*, Vol.181, 1987, pp. 441-466.
- [81] Layton, W. J., "A Mathematical Introduction to Large Eddy Simulation", *H. Deconinck (Ed.), Computational Fluid Dynamics-Multiscale Methods*, 2002.
- [82] Celik, I.B., Cehreli, Z.N., Yavuz, I., "Index of Resolution Quality for Large Eddy Simulations", *Journal of Fluids Engineering(ASME)*, Vol. 127, 2005, pp. 949-958.
- [83] Klein, M., "An Attempt to Assess the Quality of Large Eddy Simulation in the Context of Implicit Filtering", *Flow, Turbulence and Combustion*, Vol. 75, 2005, pp. 131-147.
- [84] Cadiou, A., "NadiaLES: Theoretical Manual," Centre National De La Recherche Scientifique (CNRS), Rept. LMFA-UMR CNRS 5509, France, 2003.
- [85] Hirsch, C., *Numerical Computation on Internal and External Flows*, John Wiley & Sons, New York, 1988, Vol. 1&2.
- [86] Moin, P., Squires, K., Cabot, W., Lee, S., "A Dynamic Subgrid-Scale Model for Compressible Turbulence and Scalar Transport," *Physics of Fluids*, Vol. 3(11), 1991, pp. 2746-2757.
- [87] Mary, I., Sagaut, P., "Large Eddy Simulation of Flow Around an Airfoil Near Stall," *AIAA Journal*, Vol. 40(6), 2002, pp. 1139-1145.

- [88] Hahn, M., Drikakis, D., "Large Eddy Simulation of Compressible Turbulence Using High-Resolution Methods," *International Journal for Numerical Methods in Fluids*, Vol. 47, 2005, pp. 971-977.
- [89] Carpentier, R., "Comparaison Entre des Schémas 2D de Type Roe Sur Maillages Régulier Triangle ou Quadrangle, II: Calcul au Sommet-le $\beta\gamma$ Schéma," Institut National de Recherche en Informatique et en Automatique (INRIA), Rept. 3360, France, Feb. 1980.
- [90] Bui, T. T., "A Parallel, Finite-Volume Algorithm for Large Eddy Simulation of Turbulent Flows," Dryden Flight Research Center, California, NASA/TM-1999-206570, Jan. 1999.
- [91] Dahlström, S., Davidson, L., "Large Eddy Simulation Applied to a High Reynolds Flow Around an Airfoil Close to Stall," *41st AIAA Aerospace Sciences Meeting and Exhibit*, Paper No. AIAA-2003-0776, Chalmers University of Technology, Sweden, 2003.
- [92] Hallo, L., Ribault, C. L., Buffet, M., "An Implicit Mixed Finite-Element-Finite-Volume Method for Solving 3-D Turbulent Compressible Flows," *International Journal for Numerical Method in Fluids*, Vol. 25, 1997, pp. 1241-1261.
- [93] Snir, M., Otto, S., Lederman, S. H., Walker, D., Dongarra, J., *MPI-The Complete Reference*, The MIT Press, Vol. 1, 2nd edition, Massachusetts Institute of Technology, Cambridge, London, England, 1998.
- [94] John, V., *Large Eddy Simulation of Turbulent Incompressible Flows*, Springer-Verlag Berlin Heidelberg, Germany, 2004.
- [95] Knight, D., Zhou, G., Okong'o, N., Shukla, V., "Compressible Large Eddy Simulation Using Unstructured Grids," *36th Aerospace Sciences Meeting and Exhibit*, Paper No. AIAA-1998-0535, Rutgers Univ., Piscataway, NJ, USA, 1998.
- [96] Hickel, S., Adams, N. A., Domaradzki, J. A., "An Adaptive Local Deconvolution Method for Implicit LES," *J. of Computational physics*, Vol. 213, 2006, pp. 413-436.

- [97] Comte-Bellot, G., Corrsin, S., "Simple Eulerian Time Correlations of Full and Narrow Band Velocity Signals in Grid Generated Isotropic Turbulence," *J. Fluid Mech.*, Vol. 48(2), 1971, pp. 273-337.
- [98] McMillan, O. J., Ferziger, J. H., "Direct Testing of Subgrid-Scale Models," *AIAA Journal*, Vol. 17(12), 1979, pp. 1340-1346.
- [99] Panda, J., Seasholtz, R. G., "Experimental Investigation of Density fluctuations in High-Speed Jets and Correlation with Generated Noise", *J. Fluid Mechanics*, vol. 450, 2002, pp. 97-130.
- [100] Panda, J., Seasholtz, R. G., "Velocity and Temperature Measurement in Supersonic Free Jets Using Spectrally Resolved Rayleigh Scattering," Modern Technologies Corporation, Middleburg, Ohio, NASA/TM-2003-212391, 2003.
- [101] Panda, J., Seasholtz, R. G., Elam, K., "Measurement of Correlation Between Flow Density, Velocity, and Density*Velocity² With Far Field Noise in High Speed Jets," Ohio Aerospace Institute and Glenn Research Center, NASA/TM-2002-211791, Sept. 2002.
- [102] Panda, J., Zaman, K. B. M. Q., Seasholtz, R. G., "Measurement of Initial Conditions at Nozzle Exit of High Speed Jets," Ohio Aerospace Institute and Glenn Research Center, NASA/TM-2004-212392, May 2004.
- [103] Seasholtz, R. G., Panda, J., "Multiple Point Dynamic Gas Density Measurements Using Molecular Rayleigh Scattering," Ohio Aerospace Institute and Glenn Research Center, NASA/TM-1999-209295, 1999.
- [104] Bogey, C., Bailly, C., "Investigation of Downstream and Sideline Subsonic Jet Noise Using Large Eddy Simulation," *Theoretical Computational Fluid Dynamics*, Vol. 20(1), 2006, pp. 23, 40.
- [105] Bodony, D. J., Lele, S. K., "Jet Noise Prediction of Cold and Hot Subsonic Jets Using Large-Eddy Simulation," *10th AIAA/CEAS Aeroacoustics Conference*, Paper No. AIAA-2004-3022, Manchester, GREAT BRITAIN, May 10-12, 2004.

- [106] Tajallipour, N., Owlam, B. B., Paraschivoiu, M., "A Self-Adaptive Upwinding Method for Large Eddy Simulation of Turbulent Flows on Unstructured Elements," *Submitted to the American institute of Aeronautics and astronautics (AIAA)*, June 2008.
- [107] Schetz, J. A., *Boundary Layer Analysis*, Prentice Hall, Englewood, New Jersey Cliffs, USA, 1993.
- [108] Munson, B. R., Young, D. F., Okiishi, T. H., *Fundamentals of Fluid Mechanics*, Fourth Edition, John Wiley & Sons Inc., USA, 2002.
- [109] Schlichting, H., "Laminar Struhlausbreitung" [Laminar Jet Spreading], *Z. Angew Math. Mech.*, Vol. 13, 1933, pp.260-263.
- [110] White, F. M., *Viscous Fluid Flow*, McGraw Hill, 2nd edition, New York, 1992.

A.1 Theoretical Analysis of Free Jets

From the theoretical point of view, the laminar, incompressible round jets that are flowing into an open medium which is in rest is the simplest case to be analyzed. These flows are usually studied using the similarity solutions which will be presented bellow. Further details can be found in Ref. 107.

The Newton's second law of motion for a system can be written as follows (Ref. 108):

$$\frac{D}{Dt}_{sys} \int \rho \vec{v} dv = \Sigma F_{sys} \quad (A.1)$$

in which

$$\frac{D}{Dt}_{sys} \int \rho \vec{v} dv = \frac{\partial}{\partial t}_{cv} \int \rho \vec{v} dv + \int_{cs} \rho \vec{v} (\vec{v} \cdot \vec{n}) ds \quad (A.2)$$

and

$$\Sigma F_{sys} = \Sigma F_{Corresponding\ Control\ Volume} \quad (A.3)$$

Assuming that the system has no motion and the flow conditions are not changing at the exit of the jet, we

can assume that $\frac{\partial}{\partial t}_{cv} \int \rho \vec{v} dv = 0$ and therefore

$$\frac{D}{Dt}_{sys} \int \rho \vec{v} dv = \int_{cs} \rho \vec{v} (\vec{v} \cdot \vec{n}) ds = J \quad (A.4)$$

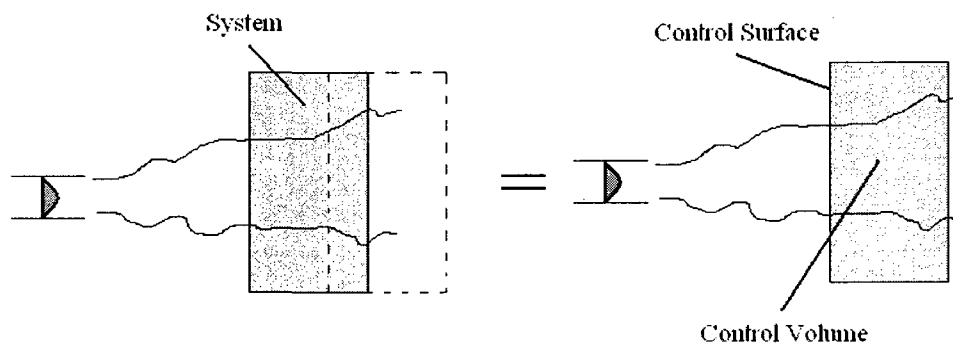


Fig. A.1 Definition of a typical system, control volume and its control surface within a free jet.

Flow is supposed to be 2D, steady and incompressible. Pressure gradients are neglected in the domain therefore the momentum equation along the jet (x-axis) will be:

$$U_r \frac{\partial U_x}{\partial r} + U_x \frac{\partial U_x}{\partial x} = \nu \left(\frac{1}{r} \frac{\partial}{\partial r} \left(r \frac{\partial U_x}{\partial r} \right) \right) \quad (\text{A.5})$$

Potential function can be defined as:

$$U_x = \frac{1}{r} \frac{\partial \Psi}{\partial r} \quad U_r = -\frac{1}{r} \frac{\partial \Psi}{\partial x} \quad (\text{A.6})$$

By substituting the above definitions into Eq. (A.5), we will have:

$$-\frac{1}{r^2} \frac{\partial \Psi}{\partial x} \frac{\partial^2 \Psi}{\partial r^2} + \frac{1}{r^3} \frac{\partial \Psi}{\partial x} \frac{\partial \Psi}{\partial r} + \frac{1}{r^2} \frac{\partial \Psi}{\partial r} \frac{\partial^2 \Psi}{\partial r \partial x} = \nu \left(-\frac{1}{r^2} \frac{\partial^2 \Psi}{\partial r^2} + \frac{1}{r^3} \frac{\partial \Psi}{\partial r} + \frac{1}{r} \frac{\partial^3 \Psi}{\partial r^3} \right) \quad (\text{A.7})$$

It is assumed that $\Psi = \nu x^A f(\eta = \frac{r}{x^B})$, then all the required derivatives of Ψ are calculated:

$$\frac{\partial \eta}{\partial x} = \frac{-B\eta}{x} \quad (\text{A.8})$$

$$\frac{\partial \Psi}{\partial x} = \nu \left(Ax^{A-1} f(\eta) - B\eta x^{A-1} f'(\eta) \right) \quad (\text{A.9})$$

$$\frac{\partial \Psi}{\partial r} = \nu x^{A-B} f'(\eta) \quad (\text{A.10})$$

$$\frac{\partial^2 \Psi}{\partial r^2} = \nu x^{A-2B} f''(\eta) \quad (\text{A.11})$$

$$\frac{\partial^3 \Psi}{\partial r^3} = \nu x^{A-3B} f'''(\eta) \quad (\text{A.12})$$

$$\begin{aligned} \frac{\partial^2 \Psi}{\partial r \partial x} &= \nu(A-B)x^{A-B-1} f'(\eta) + \nu x^{A-B} f''(\eta) \frac{-B\eta}{x} \\ \frac{\partial^2 \Psi}{\partial r \partial x} &= \nu(A-B)x^{A-B-1} f'(\eta) - \nu B\eta x^{A-B-1} f''(\eta) \end{aligned} \quad (\text{A.13})$$

Now all the computed terms are substituted in Eq. (A.7):

$$\begin{aligned}
-\frac{1}{r^2} \frac{\partial \Psi}{\partial x} \frac{\partial^2 \Psi}{\partial r^2} &= -\frac{v}{r^2} (Ax^{A-1} f(\eta) - B\eta x^{A-1} f'(\eta)) (vx^{A-2B} f''(\eta)) = -\frac{v^2}{r^2} (Ax^{2(A-B)-1} f(\eta) f''(\eta) - B\eta x^{2(A-B)-1} f'(\eta) f''(\eta)) \\
\frac{1}{r^3} \frac{\partial \Psi}{\partial x} \frac{\partial \Psi}{\partial r} &= \frac{v}{r^3} (Ax^{A-1} f(\eta) - B\eta x^{A-1} f'(\eta)) (vx^{A-B} f'(\eta)) = \frac{v^2}{r^3} (Ax^{2A-B-1} f(\eta) f'(\eta) - B\eta x^{2A-B-1} f'(\eta)^2) \\
\frac{1}{r^2} \frac{\partial \Psi}{\partial r} \frac{\partial^2 \Psi}{\partial r \partial x} &= \frac{1}{r^2} (vx^{A-B} f'(\eta)) (v(A-B)x^{A-B-1} f'(\eta) - vB\eta x^{A-B-1} f''(\eta)) = \frac{v^2}{r^2} ((A-B)x^{2(A-B)-1} f'(\eta)^2 - B\eta x^{2(A-B)-1} f'(\eta) f''(\eta))
\end{aligned}$$

$$v \left(-\frac{1}{r^2} \frac{\partial^2 \Psi}{\partial r^2} + \frac{1}{r^3} \frac{\partial \Psi}{\partial r} + \frac{1}{r} \frac{\partial^3 \Psi}{\partial r^3} \right) = -\frac{v^2}{r^2} x^{A-2B} f''(\eta) + \frac{v^2}{r^3} x^{A-B} f'(\eta) + \frac{v^2}{r} x^{A-3B} f'''(\eta) \quad (\text{A.14})$$

$$\begin{aligned}
&-\frac{1}{r^2} \frac{\partial \Psi}{\partial x} \frac{\partial^2 \Psi}{\partial r^2} + \frac{1}{r^3} \frac{\partial \Psi}{\partial x} \frac{\partial \Psi}{\partial r} + \frac{1}{r^2} \frac{\partial \Psi}{\partial r} \frac{\partial^2 \Psi}{\partial r \partial x} - v \left(-\frac{1}{r^2} \frac{\partial^2 \Psi}{\partial r^2} + \frac{1}{r^3} \frac{\partial \Psi}{\partial r} + \frac{1}{r} \frac{\partial^3 \Psi}{\partial r^3} \right) = \\
&\left(-\frac{v^2}{r^2} (Ax^{2(A-B)-1} f(\eta) f''(\eta) - B\eta x^{2(A-B)-1} f'(\eta) f''(\eta)) \right) + \left(\frac{v^2}{r^3} (Ax^{2A-B-1} f(\eta) f'(\eta) - B\eta x^{2A-B-1} f'(\eta)^2) \right) + \\
&\left(\frac{v^2}{r^2} ((A-B)x^{2(A-B)-1} f'(\eta)^2 - B\eta x^{2(A-B)-1} f'(\eta) f''(\eta)) \right) - \left(-\frac{v^2}{r^2} x^{A-2B} f''(\eta) + \frac{v^2}{r^3} x^{A-B} f'(\eta) + \frac{v^2}{r} x^{A-3B} f'''(\eta) \right) = 0
\end{aligned}$$

$$\begin{aligned}
&-\frac{1}{r^2} \frac{\partial \Psi}{\partial x} \frac{\partial^2 \Psi}{\partial r^2} + \frac{1}{r^3} \frac{\partial \Psi}{\partial x} \frac{\partial \Psi}{\partial r} + \frac{1}{r^2} \frac{\partial \Psi}{\partial r} \frac{\partial^2 \Psi}{\partial r \partial x} - v \left(-\frac{1}{r^2} \frac{\partial^2 \Psi}{\partial r^2} + \frac{1}{r^3} \frac{\partial \Psi}{\partial r} + \frac{1}{r} \frac{\partial^3 \Psi}{\partial r^3} \right) = \\
&f(\eta) f''(\eta) \left(-\frac{v^2}{r^2} Ax^{2(A-B)-1} \right) + f'(\eta) f''(\eta) \left(\frac{v^2}{r^2} B\eta x^{2(A-B)-1} - \frac{v^2}{r^2} B\eta x^{2(A-B)-1} \right) \\
&+ f(\eta) f'(\eta) \left(\frac{v^2}{r^3} Ax^{2A-B-1} \right) + f'(\eta)^2 \left(-\frac{v^2}{r^3} B\eta x^{2A-B-1} + \frac{v^2}{r^2} (A-B)x^{2(A-B)-1} \right) \\
&- \left(-\frac{v^2}{r^2} x^{A-2B} f''(\eta) + \frac{v^2}{r^3} x^{A-B} f'(\eta) + \frac{v^2}{r} x^{A-3B} f'''(\eta) \right) = 0
\end{aligned}$$

And finally the momentum equation is simplified into the following form:

$$\begin{aligned}
&f(\eta) f''(\eta) \left(-\frac{1}{r^2} Ax^{2(A-B)-1} \right) + f(\eta) f'(\eta) \left(\frac{1}{r^3} Ax^{2A-B-1} \right) \\
&+ f'(\eta)^2 \left(-\frac{1}{r^3} B\eta x^{2A-B-1} + \frac{1}{r^2} (A-B)x^{2(A-B)-1} \right) \\
&- \left(-\frac{1}{r^2} x^{A-2B} f''(\eta) + \frac{1}{r^3} x^{A-B} f'(\eta) + \frac{1}{r} x^{A-3B} f'''(\eta) \right) = 0
\end{aligned} \quad (\text{A.15})$$

On the other hand, the potential function can also be substituted into Eq. (A.4) which will result:

$$\begin{aligned} \frac{D}{Dt}_{\text{sys}} \int \rho \bar{V} dv &= \int_{cs} \rho \bar{V} (\bar{V} \cdot \bar{n}) ds = \int_{cs} \rho U_x^2 ds = \int_0^{+\infty} \rho \left(\frac{v x^{A-B}}{r} f'(\eta) \right)^2 2\pi r dr = \int_0^{+\infty} \rho (v x^{A-B} f'(\eta))^2 \frac{d\eta}{\eta} \\ \int_{cs} \rho \bar{V} (\bar{V} \cdot \bar{n}) ds &= 2\pi \rho v^2 \int_0^{+\infty} x^{2A-2B} f'(\eta)^2 \frac{d\eta}{\eta} = J \end{aligned} \quad (\text{A.16})$$

J has to remain bounded and constant for different values of x , therefore B has to be equal to A.

$$\begin{aligned} f(\eta) f''(\eta) \left(-\frac{1}{r^2} A x^{-1} \right) + f(\eta) f'(\eta) \left(\frac{1}{r^3} A x^{A-1} \right) + f'(\eta)^2 \left(-\frac{1}{r^3} A \eta x^{A-1} \right) \\ - \left(-\frac{1}{r^2} x^{-A} f''(\eta) + \frac{1}{r^3} f'(\eta) + \frac{1}{r} x^{-2A} f'''(\eta) \right) = 0 \end{aligned} \quad (\text{A.17})$$

Assuming that all the terms in Eq. (A.17) have the same dimension, A has to be equal to 1:

$$\begin{aligned} f(\eta) f''(\eta) \left(-\frac{1}{r^2} x^{-1} \right) + f(\eta) f'(\eta) \left(\frac{1}{r^3} \right) + f'(\eta)^2 \left(-\frac{1}{r^3} \eta \right) \\ - \left(-\frac{1}{r^2} x^{-1} f''(\eta) + \frac{1}{r^3} f'(\eta) + \frac{1}{r} x^{-2} f'''(\eta) \right) = 0 \end{aligned} \quad (\text{A.18})$$

By multiplying r^3 into the Eq. (A.18), the following equation is obtained:

$$\begin{aligned} -\eta f(\eta) f''(\eta) + f(\eta) f'(\eta) - \eta f'(\eta)^2 - \left(-\eta f''(\eta) + f'(\eta) + \eta^2 f'''(\eta) \right) = 0 \\ \frac{1}{\eta^2} \left(-\eta f(\eta) f''(\eta) + f(\eta) f'(\eta) - \eta f'(\eta)^2 \right) = \frac{d \left(-\frac{f'(\eta)}{\eta} + f''(\eta) \right)}{d\eta} \end{aligned} \quad (\text{A.19})$$

with the following boundary conditions:

$$\begin{aligned} U_x &= \frac{1}{r} \frac{\partial \Psi}{\partial r} = \frac{v}{r} f'(\eta) \\ U_r &= -\frac{1}{r} \frac{\partial \Psi}{\partial x} = -\frac{v}{r} (f(\eta) - \eta f'(\eta)) \end{aligned} \quad (\text{A.20})$$

$$\begin{aligned} \lim_{r \rightarrow \infty} U_x &= \lim_{\eta \rightarrow \infty} f'(\eta) = 0 \\ \lim_{r \rightarrow 0} U_r &= \lim_{\eta \rightarrow 0} f(\eta) = f(0) = 0 \\ \lim_{r \rightarrow 0} \frac{\partial U_x}{\partial r} &= \lim_{\eta \rightarrow 0} \left(\frac{v \eta f''(\eta) - f'(\eta)}{r^2} \right) = \lim_{\eta \rightarrow 0} f'(\eta) = 0 \end{aligned} \quad (\text{A.21})$$

Schlichting (1933),¹⁰⁹ has proposed the following closed form solution which has also mentioned in Ref. 110):

$$f(\eta) = \frac{\eta^2}{16\pi\rho v^2 / 3J + \eta^2 / 4} \quad (\text{A.22})$$

$$U = \frac{3J}{8\pi\rho v x} \left(1 + \frac{3J\eta^2}{64\pi\rho v^2} \right)^{-2} \quad (\text{A.23})$$

$$U_{\max} = \frac{3J}{8\pi\rho v x} \quad (\text{A.24})$$

$$\frac{U}{U_{\max}} = \left(1 + \frac{3J\eta^2}{64\pi\rho v^2} \right)^{-2} \quad (\text{A.25})$$

Equation (A.23) has been used in Ref. 32 to validate their numerical results.

If we assume that one side of the control volume goes vertically through the nozzles and also if we neglect the flow coming from behind the nozzle then an approximation for the parameter J is calculated as follows:

$$J = \int_{cs} \rho \bar{V} (\bar{V} \cdot \bar{n}) ds = \frac{\pi D^2 \rho_j U_j^2}{4} \quad (\text{A.26})$$